

AFRL-IF-RS-TR-2002-158
Final Technical Report
July 2002



ANALYSIS AND CHARACTERIZATION OF AN ACOUSTO-OPTIC BEAM POSITION CONTROL SYSTEM

SUNY at Binghamton

APPROVED FOR PUBLIC RELEASE; DISTRIBUTION UNLIMITED.

**AIR FORCE RESEARCH LABORATORY
INFORMATION DIRECTORATE
ROME RESEARCH SITE
ROME, NEW YORK**


This report has been reviewed by the Air Force Research Laboratory, Information Directorate, Public Affairs Office (IFOIPA) and is releasable to the National Technical Information Service (NTIS). At NTIS it will be releasable to the general public, including foreign nations.

AFRL-IF-RS-TR-2002-158 has been reviewed and is approved for publication.

A handwritten signature in black ink, appearing to read "D J Nicholson".

APPROVED:

DONALD J. NICHOLSON
Project Engineer

A handwritten signature in black ink, appearing to read "Warren H. Debany".

FOR THE DIRECTOR:

WARREN H. DEBANY, Technical Advisor
Information Grid Division
Information Directorate

REPORT DOCUMENTATION PAGE			<i>Form Approved</i> <i>OMB No. 074-0188</i>	
Public reporting burden for this collection of information is estimated to average 1 hour per response, including the time for reviewing instructions, searching existing data sources, gathering and maintaining the data needed, and completing and reviewing this collection of information. Send comments regarding this burden estimate or any other aspect of this collection of information, including suggestions for reducing this burden to Washington Headquarters Services, Directorate for Information Operations and Reports, 1215 Jefferson Davis Highway, Suite 1204, Arlington, VA 22202-4302, and to the Office of Management and Budget, Paperwork Reduction Project (0704-0188), Washington, DC 20503				
1. AGENCY USE ONLY (Leave blank)		2. REPORT DATE JULY 2002	3. REPORT TYPE AND DATES COVERED Final May 00 – May 01	
4. TITLE AND SUBTITLE ANALYSIS AND CHARACTERIZATION OF AN ACOUSTO-OPTIC BEAM POSITION CONTROL SYSTEM			5. FUNDING NUMBERS C - F30602-00-1-0582 PE - 62702F PR - 558B TA - II WU - RS	
6. AUTHOR(S) Victor Skorman				
7. PERFORMING ORGANIZATION NAME(S) AND ADDRESS(ES) SUNY at Binghamton The Research Foundation Office of Sponsored Programs PO Box 6000 Binghamton New York 13902-6000			8. PERFORMING ORGANIZATION REPORT NUMBER N/A	
9. SPONSORING / MONITORING AGENCY NAME(S) AND ADDRESS(ES) Air Force Research Laboratory/IFGC 525 Brooks Road Rome New York 13441-4505			10. SPONSORING / MONITORING AGENCY REPORT NUMBER AFRL-IF-RS-TR-2002-158	
11. SUPPLEMENTARY NOTES AFRL Project Engineer: Donald J. Nicholson/IFGC/(315) 330-7437/ Donald.Nicholson@rl.af.mil				
12a. DISTRIBUTION / AVAILABILITY STATEMENT APPROVED FOR PUBLIC RELEASE; DISTRIBUTION UNLIMITED.				12b. DISTRIBUTION CODE
13. ABSTRACT (Maximum 200 Words) This is the final report for study of laser beam position control using an Acousto-Optic cell. The effort was performed under a Cooperative Research and Development Agreement (CRDA) between the State of New York University in Binghamton and the Air Force Research Laboratory. The study consisted of five parts: Theoretical analysis, experimental analysis of the system components, cell design considerations, comparison with the behavior of a system based on Piezo-Electric technology, and finally the design and performance of a model reference adaptive control system for using the cell in a jitter rejection mode.				
14. SUBJECT TERMS Laser Communication, Acoustic-Optics Control System				15. NUMBER OF PAGES 119
				16. PRICE CODE
17. SECURITY CLASSIFICATION OF REPORT UNCLASSIFIED	18. SECURITY CLASSIFICATION OF THIS PAGE UNCLASSIFIED	19. SECURITY CLASSIFICATION OF ABSTRACT UNCLASSIFIED	20. LIMITATION OF ABSTRACT UL	

Table of Contents

1. THEORETICAL ANALYSIS OF ACOUSTO-OPTIC PHENOMENA AND ITS IMPLEMENTATION IN BRAGG CELLS	1
1.1. Mathematical Description Of The Bragg Cell	1
1.2. Assessment Of The Environmental Effects On The Efficiency And Performance Of The Bragg Cell System.....	11
1.3 Conclusion	14
REFERENCES	16
2. EXPERIMENTAL ANALYSIS AND CHARACTERIZATION OF THE LASER BEAM POSITIONING SYSTEM COMPONENTS.....	17
2.1. Experimental Analysis And Characterization Of The Bragg Cell.....	17
2.2. Experimental Analysis And Characterization Of The Quadrant Detector.....	31
2.2.1. Experimental characterization of the quadrant detector	31
2.2.2. Mathematical description of the quadrant detector.....	36
2.3. Conclusion	42
REFERENCES	43
3. BRAGG CELL DESIGN CONSIDERATIONS	44
3.1. Interaction Medium Choice	45
3.2. Choice Of Field Of Regard, Time Bandwidth And Beam Dimensions.....	47
3.3. Center Frequency Choice And Bragg Cell Design	49
3.4. Design And Materials Alternatives.....	60
3.5. Application Of Genetic Algorithms For Design Optimization Of A Bragg Cell .	65
3.6. Other Research Aspects	71
3.7. Conclusion	74
REFERENCES	75
4. COMPARATIVE ANALYSIS OF ACOUSTO-OPTIC AND PIEZO-ELECTRIC STEERING TECHNOLOGY	76
4.1. Piezo-Electric Steering System Components.....	76
4.2. Piezo-Electric Mirror Model.....	77
4.3. Comparative Analysis.....	83
4.4. Conclusion	85
REFERENCES	86
5. MODEL REFERENCE ADAPTIVE CONTROL.....	87
5.1. Simulation Analysis Of The Existing System	87
5.2. Design Of The Reference Model Controller.....	90
5.3. Testing Of The Model Reference Controller By Computer Simulations	95
5.4. Jitter Rejection	102
5.5. Acoustic Power Control: Diffraction Efficiencies.....	106
5.6. Conclusion	111
REFERENCES	112

Table of Figures

Figure 1.1. Principle of operation of the Bragg cell	3
Figure 1.2. Momentum conservation diagram.....	4
Figure 1.3. Momentum diagram	5
Figure 1.4. Intensity distribution for $Q=2\pi$	8
Figure 1.5. Intensity distribution for $Q = 4\pi$	9
Figure 1.6. Intensity distribution for $Q = 8\pi$	10
Figure 1.7. Dimension of the AO medium and the piezoelectric transducer.....	13
Figure 2.1. Laser Beam Positioning System.....	18
Figure 2.2. Quadrant detector circuit.....	19
Figure 2.3. Deflection angles for the first frequency band	20
Figure 2.4. Deflection angles for the second frequency band.....	20
Figure 2.5. Step response of the Bragg cell	21
Figure 2.6. Delay estimation experiment.....	22
Figure 2.7. Electronics delay experiment	23
Figure 2.8. Electronics delay (zoom-in)	24
Figure 2.9. Lines of pixels at $f = 18$ MHz.....	25
Figure 2.10. One frame at $f = 18$ MHz	25
Figure 2.11. Lines of pixels at $f = 21$ MHz.....	26
Figure 2.12. One frame at $f = 21$ MHz	26
Figure 2.13. Lines of pixels at $f = 24$ MHz.....	27
Figure 2.14. One frame at $f = 24$ MHz	27
Figure 2.15. Lines of pixels at $f = 27$ MHz.....	28
Figure 2.16. One frame at $f = 27$ MHz	28
Figure 2.17. Lines of pixels at $f = 30$ MHz.....	29
Figure 2.18. One frame at $f = 30$ MHz	29
Figure 2.19. Acoustic attenuation effect.....	30
Figure 2.20. Silicon Photodiode Quadrant detector RCA C30927E [3].....	31
Figure 2.21 Quadrant detector simplified scheme	32
Figure 2.22. The quadrant detector circuitry [4].....	33
Figure 2.23. Azimuth channel response to horizontal beam displacement ($y=0$).....	34
Figure 2.24 Azimuth channel response to diagonal beam displacement ($y=x$)	34
Figure 2.25 Illustration of coupling effect in the quadrant detector	35
Figure 2.26 Response in the azimuth channel	36
Figure 2.27. Error plot for the rational interpolation method	38
Figure 2.28. Azimuth Channel Response (Numerical Model)	39
Figure 2.29. Elevation Channel Response (Numerical Model)	40
Figure 2.30. Azimuth Channel Response (Analytical Approximation).....	41
Figure 2.31. Analytical Approximation Error.....	41
Figure 3.1. BER versus link range for different beam diameters [1].....	44
Figure 3.2. Thermal and Deflection figures of merit for different acousto-optic materials [1].....	46
Figure 3.3. Field of regard Θ_{FOR} versus the beam size for different spot resolutions N_{tb}	47
Figure 3.4. Vector diagrams for isotropic and birefringent cells.....	50

Figure 3.5. Birefringent momentum diagram	51
Figure 3.6. Off-axis illustration for non-rotated Bragg cell[2]	53
Figure 3.7. First solution method for off axis device with $\lambda = 632.8nm$ and $\bar{\theta}_a = 6^\circ$	54
Figure 3.8. Illustration of the rediffraction at the degenerate frequency f_d for on-axis Bragg cells	55
Figure 3.9. Illustration of the rediffraction at the degenerate frequency f_d for off-axis Bragg cells	56
Figure 3.10. The second solution method applied to the off axis Bragg cell design with $\lambda_o = 632.8nm$ and an 8° off axis angle as per[2].	57
Figure 3.11. Rotated acousto-optic interaction plane	61
Figure 3.12. Region (under the curve) where (3.20) could be used with less than 1 percent approximation error	62
Figure 3.13. Transducer position on a rotated cell.....	64
Figure 3.14 Genetic Optimization of Optimal Design.....	67
Figure 3.15. The wave-vector diagram of the 2D interaction.....	73
Figure 4.1. Step response for Channel 1	79
Figure 4.2. Step response for Channel 2	79
Figure 4.3. Step response for Channel 3	80
Figure 4.4. VISSIM simulation model of the piezo-electric mirror	81
Figure 4.5. Simulated step response for Channel 1	82
Figure 4.6. Simulated step response for Channel 2	82
Figure 4.7. Simulated step response for Channel 3	83
Figure 5.1. Open loop simulation block diagram	87
Figure 5.2. Plant compound block.	88
Figure 5.3. Open-loop simulation results.....	89
Figure 5.4. Closed-loop simulation results without the adaptation mechanism.	93
Figure 5.5. Closed-loop adaptive control system simulation setup	96
Figure 5.6. Simulation results for the azimuth channel of the AMF control closed-loop system	97
Figure 5.7. Tracking error in the azimuth channel.....	98
Figure 5.8. Simulation results for the elevation channel of the AMF control closed-loop system	98
Figure 5.9. Tracking error in the elevation channel.....	99
Figure. 5.10. Azimuth channel response for $\tau = 0$	100
Figure. 5.11. Azimuth channel tracking error for $\tau = 0$	101
Figure. 5.12. Elevation channel response for $\tau = 0$	101
Figure. 5.13. Elevation channel tracking error for $\tau = 0$	102
Figure 5.14 Noise sample after appropriate filtering.....	103
Figure 5.15 Azimuth response to noise signal injected in the horizontal channel.....	104
Figure 5.16. Elevation response to noise signal injected in the horizontal channel	104
Figure 5.17 Azimuth response to noise signal injected in the vertical channel.....	105
Figure 5.18 Elevation response to noise signal injected in the vertical channel.....	106
Figure. 5.19. Acoustic frequency applied to the Bragg cell.....	107
Figure 5.20. Deflection angle change	108
Figure 5.21. Diffraction efficiency for $P_a = 400$ mW	108

Figure 5.22. Diffraction efficiency for $P_a = 292.3 \text{ mW}$	109
Figure 5.23. Diffraction efficiency as a function of acoustic power	110

Table of Tables

Table 3.1. Second solution characteristic parameter definition.....	58
Table 3.2. Value of R versus allowable uniformities.....	59
Table 3.3. Velocity v versus off axis angle θ_a	59
Table 3.4. Velocity values for pairs where the approximation is not to be used.....	62
Table 3.5. Genetic optimization for off- axis acoustically rotated device	70
Table 4.1. Properties of Bragg cells and piezo-electric mirrors	85

1. THEORETICAL ANALYSIS OF ACOUSTO-OPTIC PHENOMENA AND ITS IMPLEMENTATION IN BRAGG CELLS

In optical free-space laser communications, a new steering technique is being developed. It involves the use of acousto-optics (AO), and particularly the use of a combination of two Bragg cells in series to achieve both the horizontal and vertical steering. The reason to use AO arises from the need of a high-speed steering, as opposed to the speed limitations that are encountered using mechanical steering devices. Indeed, Bragg cells offer higher tracking bandwidth, and high optical and electrical efficiency.

A description of the acousto-optic phenomena that occurs inside the Bragg cell is given. Analysis of the factors responsible for inertia, accuracy, power consumption, and mass of the devices is provided. Finally, an assessment of the environmental effects on the efficiency of the Bragg cell is made.

1.1. Mathematical Description Of The Bragg Cell

As stated earlier, Bragg cells are being studied as a part of a laser beam steering system in order to accomplish the agile steering of the laser beam used in satellite communication. The use of a laser beam in satcom offers many advantages such as the small beam divergence, narrow beam width, and high switching ability. These three characteristics result in a communication channel that can offer a virtually continuous and more secure data transfer. However, the use of laser beams as a communication medium is associated with a main technical challenge: high accuracy pointing, acquisition, and tracking (PAT) is required. Indeed, a small angle deviation at the emitting source results in a high position error due to the large distances between communicating stations involved in laser communications. Moreover, other considerations might be noticed in the use of the Bragg cell, as to yield the exact deflection of the laser beam. The main one concerns the angle at which the laser beam reaches the Bragg cell. This angle must be equal to the Bragg angle, and the input frequency must be within a predefined frequency range to ensure that the Bragg cell is still in the Bragg regime.

A-Definition of the Bragg condition:

The Bragg cell is an AO device that can be manufactured either from glass or plastic. This device can be viewed as a medium where light interacts with sound yielding a diffracted light beam. Bragg cells can operate in two regimes, the Bragg regime, and the Raman-Nath regime. The working regime of the Bragg cell is determined by the Klein–Cook parameter $Q = 2\pi \lambda L / \Lambda^2$ where λ is the wavelength of the incident laser beam, L is the width of the acoustic transducer in the cell, Λ is the sound wavelength. This ratio is basically a figure of merit that helps describe the acousto-optic interaction in a given configuration. When this ratio is much greater than 2π , the cell is in the Bragg regime, and if not, it is in the Raman Nath regime. The Raman Nath regime is the regime at when the cell outputs more than two orders of light. When the cell is in the Bragg regime, the diffracted light beam will have a different frequency and new direction, depending on both the sound frequency, and the incident beam direction as shown in Figure 1.1. Parameters shown in the figure are: f_c - center frequency of the acoustic wave, n – the index of refraction, v - acoustic velocity in crystal medium.

The sound wave is generated by the input RF signal that goes through a transducer, the RF signal being the original signal that causes the beam deflection to the desired spot. As the RF signal passes through the transducer, it is transformed in a sound wave that travels through the Bragg cell. Thus, different regions of expansion and compression are created inside the Bragg cell, producing changes in density, which yields a change in the index of refraction of the Bragg cell following the equation [1]:

$$\Delta n(z,t) = \Delta n \sin(w_s t - k_s z), \quad (1.1)$$

Where z - position in the Bragg cell along the vertical axis;

w_s - sound frequency,

k_s - sound wave vector given by w_s/v .

The change in the index of refraction creates a grating inside the Bragg cell, which is responsible for the beam deflection. It happens as a result of collision of light with sound. It can also be viewed, for simplification, as a collision between a light photon and a sound phonon. After the collision has occurred, the result at the output of the Bragg cell is a diffracted photon with a different frequency.

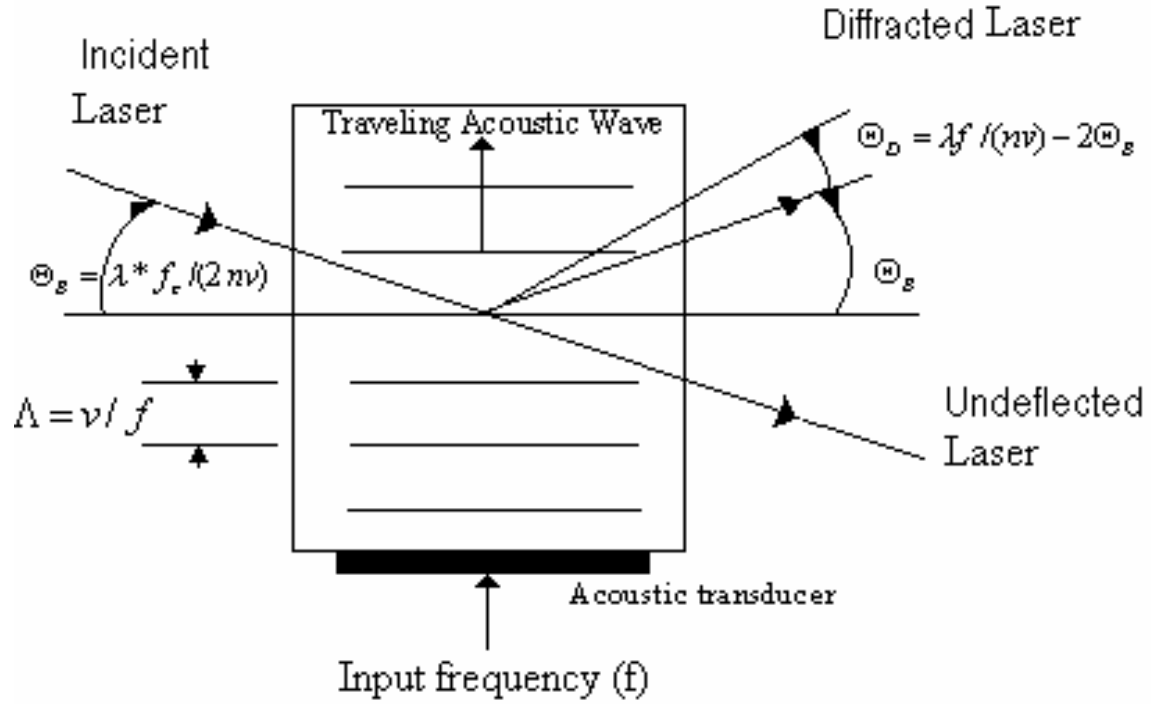


Figure 1.1. Principle of operation of the Bragg cell

Let w_i be the frequency of the incident light, and k_i be the propagation vector of light, then using the conservation of energy principle and the principle of momentum conservation, we can define, the frequency, and propagation vector of the diffracted laser beam to be:

$$w_d = w_s + w_i \quad (1.2)$$

$$k_d = k_s + k_i \quad (1.3)$$

Using the fact that sound frequencies are less than 10^{10} Hz, while the optical frequencies are higher than 10^{13} Hz, w_s can be neglected in (1.2), hence:

$$w_d = w_i \quad (1.4)$$

which implies that

$$k_d = k_i = k. \quad (1.5)$$

Using this relation, in the following scheme, representing the light-sound interaction in the Bragg cell yields what is known as the Bragg condition.

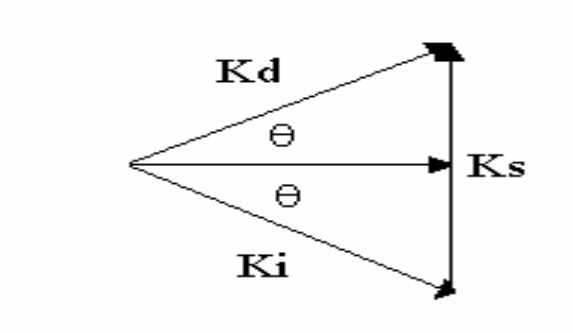


Figure 1.2. Momentum conservation diagram

Indeed, if

$$k_d = k_i = k, \quad (1.6)$$

then

$$k_s = 2k \sin \theta, \quad (1.7)$$

Where θ is the incidence angle of the laser beam.

Using the fact that

$$k = 2\pi / \lambda, \quad (1.8)$$

and

$$k_s = 2\pi / \lambda_s, \quad (1.9)$$

we have

$$2\pi / \lambda_s = 4\pi / \lambda \sin \theta \quad (1.10)$$

And, the Bragg condition is defined by :

$$2\lambda_s \sin \theta = \lambda / n \quad (1.11)$$

Which yields the desired Bragg angle definition:

$$\theta_B = \sin^{-1} (\lambda / 2n\lambda_s) = \sin^{-1} (\lambda f_c / 2nv) \quad (1.12)$$

B- Deflection angle of the diffracted beam

When the laser beam reaches the Bragg cell at the right Bragg angle, and after the light- sound interaction has occurred, the output of the Bragg cell is composed of two orders: a diffracted first order, and a non-diffracted zeroth order. In our case, we are interested in the first order diffracted laser beam. This laser beam should be deflected according to the sound frequency applied to the Bragg cell transducer.

When the sound frequency is changed by Δf_s , from f_s to $f_s + \Delta f_s$, there is a change in the magnitude of the sound vector equal to $\Delta k_s = 2\pi(\Delta f_s) / v$ [1], as shown Figure 1.3. This change in the sound vector results in a small angle change $\Delta\theta$.

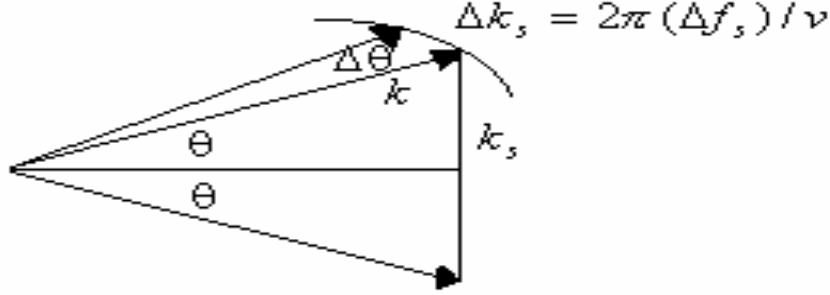


Figure 1.3. Momentum diagram

The incident laser beam direction is kept unchanged during the whole experiment, while the magnitude of the diffracted vector k experiences only a small change of the order of 10^{-10} or less, and therefore, is considered to stay unchanged. The beam will be diffracted along the direction that least violates the momentum conservation principle. For small incident Bragg angles θ , and small changes $\Delta\theta$, the deflection angle is proportional to the frequency of the input acoustic wave and can be found as

$$\Delta\theta = (\lambda * \Delta f_s) / (n * v) \quad (1.13)$$

The direction of the diffracted beam can be controlled by the frequency of the acoustic wave, which is the frequency of the electrical signal applied to the piezoelectric transducer.

The deflection angle is given by

$$\Theta_D = \lambda f / (nv) - 2\Theta_B \quad (1.14)$$

Acoustic velocity inside the medium varies depending on the mode and propagation direction of the acoustic wave inside the cell. In the setup available in our laboratory, a shear wave is generated implying a velocity of the sound equal to 617m/s.

Expression for the deflection angle can also be rewritten as:

$$\Theta_D = \lambda f / (nv) - 2 * (f_c \lambda / 2nv), \quad (1.15)$$

that is equivalent to:

$$\Theta_D = \lambda / (nv) * (f - f_c) \quad (1.16)$$

Equation (1.16) expresses the deflection output in term of the input frequency without reflecting any dynamics. A delay function has to be added to the above relation to simulate the delay needed for the acoustic wave to reach the input laser beam passing through the crystal. It is also necessary to introduce a lag filter representing the response time needed, to change the position of the diffracted beam while the acoustic wave propagates across it. As a result, the transfer function, relating the deflection angle to the input sound frequency, is:

$$G(s) = \Theta_D / (f - f_c) = [\lambda / (nv)] * [k / (k + s)] e^{-s\tau} \quad (1.17)$$

Parameters of the lag filter and delay function are to be defined later.

C-Intensities of the diffracted orders:

When the cell is in the Bragg regime, only two orders are expected, however, depending on the value of Q, the intensity of the diffracted beam will vary. It increases as the Klein-Cook parameter is getting larger than 2π ; if Q is equal to 2π or smaller, more diffracted beams are generated by the cell reducing the power of the first diffracted order.

To describe the distribution over the scattered orders in the Bragg regime, a set of coupled differential equations [2] can be written as follows

$$\frac{dE_n}{d\xi} = \frac{-j\alpha}{2} \{ e^{-j(n-1)Q\xi} E_{n-1} + e^{jnQ\xi} E_{n+1} \} \quad (1.18)$$

Where n - the order of the scattered beam,

Q - Klein-Cook parameter,

α^\wedge - phase peak delay in the medium,

ξ - normalized position of the beam inside the cell.

We are interested in the case when $\xi = 1$ that corresponds to the output of the Bragg cell. The phase peak delay is defined by:

$$\alpha^\wedge = \frac{Ck_mSL}{2}, \quad (1.19)$$

Where C is given by $C = -n_0^2 * p$,

p - strain-optic coefficient of the medium,

k_m - light propagation constant,

S - sound field amplitude,

L - interaction length of the cell defined by the transducer size.

When $Q \gg 2\pi$, the cell is considered to be in the Bragg regime. In reality, Q is finite and in many instances can be slightly greater than 2π (this especially applies to the case when a large steering range needs to be achieved). This is considered to be a deviation from the conditions traditionally viewed as “nominal.” The general trend is to concentrate the optical energy in the immediate spatial neighborhood of the zeroth order. Therefore, truncation of much weaker higher diffracted orders creates negligible numerical errors. Applying (1.18) to the first five scattered orders, we obtain the following equations for $E_{-2}, E_{-1}, E_0, E_1, E_2$ [2]:

$$\begin{aligned} \frac{dE_2}{d\xi} &= \frac{-j\alpha^\wedge}{2} \{e^{-jQ\xi} E_1 + e^{j2Q\xi} E_3\} \\ \frac{dE_1}{d\xi} &= \frac{-j\alpha^\wedge}{2} \{E_0 + e^{jQ\xi} E_2\} \\ \frac{dE_0}{d\xi} &= \frac{-j\alpha^\wedge}{2} \{e^{jQ\xi} E_{-1} + E_1\} \end{aligned} \quad (1.20)$$

$$\frac{dE_{-1}}{d\xi} = \frac{-j\alpha}{2} \{e^{j2Q\xi} E_{-2} + e^{-jQ\xi} E_0\}$$

$$\frac{dE_{-2}}{d\xi} = \frac{-j\alpha}{2} \{e^{j3Q\xi} E_{-3} + e^{-j2Q\xi} E_{-1}\}$$

The set of coupled differential equations defined by (1.18) can be solved numerically for a given number of diffracted orders to demonstrate how the change of Q affects intensity distribution among them. The following figures show how intensities vary when a Klein-Cook parameter is changed, and the phase-shift delay is assumed to be equal to 4 [2] For the sake of simplicity only six diffracted orders are used along with the non-diffracted order.

Figure 1.4 presents numerical results for $Q=2\pi$. It is seen from the figure that there is a noticeable amount of intensity in scattered orders other than the two orders of interests. At the output of the Bragg cell intensity of the first diffracted order is approximately 84% of that of the incident light (which corresponds to 84% diffraction efficiency). The remaining 16%

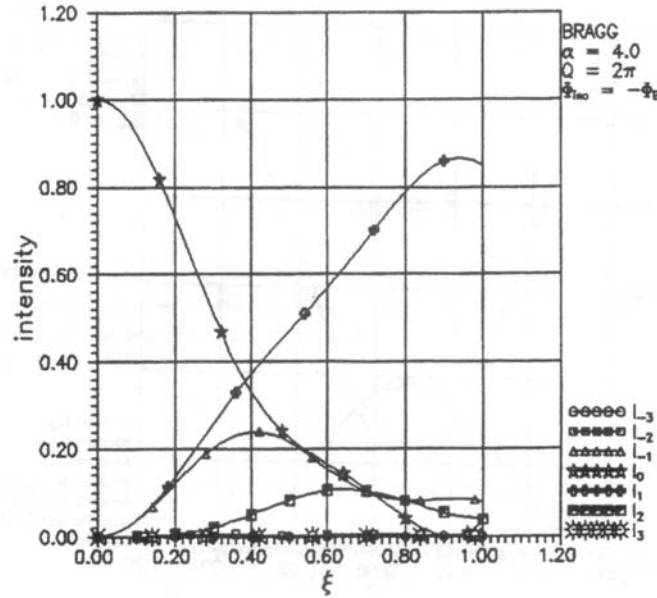


Figure 1.4. Intensity distribution for $Q=2\pi$

is distributed among the other diffracted beams. This situation corresponds to the boundary line between the Bragg and Raman-Nath regimes of operation. Figure 1.4

illustrates that by selecting a proper value for d we can put a significant portion of intensity into the first order. Figure 1.5 presents the results when the Klein-Cook parameter is changed to 4π and the system is “deeper” in the Bragg mode. As can be seen from this numerical solution, higher order diffracted beams start “fading” compared to those in Figure 1.4. At the same time intensity of the first order diffracted beam at the output of the Bragg cell practically does not change and stays around 84% of the incident light intensity.

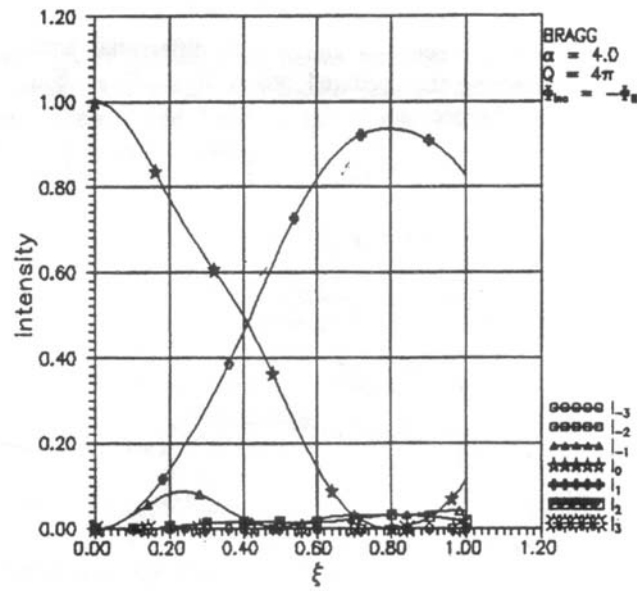


Figure 1.5. Intensity distribution for $Q = 4\pi$

Figure 1.6 presents the case when the Klein-Cook parameter is set to 8π

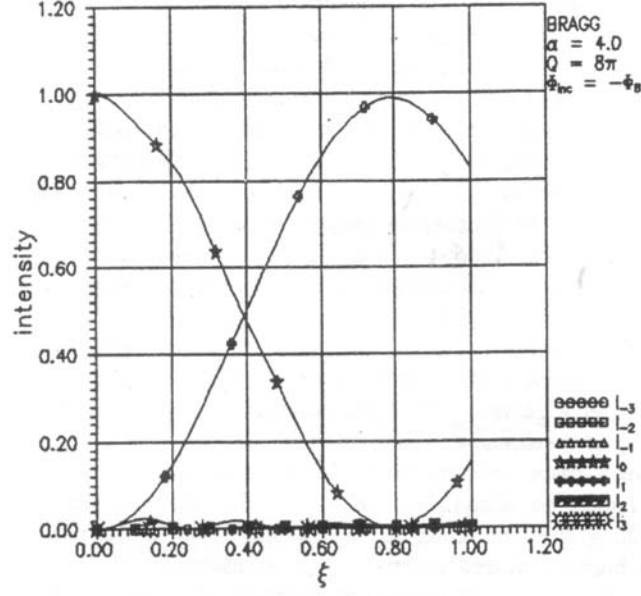


Figure 1.6. Intensity distribution for $Q = 8\pi$

When Q is equal to 8π , essentially only the two orders of interest are present, while the other scattered beams practically “fade out”. Another interesting observation from Figure 6 is the fact that the intensity of the diffracted laser beam I_1 remains virtually unchanged getting 84% of the incident beam intensity. However, the presence of the other orders affects the intensity that falls into the zeroth non-diffracted order. Therefore, as the figure of merit Q is changed within the near-Bragg regime in the output of the cell we observe redistribution of intensities among the scattered beams except I_1 that practically does not change.

Ideally, if Q were set to infinity, the set of coupled equations defined by (1.18) would get reduced to [2]:

$$\frac{dE_0}{d\xi} = \frac{-j\alpha}{2} \{E_1\} \quad (1.21a)$$

$$\frac{dE_1}{d\xi} = \frac{-j\alpha}{2} \{E_0\} \quad (1.21b)$$

Solving for the two orders yields:

$$E_0 = E_{inc} * \cos\left(\frac{\alpha\xi}{2}\right) \quad (1.22a)$$

$$E_1 = -j * E_{inc} * \sin\left(\frac{\alpha \xi}{2}\right) \quad (1.22b)$$

The above equations are consistent with the numerical results presented above. Indeed, beam intensity can be found by raising its spectrum E to the second power, hence

$$I_0 = I_{inc} * \cos^2\left(\frac{\alpha \xi}{2}\right) \quad (1.23a)$$

$$I_1 = I_{inc} * \sin^2\left(\frac{\alpha \xi}{2}\right) \quad (1.23b)$$

I_0 and I_1 in Figure 1.6 are described by equations (1.23) for $d = 4$. Moreover, it can also be demonstrated that (1.23b) can be used to estimate I_1 in the cell output. For $d = 4$ and $\xi = 1$

$$I_1 = I_{inc} * \sin^2\left(\frac{4 * 1}{2}\right) = 0.83 * I_{inc},$$

which practically matches the results presented in Figures 1.4 – 1.6.

1.2. Assessment Of The Environmental Effects On The Efficiency And Performance Of The Bragg Cell System

A-Vibrations effects:

A 2-dimensional Bragg cell based steering system is intended for satellite-borne applications. It will, therefore, experience some vibrations due to the satellite platform jitter. Spectrum of these vibrations does not exceed 2-3Khz. The system does not have any moving parts; therefore, there is practically no vibration of the laser source with respect to the steering device. The only possible effect on the Bragg cell is addition of these disturbances to the vibration spectrum of the transducers. The fact that frequencies of external vibrations are small compared to the drive frequencies of the Bragg cell (usually of the order of tens of MHz), their effect is virtually zero, and functioning of the steering device itself is not altered by the satellite platform jitter. However, due to displacements of the entire system caused by vibrations, beam positioning may become inaccurate. These disturbances can be eliminated by the use of adaptive control techniques that will be discussed later.

B-Temperature effects:

The Bragg cells used in our laboratory are made from Tellurium Dioxide. The thermal expansion coefficient of this material is $19.5 \cdot 10^{-6}$ per degree Kelvin at $290^\circ K$, with a melting point of $1006^\circ K$. In addition, the hardness coefficient of the material is $4 \text{ M}\Omega$. Using this type of Bragg cells for satellite communications purposes requires special measures to create an environment suitable for device operation and preventing the cell from experiencing critical temperature changes. When exposed to higher temperatures the cell expands, thus changing the interaction length L . Since the operation temperature range is not large, linear expansion can only be a small fraction of a percent. Thermal expansion of the cell does not affect the deflection angle as can be seen from (1.16) and (1.17). On the other hand, the Klein-Cook parameter Q is a function of L . However, if Q is large enough, and the change of L is very small, then performance of the steering device will not be affected. It has been demonstrated in Figures 1.4 – 1.6 that even such significant changes of Q as from 2π to 4π and then to 8π did not change intensity of the first diffracted order in the output of the cell. Another parameter affected by L as per (1.19) is the phase peak delay $\hat{\alpha}$. It is seen from (1.23b) that intensity of the first diffracted order is directly affected by this parameter; however, since the change of $\hat{\alpha}$ is so negligible, I_1 is practically not affected.

C-Effects of the acoustic power on the diffraction efficiency:

For isotropic Bragg diffraction assuming that the incident angle is equal to the Bragg angle as shown in Figure 1.1, the diffraction efficiency η can be expressed in terms of the acoustic power P_a as [3]:

$$\eta = \sin^2\left(\frac{\nu}{2}\right) \quad (1.24)$$

$$\nu = \frac{2\pi}{\lambda_0} * \frac{1}{\cos\theta} * \left[\frac{M_2 L}{2H} * P_a \right]^{1/2} \quad (1.25)$$

Where M_2 - acousto-optic figure of merit corresponding to the Tellurium Dioxide material

of the Bragg cell. For isotropic diffraction, with a shear acoustic wave, and a circularly polarized optical wave M_2 is equal to $1200 \cdot 10^{-15} \text{ s}^3 / \text{kg}$.

λ_0 - incident laser beam wavelength

L and H - dimensions of the acoustic transducer as presented in Figure 1.7.

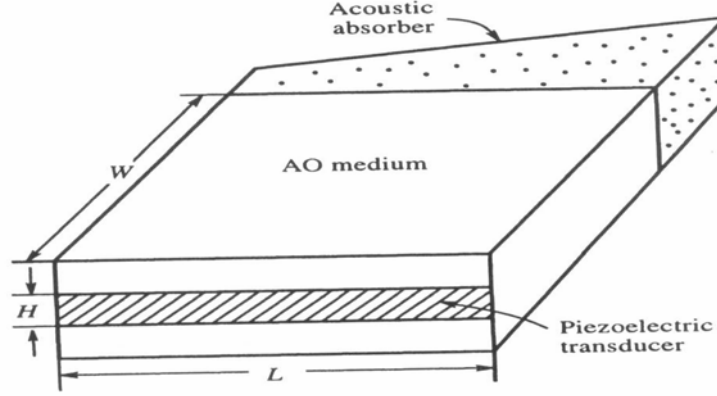


Figure 1.7. Dimension of the AO medium and the piezoelectric transducer

The diffraction efficiency is thus given by:

$$\eta = \sin^2 \left\{ \frac{\pi}{\lambda_0 \cos \theta} \left[\frac{M_2 L}{2H} P_a \right]^{\frac{1}{2}} \right\} \quad (1.26)$$

Equation (1.24) is a trigonometric function that has a maximum when its argument is equal to $\pi/2$. In other words, parameter v defined by (1.25) should be close to π . It can be demonstrated that in the cases of small diffraction efficiency v is less than π ; therefore, it needs to be increased. Let us consider two cases:

a) Constant acoustic power:

At a constant acoustic power, achieving an increase in the diffraction efficiency requires the use of a material that has a high figure of merit M_2 [3]. Choosing an acoustic transducer that has a lower height H and a longer length L can also increase the efficiency. One can also notice that a higher efficiency is obtained using laser beams with lower wavelength [3].

b) Modulation of the diffracted order:

The diffraction efficiency of the cell can be achieved by changing the acoustic power. As a result, modulation can be implemented by changing the acoustic power especially if the efficiency is small (<50%) [3]. Indeed, if η is small, then using the fact that $\sin x \approx x$, the efficiency equation can be reduced to:

$$\eta = \frac{\pi^2 M_2 L}{2 \lambda_0 H} P_a \quad (1.27)$$

offering a linear modulation. In the case when efficiency is larger, the modulation expression can be derived from (1.25) by equating v to π as follows:

$$P_a = \frac{H * \lambda_0^2 * \cos^2 \theta}{2 * M_2 * L} \quad (1.28)$$

Note: The power consumption of the Bragg cells used in our laboratory is 400 mW for each device.

1.3 Conclusion

In this portion of the research project a number of tasks has been accomplished. Theoretical study of the acousto-optical phenomena has been conducted. Based on the equation of physics describing the process of sound-light interaction a mathematical description of the Bragg cell has been developed. Special attention has been given to the case when the cell operates in the near-Bragg regime. It has been demonstrated that even when the device deviates from the “nominal” conditions it is still possible to achieve high diffraction efficiency. It has also been shown that the factor responsible for inertia of the cell is the propagation delay of the sound wave inside the crystal, and therefore, is a function of dimensions of the cell as well as acoustic velocity. Accuracy of the device is very high for a small steering range. For small angles the relationship between the acoustic frequency and the deflection angle is linear as has been shown by (1.13) – (1.16). Therefore, the accuracy is determined purely by the capability of the device driver to generate the required acoustic frequencies. It is also obvious from (1.13) – (1.16) that resolution of the system depends on the frequency resolution of the driver. Section 1.3 of this report has demonstrated 2 approaches to power management. One of them implies constant acoustic power, however, this approach requires that the amplitude of the acoustic signal for all frequencies is large enough so that the wave does not attenuate too

much before reaching the beam. Attenuation is proportional to the frequency, therefore, the largest frequency value should be used to select acoustic power, however, it will be excessive for lower frequencies. Another approach suggests modulation as presented by (1.28). Assessment of environmental effects on the efficiency and performance of the Bragg cell has been performed. This task has resulted in obtaining a theoretical mathematical model of the Bragg cell described by (1.17), (1.18), (1.23).

REFERENCES

- [1] A. Yariv, *Optical Electronics*, CBS College Publishing 1985.
- [2] S. Chen, M.R. Chatterjee, “A Numerical Analysis and Expository Interpretation of the Diffraction of Light by Ultrasonic Waves in The Bragg and Raman-Nath Regimes Using Multiple Scattering Theory”, *IEEE Transactions* Vol.39, pp 56-68, (1996).
- [3] J. Xu, R. Stroud, *Acousto-Optic Devices: Principles, Design and Application*, John Wiley & Sons, 1992

2. EXPERIMENTAL ANALYSIS AND CHARACTERIZATION OF THE LASER BEAM POSITIONING SYSTEM COMPONENTS

2.1. Experimental Analysis And Characterization Of The Bragg Cell

A number of measurements has been performed to estimate dynamics and statics of the Bragg cell. The model suggested as a result of theoretical study of the acousto-optic phenomena uses change of the acoustic frequency of the transducer as an input and deflection angle of the laser beam as an output and has the following form:

$$G(s) = \theta_D / (f - f_c) = \lambda / (nv) * [k / (s + k)] * e^{-s\tau}, \quad (2.1)$$

Where θ_D – deflection angle;

f – acoustic frequency of the transducer;

f_c – center frequency of the Bragg cell (24 MHz);

λ - wavelength of the incident beam (670 nm);

n – refraction index (2.26);

v – acoustic velocity in crystal medium (617 m/sec);

k – parameter of the lag filter modeling propagation of the acoustic wave across the laser beam;

τ - parameter of the delay function reflecting the time that the acoustic wave propagates from the transducer to the laser beam.

The laser positioning system used for experimentation is presented in Figure 2.1. The first set of measurements has been performed to verify the values of the deflection angles as we change acoustic frequency applied to the crystal. For this purpose a quadrant detector has been placed at a distance $d=87$ cm from the Bragg cell. Acoustic frequency has been set to the smallest available value (18 MHz), and position of the detector has been adjusted so that the beam is right in the middle of it. Then acoustic frequency has been changed in increments of 14.58 kHz. Each time after the change the quadrant detector has been repositioned to keep the beam in the middle of it. The exact linear displacement of the quad in the vertical direction Δz has been measured after each step

with a precision of tens of microns. The displacements have been mapped to obtain the corresponding deflection angles.

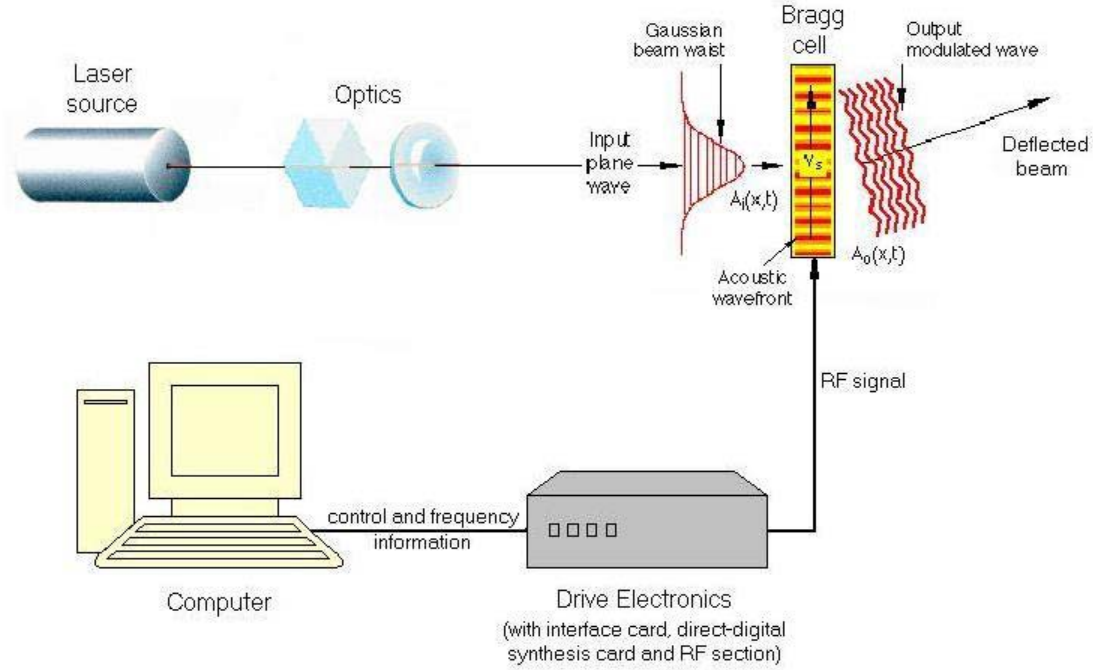


Figure 2.1. Laser Beam Positioning System

Theoretically the deflection angle can be found as follows

$$\theta_D = (\lambda/nv) * (f - f_c) \quad (2.2)$$

While the center frequency of the Bragg cell is 24 MHz, the drive electronics is designed in such a way that it operates in two acoustic frequency bands: 18 – 23.25 MHz and 24.75 – 30 MHz. Fig. 2.2 presents configuration of the detector circuitry. A quadrant detector has been used to transform optical energy of the beam into corresponding electrical signals measured by an oscilloscope. The circuit is configured in such a way that it detects beam deviation only in the vertical direction (elevation channel).

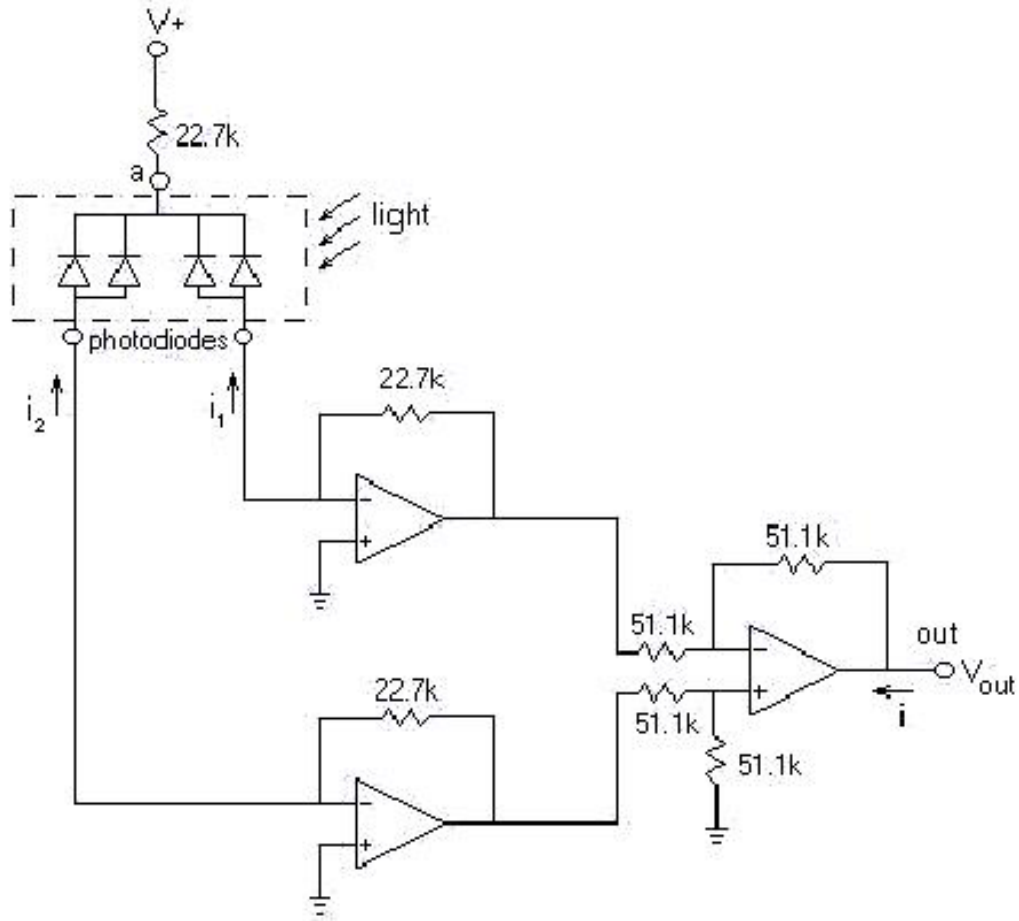


Figure 2.2. Quadrant detector circuit

Figure 2.3 presents theoretical and measured results for the first band. Calculated response of the Bragg cell is shown by a dotted line. As can be seen from the figure that for this frequency range theoretical and experimental values are very close. Results for the second frequency band are presented in Fig. 2.4. While for lower frequencies the measured response tracks the theoretical values, we can see noticeable deviation at higher frequencies. The possible cause of these discrepancies will be discussed later.

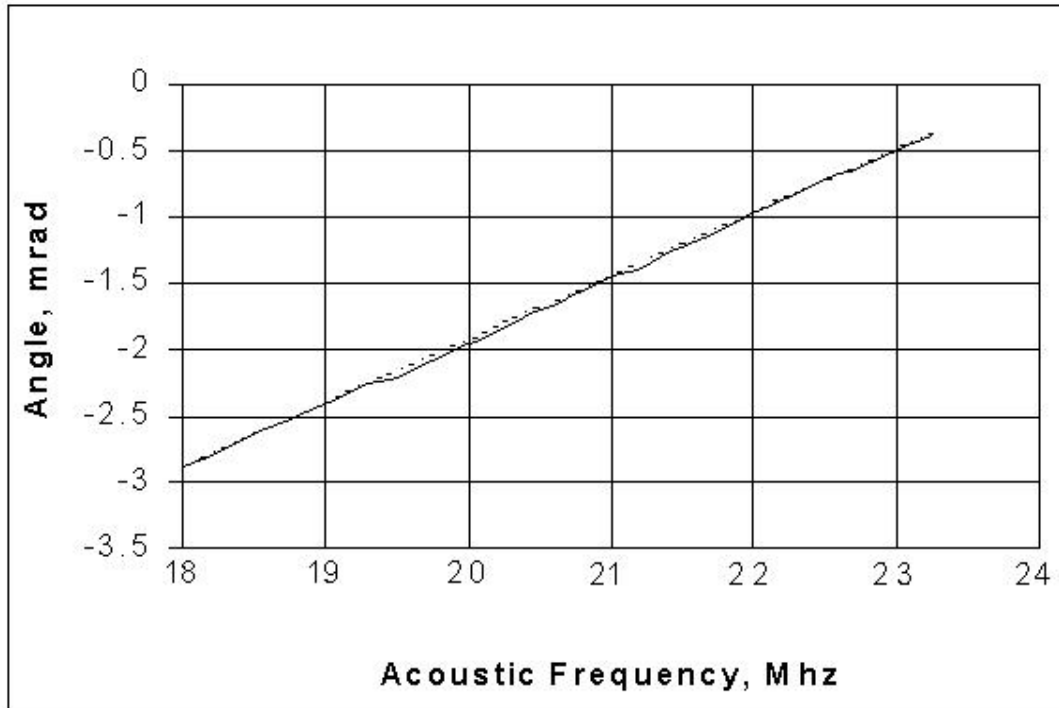


Figure 2.3. Deflection angles for the first frequency band

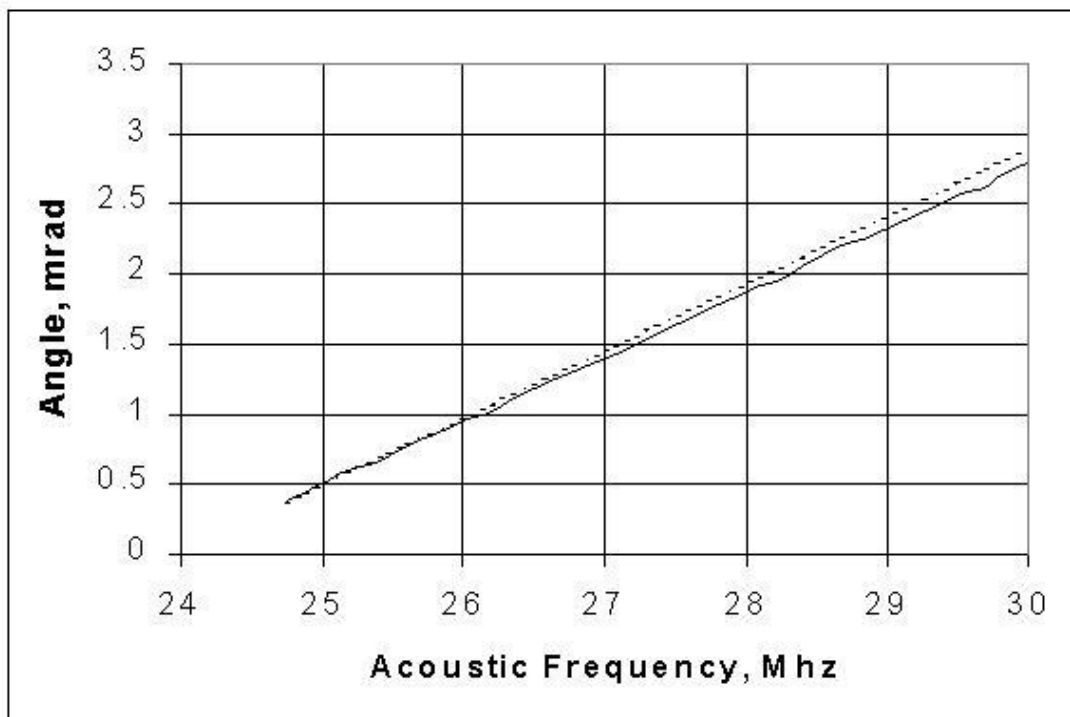


Figure 2.4. Deflection angles for the second frequency band

The next experiment has been performed to obtain step response of the Bragg cell. As an input we applied a rectangular signal (acoustic frequency changing between 20.625 and 27.375 MHz). The result is presented in Fig. 2.5.

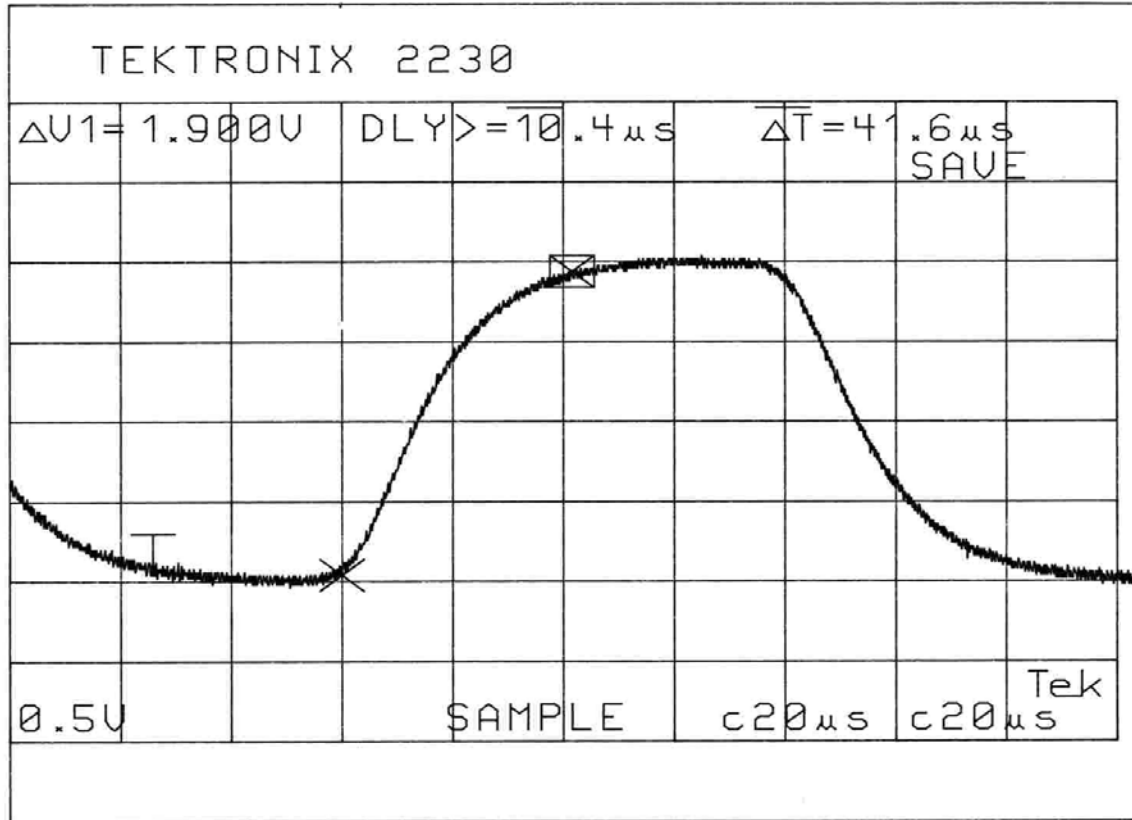


Figure 2.5. Step response of the Bragg cell

The curve presented in Fig. 2.5 may be used to estimate parameter k in equation (2.1), since the above response is associated with transition of the acoustic wave through the laser beam. Settling time of a first order system is related to parameter k as follows.

$$T_{set}=4/k \quad (2.3)$$

For the response presented above $T_{set} = 41.6 \mu\text{sec}$, therefore

$$k = 4/41.6 \cdot 10^{-6} = 96154 \text{ rad/sec.}$$

Another parameter of equation (2.1) that needs to be estimated is τ . It can be defined by performing a series of two experiments with changing beam position relative to the transducer of the Bragg cell. Initially the distance from the transducer to the beam

is 5 mm. We obtain a step response as in the previous experiment. Then the beam is shifted from the transducer by another 5 mm, so the distance is 10 mm. This change increases the propagation delay. The superimposed results of these two experiments are shown in Fig. 2.6.

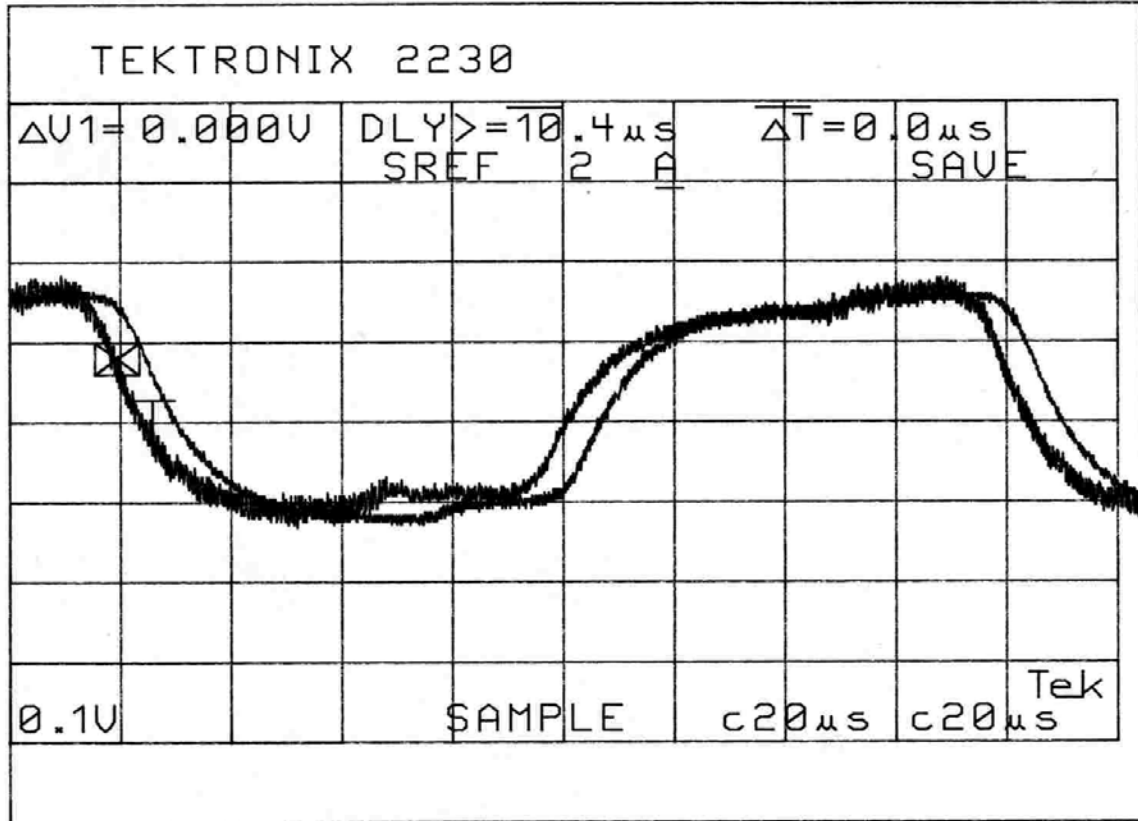


Figure 2.6. Delay estimation experiment

The lagging trace in the above figure represents the second experiment. The time delay τ is approximately $8 \mu s$. This number is consistent with specifications of the Bragg cell crystal. The acoustic wave propagates 5 mm in $8 \mu s$, which corresponds to a speed of approximately 625 m/sec (the nominal value is 617 m/sec).

To ensure that the above measurements represent dynamics of the Bragg cell, we have estimated delay associated with detector electronics presented in Fig. 2.2. Two voltage signals have been measured and superimposed. One of them is at the output of the circuit in Fig. 2.2; the second signal is taken from node *a*. The result is presented in Fig. 2.7.

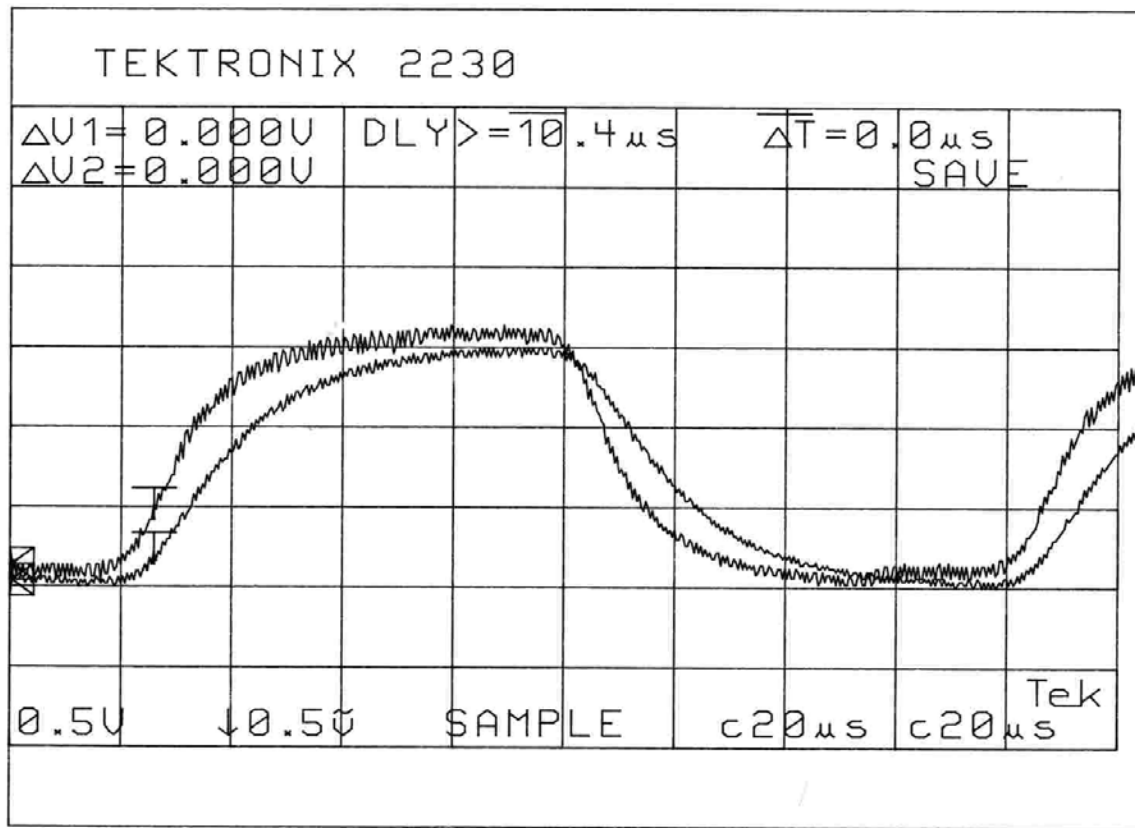


Figure 2.7. Electronics delay experiment

For convenience the signal V_a has been inverted and offset with respect to the output signal. In the above figure the output voltage is represented by the leading trace. This can be explained by direction of currents in the circuit (see Fig. 2.2). Voltage drops from node **out** to node **a**. The path between these two nodes includes resistors and capacitive elements (parasitic capacitances inside the amplifiers). This RC circuit creates a phase lag in the direction from **out** to **a**. Fig. 2.8 presents a zoom-in version of the same measurements.

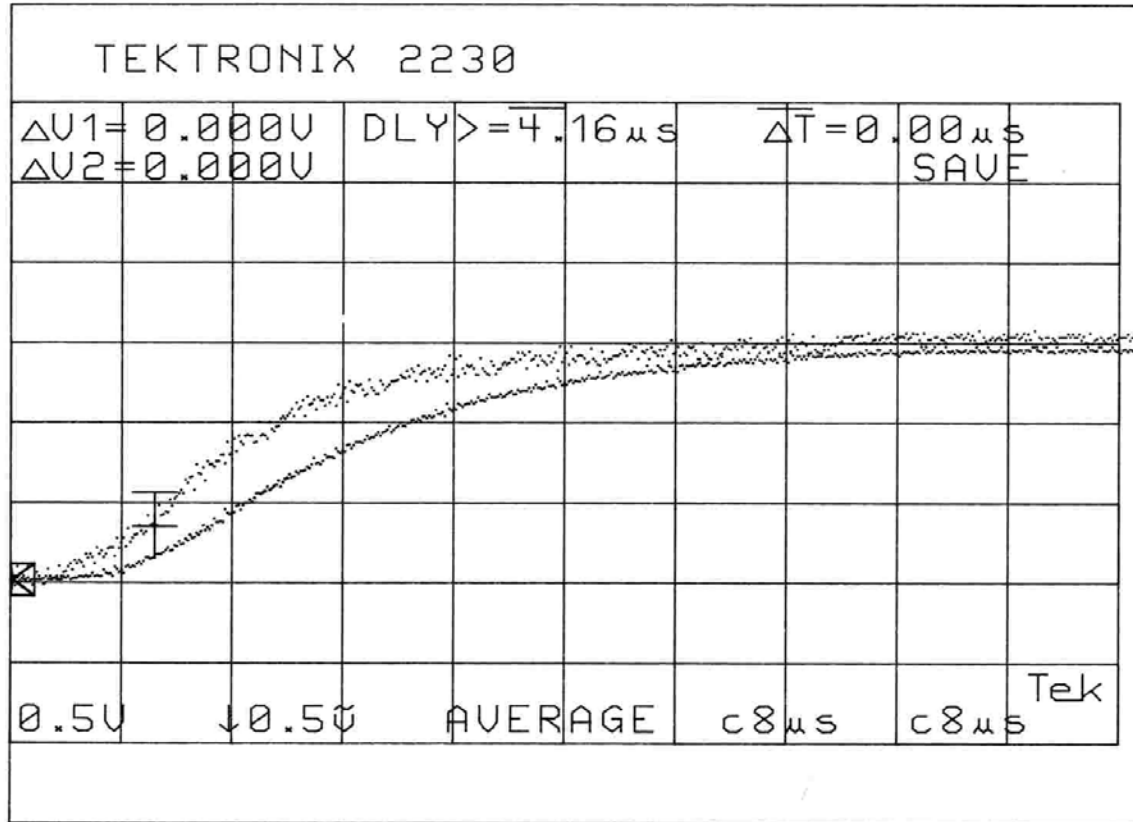


Figure 2.8. Electronics delay (zoom-in)

The time delay associated with detector electronics is approximately $8 \mu\text{sec}$, which is considerably smaller than response time of the Bragg cell. Thus, electronics delay does not interfere with Bragg cell step response measurements presented in Fig. 2.5.

The next set of measurements has been performed to assess optical and acoustic properties of the Bragg cell. RF signals of different frequencies have been applied to the transducer to perform deflection in the horizontal direction. The output beam has been monitored by a CCD camera. The output of the camera has been connected to the oscilloscope to view the response provided by individual pixels. Voltage generated by a pixel of a CCD camera is proportional to the intensity of light illuminating this pixel. Thus, we are able to obtain the intensity profile of the beam after it is deflected by the Bragg cell. Since the camera uses interline transfer mode, we have captured the signals corresponding to one line of pixels, as well as the entire frame of the field of view. The results are presented in Fig. 2.9 – 2.18.

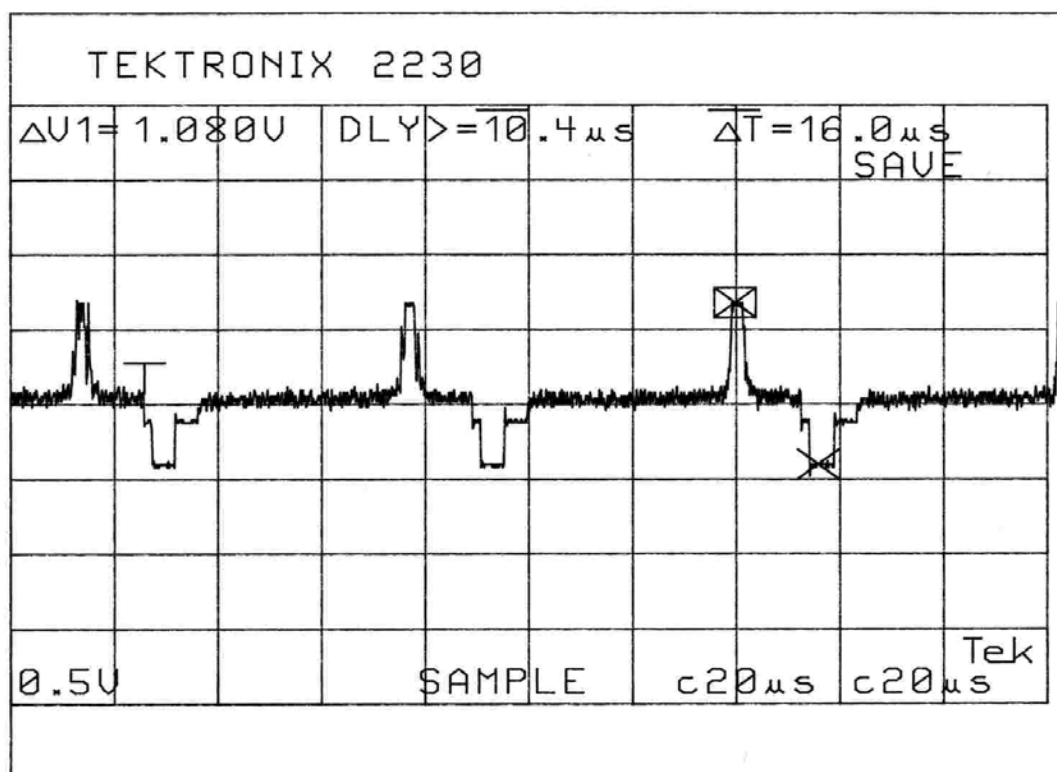


Figure 2.9. Lines of pixels at $f = 18$ MHz

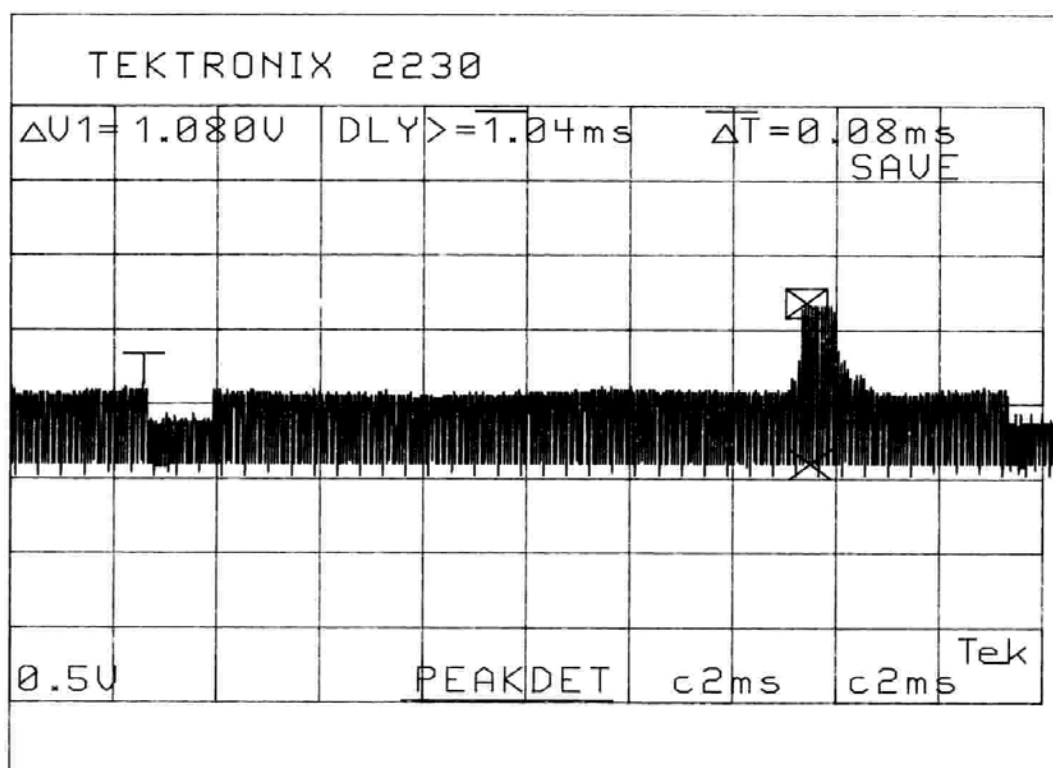


Figure 2.10. One frame at $f = 18$ MHz

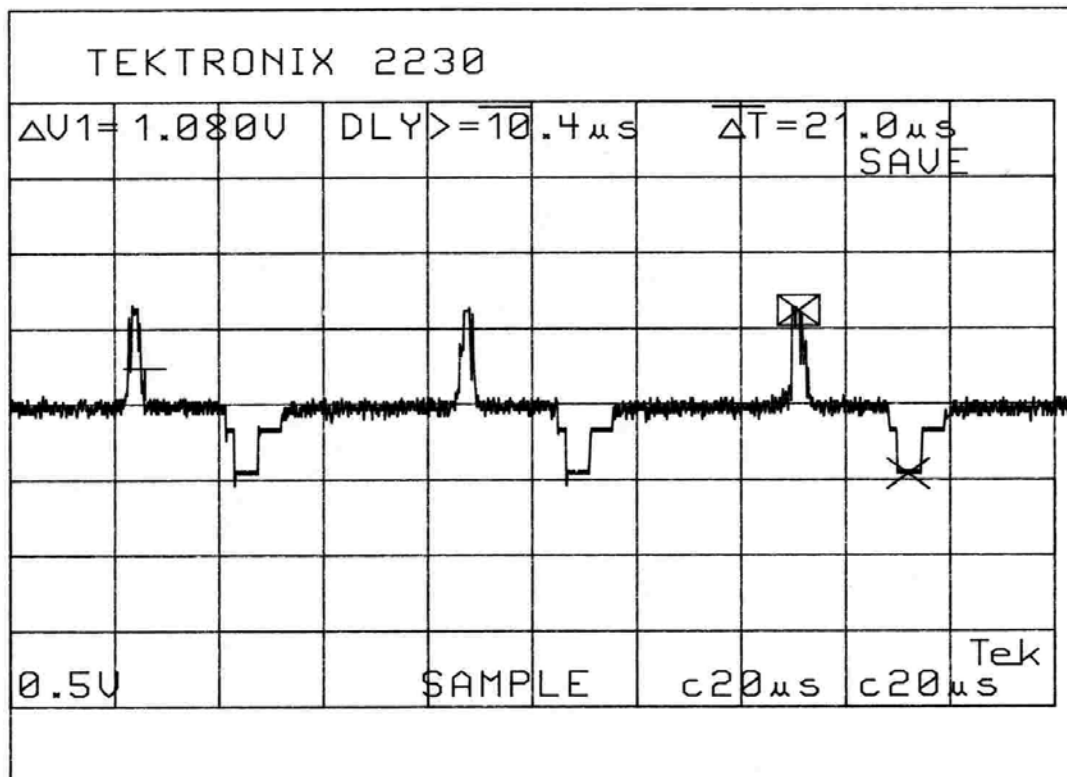


Figure 2.11. Lines of pixels at $f = 21$ MHz

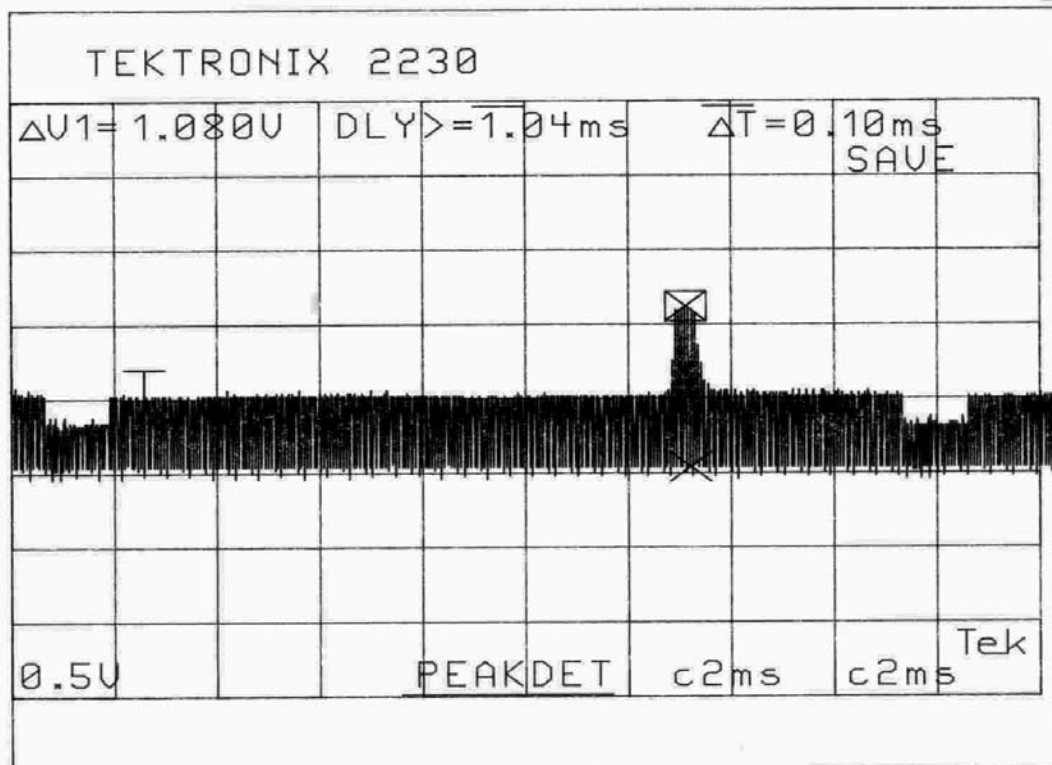


Figure 2.12. One frame at $f = 21$ MHz

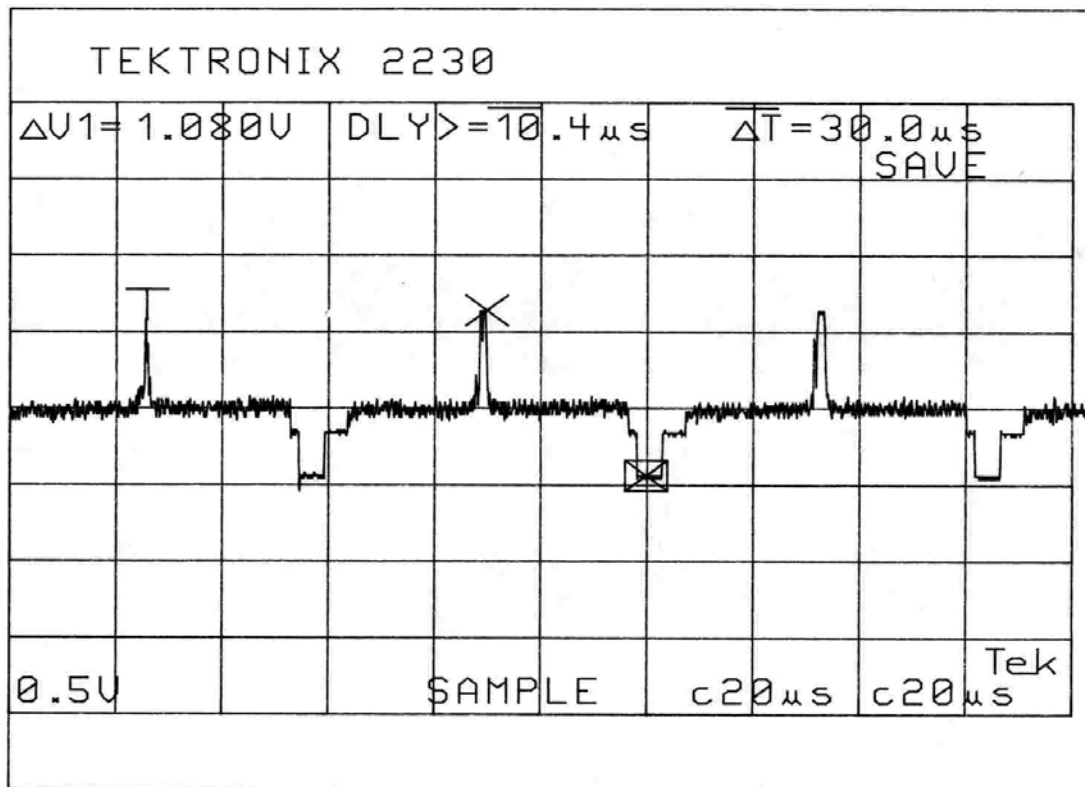


Figure 2.13. Lines of pixels at $f = 24$ MHz

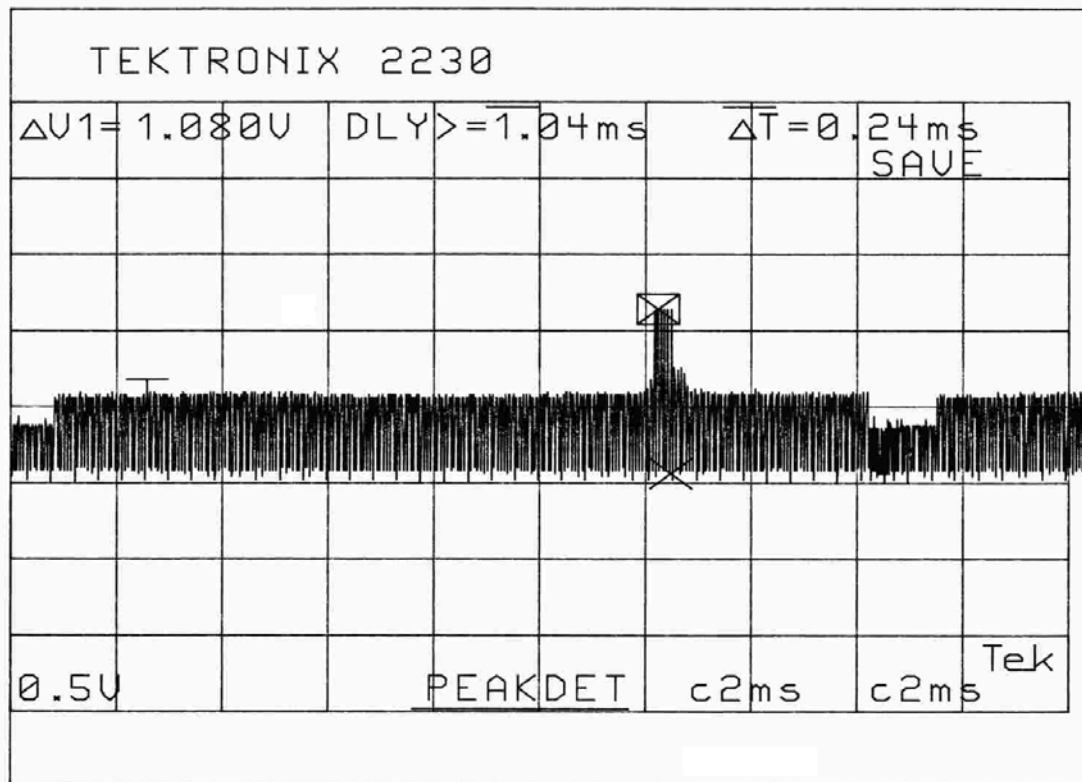
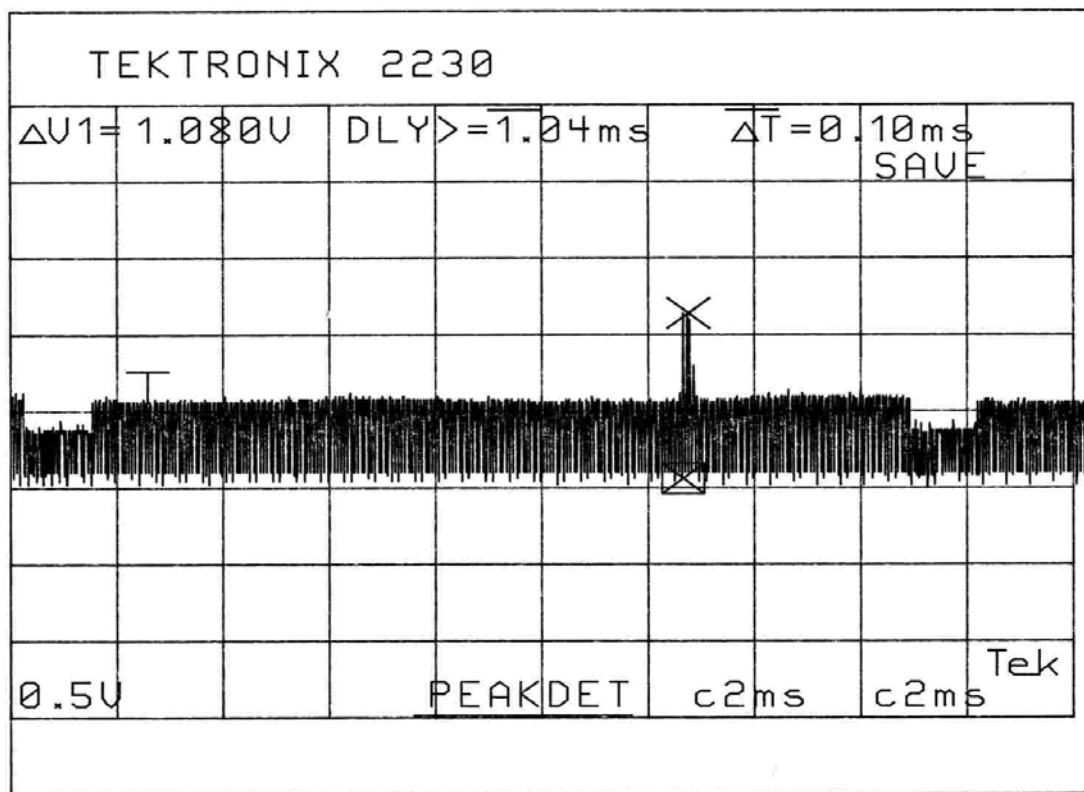
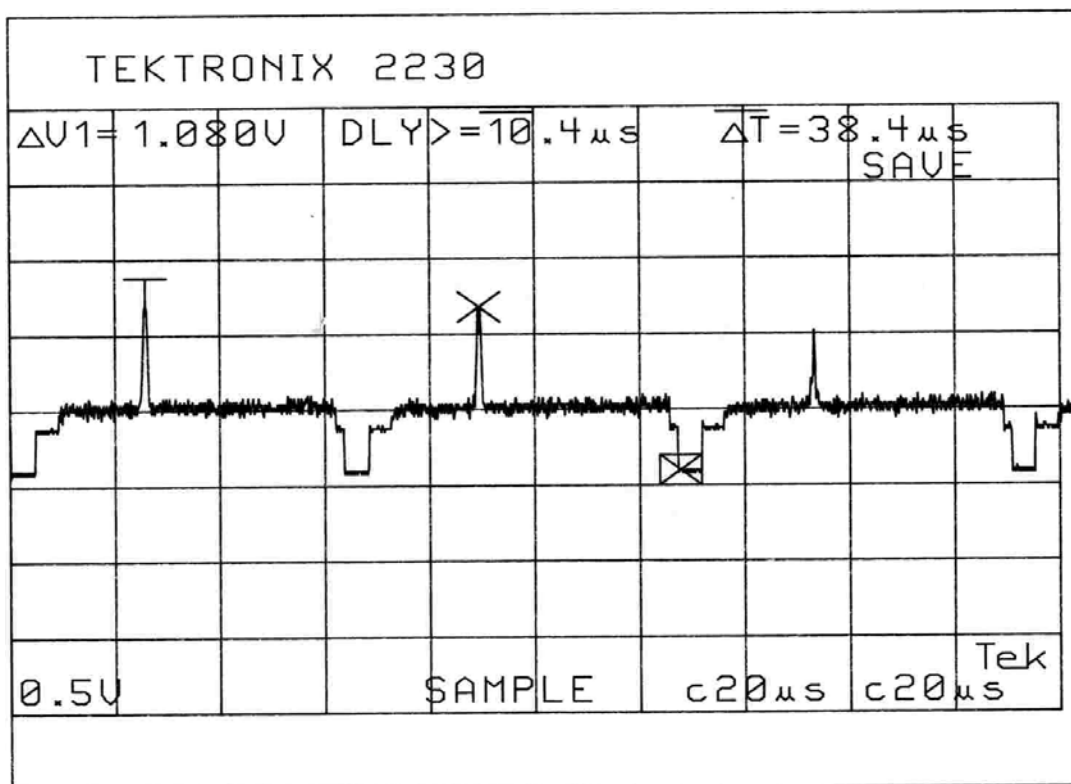


Figure 2.14. One frame at $f = 24$ MHz



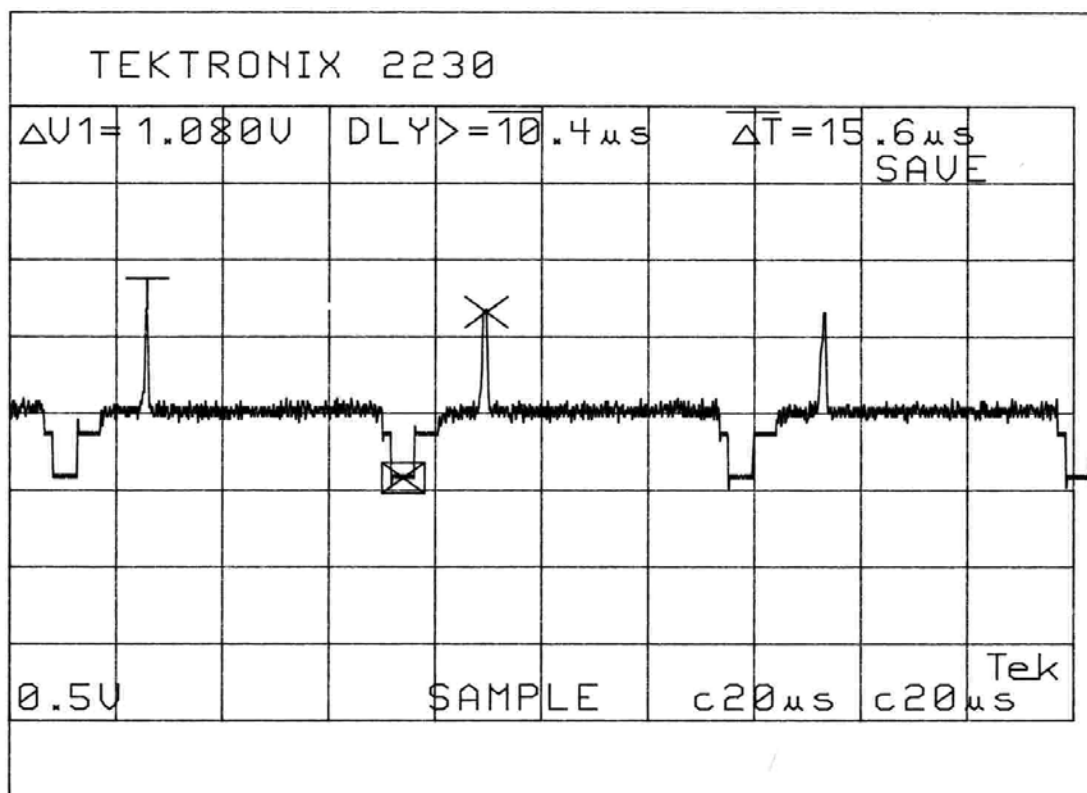


Figure 2.17. Lines of pixels at $f = 30$ MHz

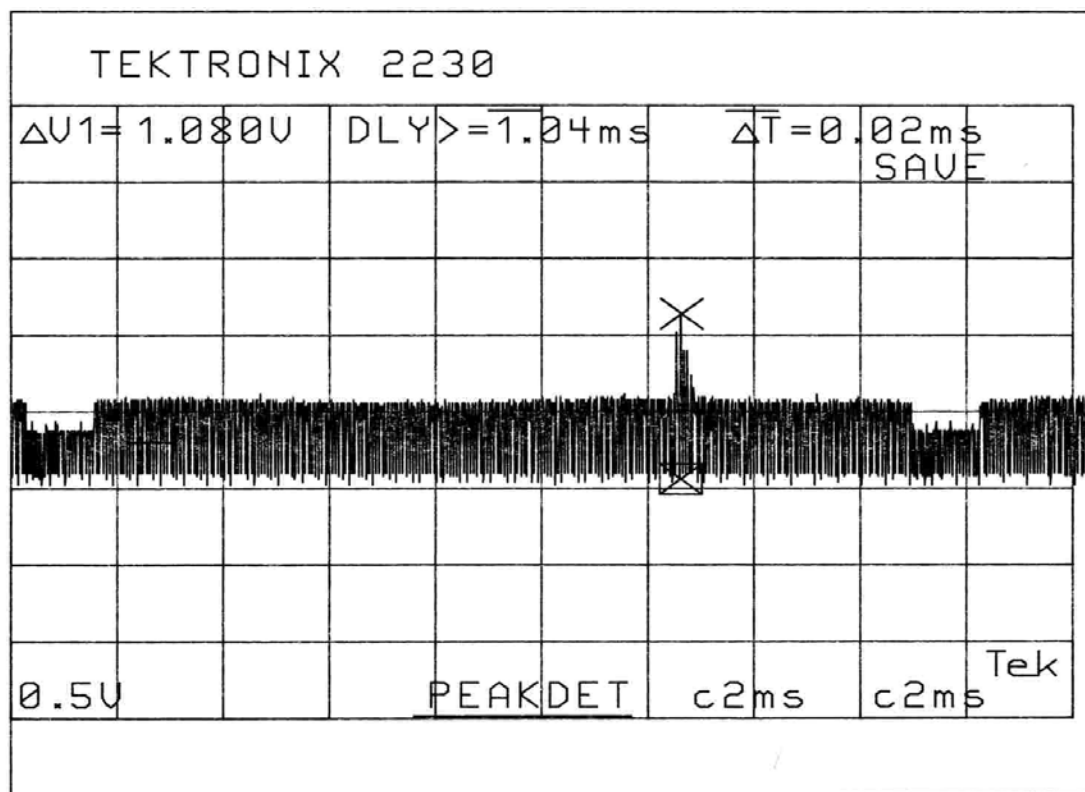


Figure 2.18. One frame at $f = 30$ MHz

For each operating point the first figure presents approximately three lines of pixels. Negative voltages between them are used for synchronization, so that the monitor can distinguish beginning and end of each line. The second figure for each frequency shows the whole frame (all lines stacked together). It also presents intensity profile of the beam .

The following observations can be made. The peak intensity does not change as the acoustic frequency is increased. One can see from Fig. 2.9 – 2.18 that the corresponding voltage signal generated by the CCD camera is always equal to 1.08 V (this is better seen in the figures showing only a few lines of pixels). From the same figures one can see that the peak shifts as we change the frequency (this is due to horizontal steering of the beam). In the figures representing the whole frame we notice some changes in the spatial domain when the acoustic frequency is increased. This is related to acoustic attenuation. The drive electronics is designed in such a way that it applies a constant 400 mW acoustic signal regardless of the frequency. As the acoustic wave propagates through the crystal, it attenuates with attenuation constant being proportional to the square of the sound frequency. It has been shown in Chapter 1 that diffraction efficiency depends on the acoustic power that changes in the direction of acoustic wave propagation. As a result, at higher frequencies when the wave traverses the beam, its power decays faster and diffraction efficiency on the outer side of the beam decreases as can be seen from (1.26). On the other hand, the side of the beam close to the transducer is affected more by the acoustic wave, since the acoustic wave has not attenuated much yet. This is demonstrated in Fig. 2.19.

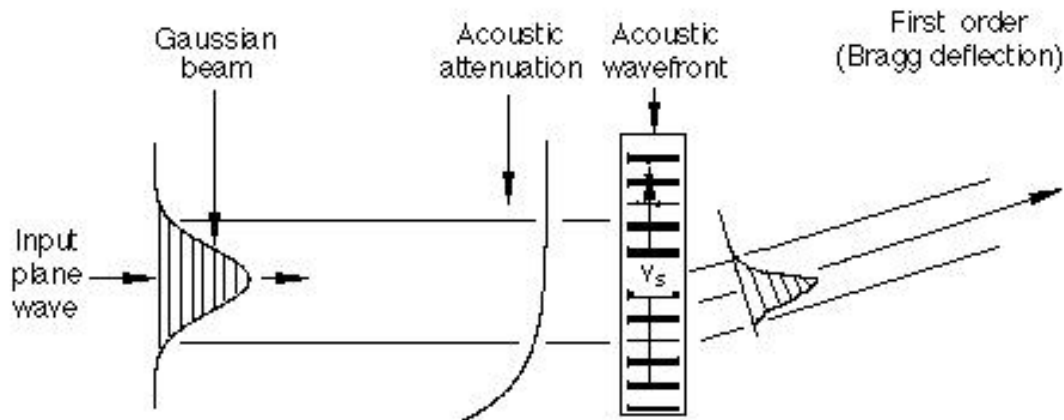


Figure 2.19. Acoustic attenuation effect

The intensity profile distortion of the deflected beam creates an effect of beam shifting (one can see from Fig. 2.19 that the peak intensity is closer to the bottom of the Bragg cell where the transducer is located). When position of this beam is determined using a quadrant detector it appears that the deflection angle is less than it should be theoretically. This is the effect that we observe in Fig. 2.4 at high frequencies, and it is also consistent with the intensity profiles at 27 and 30 MHz presented in Fig. 2.16 and Fig. 2.18. A possible solution to this problem is the use of acoustic signal modulation such that for all frequencies of operation the sound wave does not decay too much while it passes through the beam.

2.2. Experimental Analysis And Characterization Of The Quadrant Detector

2.2.1. Experimental characterization of the quadrant detector

The quadrant detector is a silicon photodiode detector, and is widely used in position sensing [1,2].



Figure 2.20. Silicon Photodiode Quadrant detector RCA C30927E [3]

The photodiode used for our experiments is an RCA C30927E that has four quadrants. Each quadrant generates a voltage. Using these four voltages, as inputs to the circuitry containing operational amplifiers as shown in Figure 2.22, the actual position of the laser beam is sensed. The electronic circuit takes the four voltages as inputs, and outputs two voltages. These two voltages indicate the azimuth and elevation displacements of the laser beam as sensed by the quadrant. Basically, in order to get the elevation output, we compute the difference between the voltages of the two top

quadrants and the two bottom quadrants. The azimuth voltage is computed by subtracting the sum of the voltages in the leftmost quadrants from the sum of voltages in the rightmost quadrants. A schematic representation of the quadrant is shown in Figure 2.21.

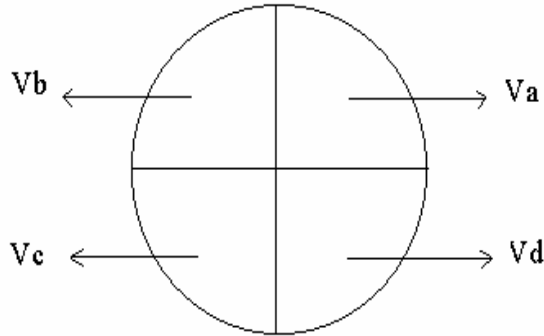


Figure 2.21 Quadrant detector simplified scheme

Using the notation as given in Figure 2.21, the elevation and azimuth voltages generated by the circuit in Figure 2.22 are given by:

$$V_{el} = (V_a + V_b) - (V_d + V_c)$$

$$V_{az} = (V_a + V_d) - (V_b + V_c).$$

A series of experiments have been performed using the quadrant detector to determine the behavior of this optical sensor as the beam is moved across the different quadrants in various directions. The first set of experiments consisted of determining the change in the azimuth and elevation channels as the beam was moved along the horizontal axis, the vertical axis, and finally diagonally.

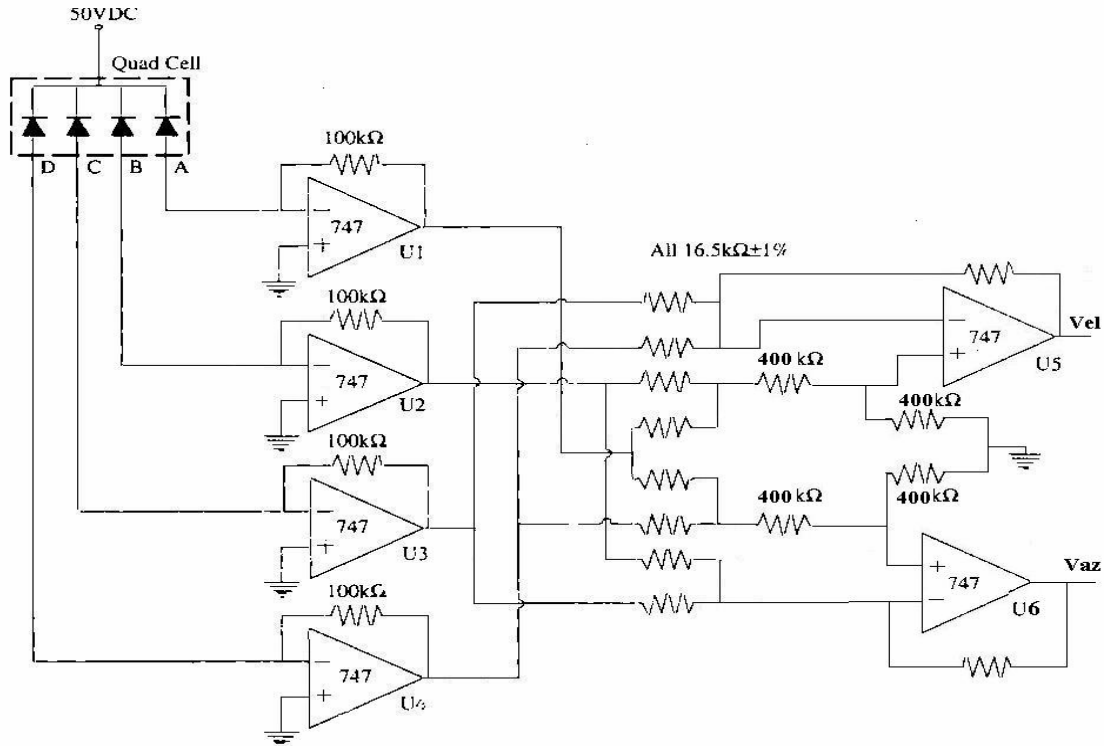


Figure 2.22. The quadrant detector circuitry [4]

The readings in the azimuth channel as the beam is moved along the axes and diagonals of the quadrant detector are presented by the following figures. The quadrant detector has a radius equal to 750 microns; however, the useful radius has been estimated to be approximately equal to 600 microns.

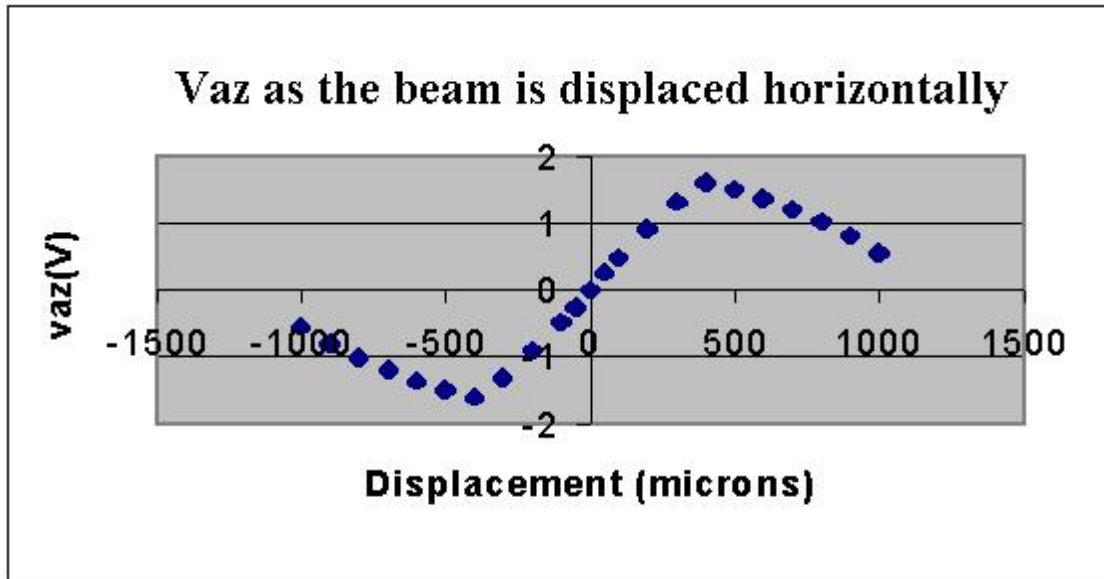


Figure 2.23. Azimuth channel response to horizontal beam displacement ($y=0$)

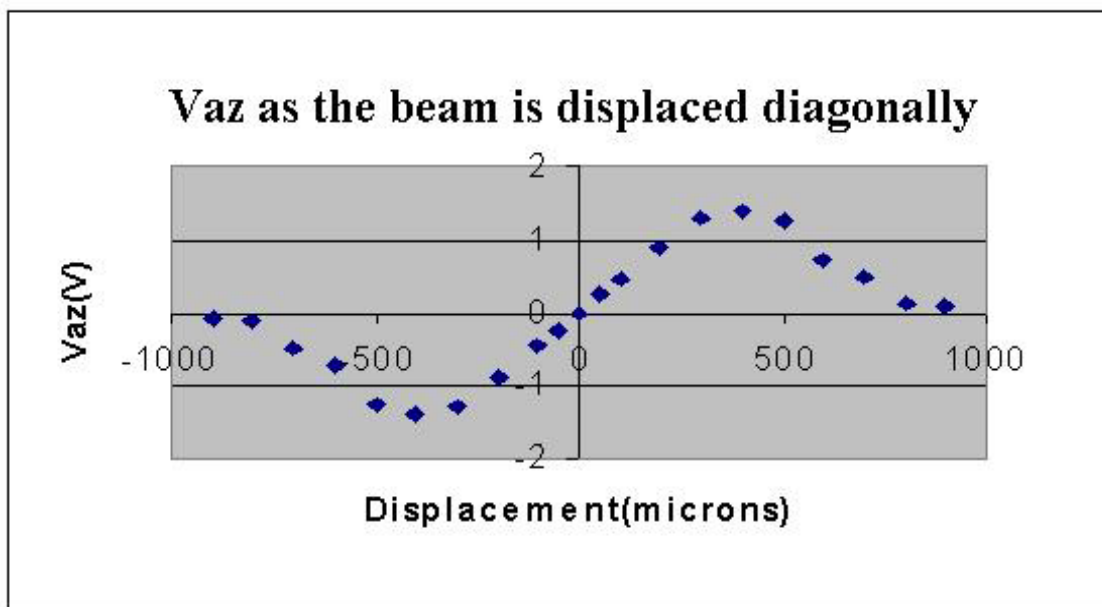


Figure 2.24 Azimuth channel response to diagonal beam displacement ($y=x$)

The reading in the elevation channel, as the beam is displaced along the vertical axis ($x=0$) is the same as that shown in Figure 2.23. Similarly, the reading in the elevation channel as the beam is moved diagonally ($y=x$), is the same as that in the azimuth channel as shown in Figure 2.24. The quadrant detector exhibits coupling between the

two channels. This property is illustrated in Fig. 2.25, representing azimuth channel response. In this experiment the horizontal position is kept at 100 microns, while the elevation position varies from 0 to 1000 microns. It could be seen that although the azimuth position is unchanged, the increase of elevation results in response in the azimuth channel. This phenomenon could be explained by the varying energy distribution pattern between four segments of the quadrant detector.

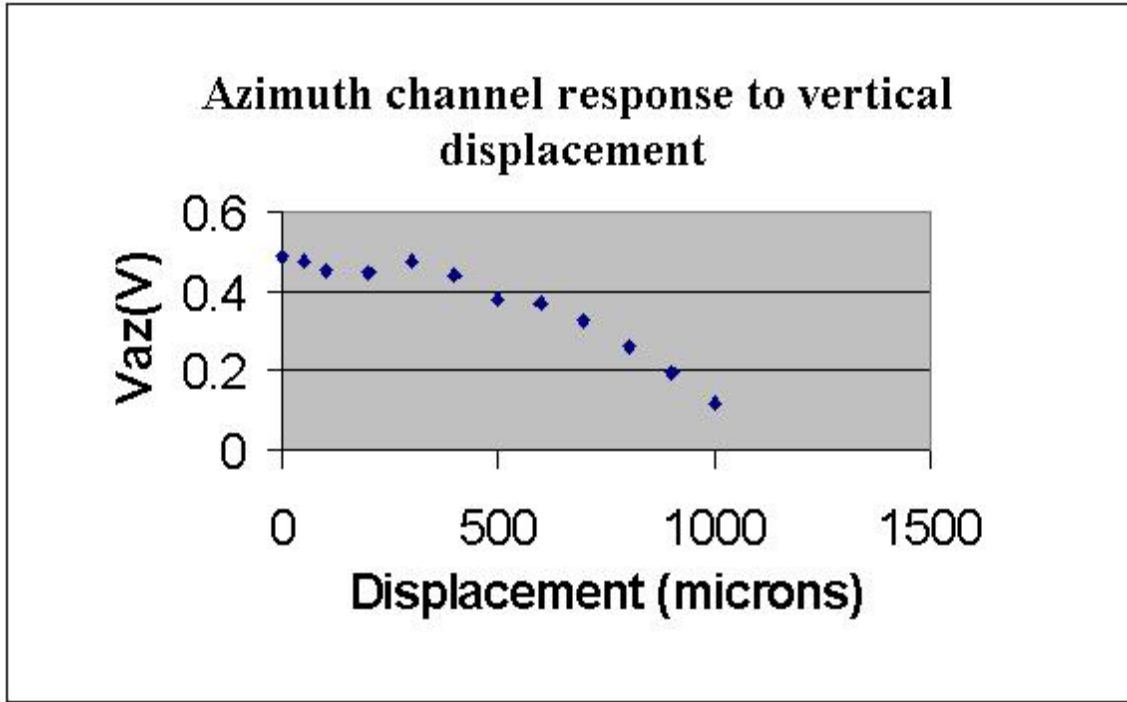


Figure 2.25 Illustration of coupling effect in the quadrant detector

Another experiment with the quadrant photodiode detector has been performed. The laser beam has been steered across one quadrant in both horizontal and vertical directions to obtain the complete characteristics. Fig. 2.26 presents a summary of this experiment. The data have been recorded while moving the beam across quadrant A (see Figure 2.21). These results will be used to set up a mathematical model of the quadrant photodiode detector.

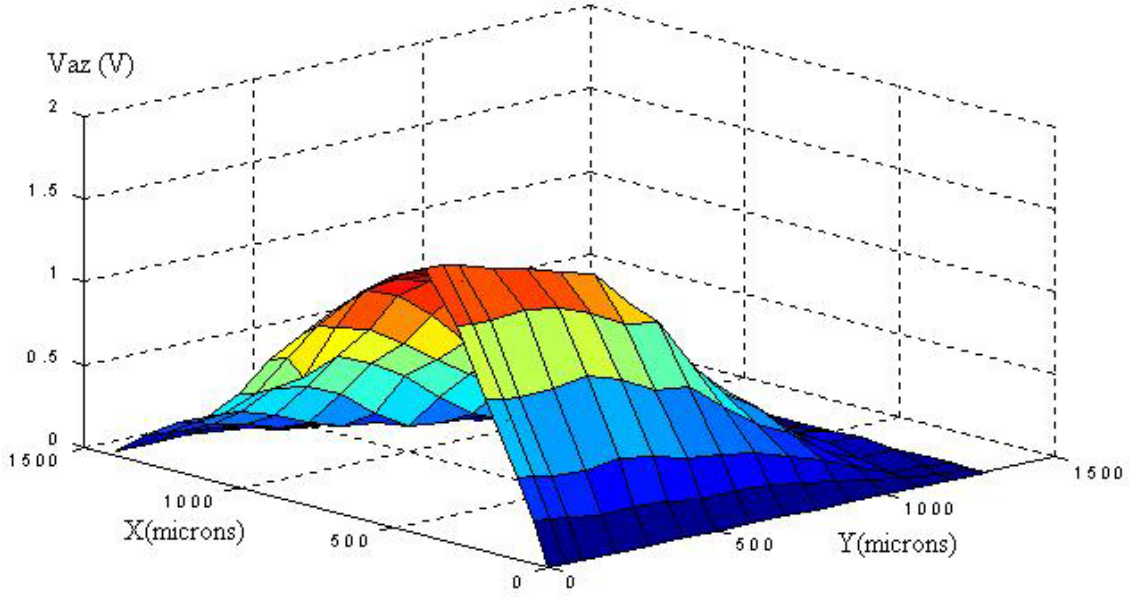


Figure 2.26 Response in the azimuth channel

2.2.2. Mathematical description of the quadrant detector

In order to implement the quadrant detector model, we first tried to come up with an analytical expression that relates the coordinates of the laser beam on the quadrant and the voltage generated in the outputs of the detector. The azimuth and elevation channel outputs are directly related to the energy of the laser beam that falls in each quadrant. This energy can be analytically presented as a double integral of the intensity of the laser beam over the quadrant area. Assuming that the laser beam used as a communication medium has a Gaussian intensity distribution profile, as presented in [5], the energy in each of the four quadrants as defined in figure 2.21 is given by the following equations:

$$E_a = \int_X^{R+X} \int_Y^{\sqrt{R^2 - (x-X)^2} + Y} I_0 \cdot \text{Exp} \left[-2 (x^2 + y^2) / w^2 \right] dy dx$$

$$E_b = \int_{-R+X}^X \int_Y^{\sqrt{R^2 - (x-X)^2} + Y} I_0 \cdot \text{Exp} \left[-2 (x^2 + y^2) / w^2 \right] dy dx$$

$$E_c = \int_{-R+X}^X \int_{-\sqrt{R^2 - (x-X)^2} - Y}^Y I_0 \cdot \text{Exp} \left[-2 (x^2 + y^2) / w^2 \right] dy dx$$

$$E_d = \int_X^{R+X} \int_{-\sqrt{R^2 - (x-X)^2} - Y}^Y I_0 \cdot \text{Exp} \left[-2 (x^2 + y^2) / w^2 \right] dy dx$$

In these integrals, R represents the radius of the quadrant, X and Y - horizontal and vertical coordinates of the laser beam, respectively, I_0 – peak intensity of the beam, w – beam width. Obtaining a closed-form solution is not possible because the result of the inner integrals contains the error function “erf”, that cannot be integrated. Before using numerical approximation to come up with a mathematical model of the quadrant detector, various attempts to solve the double integral analytically have been performed.

A- Analytical model : Approximations methods

The idea of this approach is finding an approximation of the integrant in the equations above that can be double integrated. The intensity of the laser beam has Gaussian distribution. First we used Taylor series expansion to find a good approximation. Representing an exponential expression by a polynomial eliminates the error function from the first integral solution, and a solution to the second integral can be found. This method fails, due to the fact that the Taylor series expansion over two variables gives a valid approximation only in the vicinity of zero, which is less than needed for this application. The approximation has to be valid over a range of values that will at least comprise the total diameter of the quadrant plus the width of the beam.

Three other methods have been tried using *Mathematica* software. The first one is the rational interpolation method that approximates the Gaussian function by a rational polynomial. The user has the option to choose the order of the numerator, and the order of the denominator along with a set of points where the approximation has to be perfect. The results are illustrated in the Fig. 2.27, where a plot of the error is given.

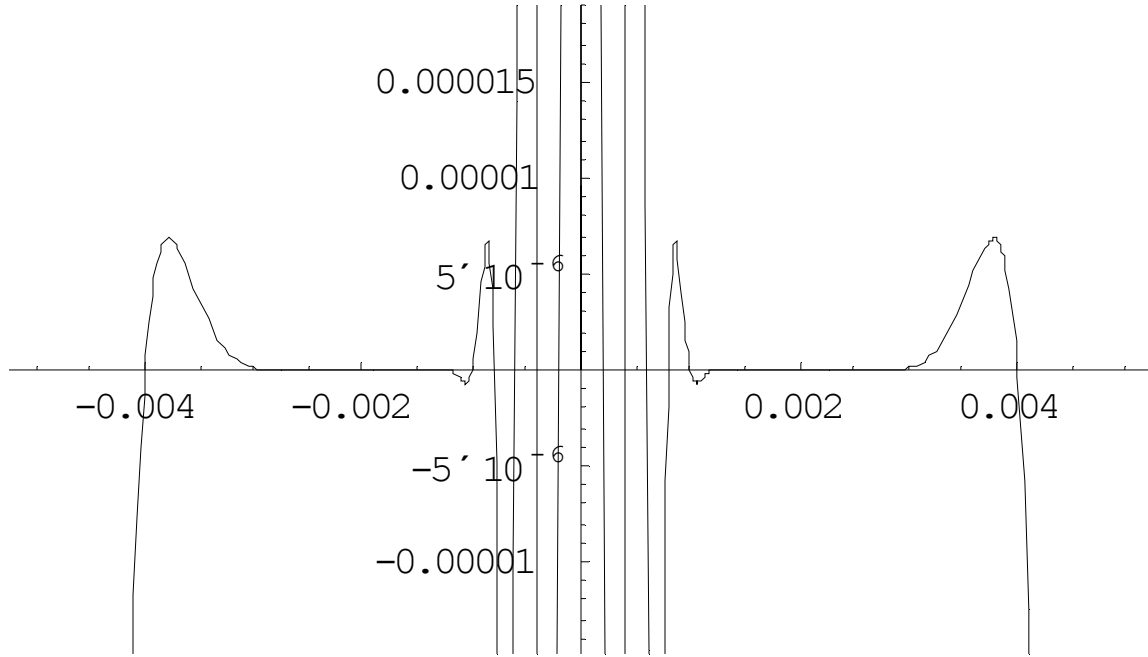


Figure 2.27. Error plot for the rational interpolation method

The figure above clearly demonstrates that this approximation cannot be used because the error becomes unacceptably large between the points selected by the user. Increasing the number of points will imply increasing the order of the polynomials used for the approximation, which is not convenient.

The second approximation used is Fourier trigonometric series expansion. This method implies approximation of the Gaussian intensity distribution function by a combination of cosine and sine functions. This method also does not work perfectly due to the fact that the approximation is good only in the vicinity of one point. The third method is the Min-Max approximation, that proved to be unacceptable for the same reasons.

B-Numerical model:

Another approach to modeling the quadrant detector is numerical solution of the energy integrals. This procedure has been implemented in MATLAB, and output voltages of the detector have been computed for various coordinates of the laser beam. The laser beam width w has been set to 0.4 mm, and the estimated peak intensity I_0 at the center of

the beam is 10. The plot of the generated data, representing response in the azimuth channel versus horizontal and vertical displacement X and Y is presented in Fig. 2.28. A plot of the elevation channel response is given in Fig. 2.29.

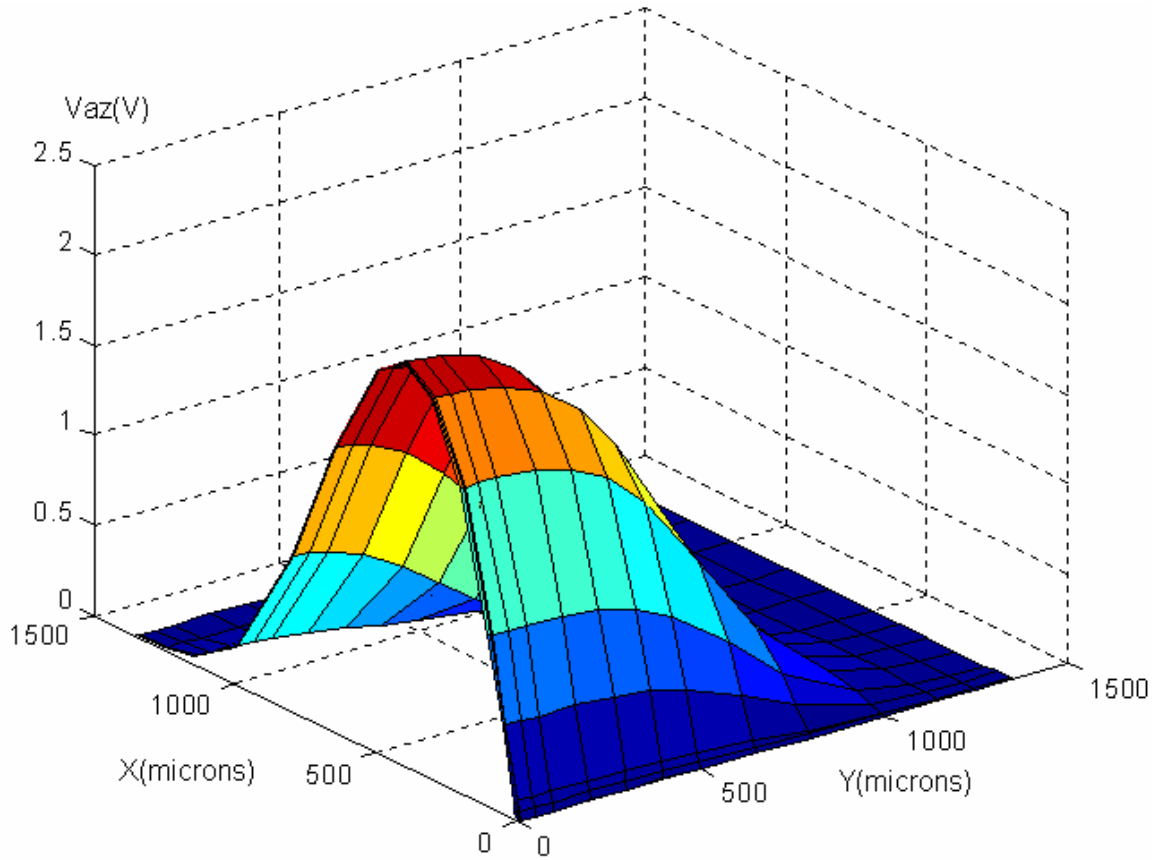


Figure 2.28. Azimuth Channel Response (Numerical Model)

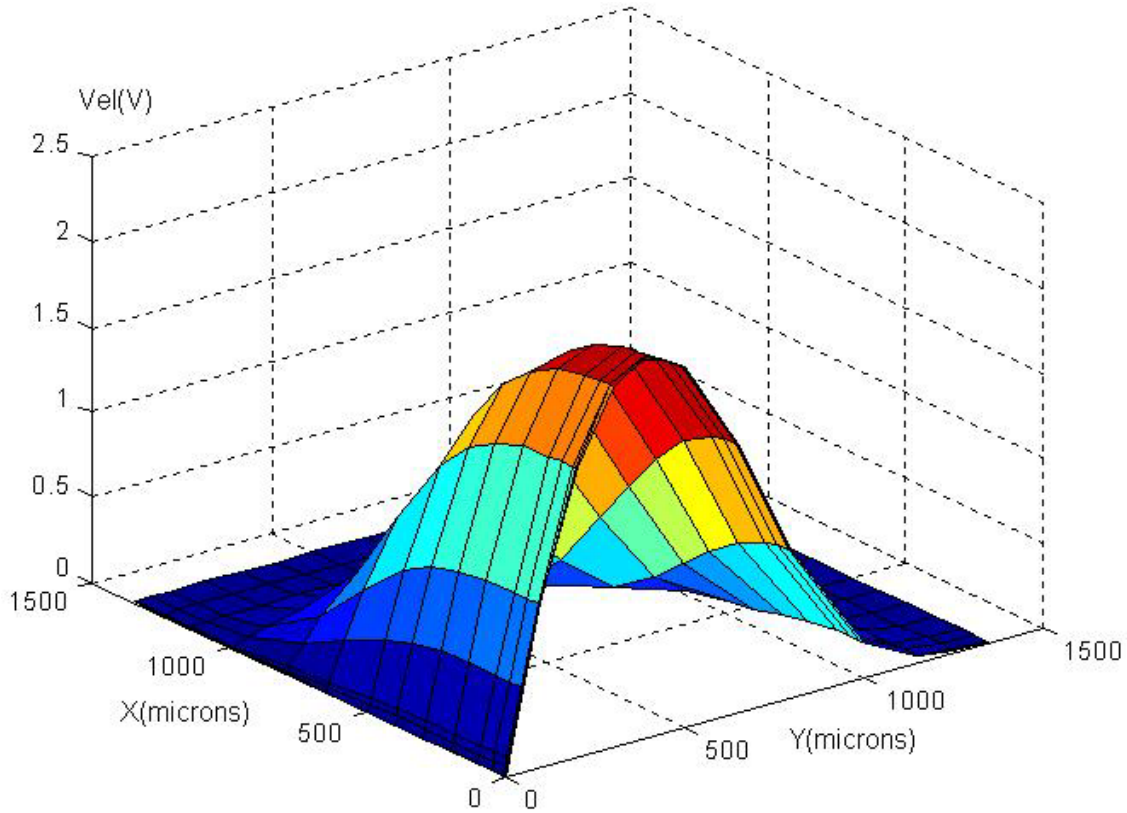


Figure 2.29. Elevation Channel Response (Numerical Model)

While the numerical model gives accurate results, as can be seen in Fig. 2.28 and Fig. 2.29, it is not very convenient for implementation in simulation software. Therefore, a good analytical approximation needs to be obtained. The approach that has been used relies on the concept of a Radial-Basis-Function (RBF) neural network. The idea behind this is to use a set of Gaussian basis function that all have the same input (azimuth and elevation displacement). Then a weighted sum of the basis functions is computed to form the output signal. The number of Gaussians is 31, and they have been placed according to the profile of the surface in Fig. 2.26. The width of each function is set to 250 microns. A set of measurement data points has been used to train the neural network (adjust the weights associated with each basis function). Then another set of measurement data has been used for model validation. The coefficient of determination is equal to 0.98. Fig. 2.30 presents the analytical approximation model after the training of the neural network.

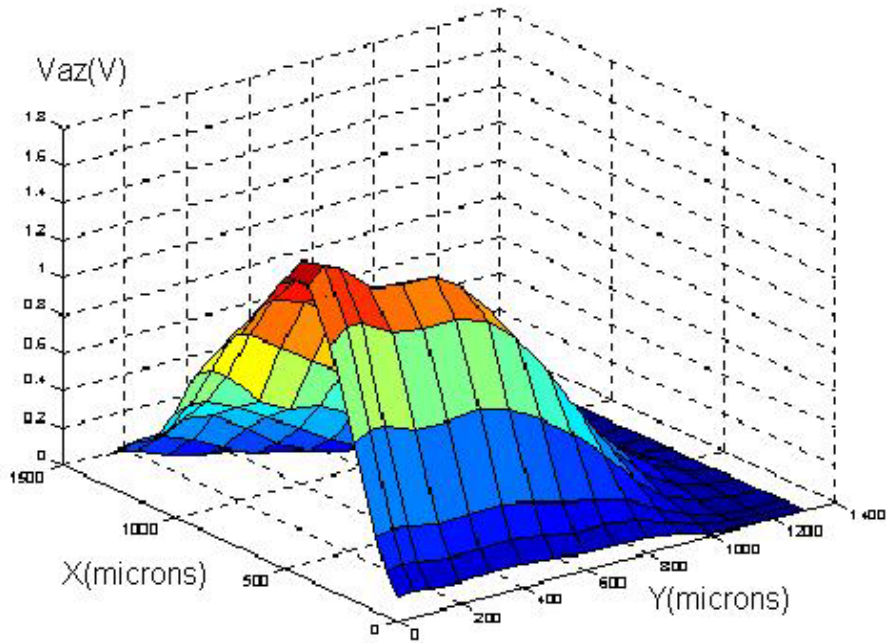


Figure 2.30. Azimuth Channel Response (Analytical Approximation)

Accuracy of the obtained approximation is illustrated in Fig. 2.31, where the error between the measurement data and the analytical approximation using an RBF network is presented.

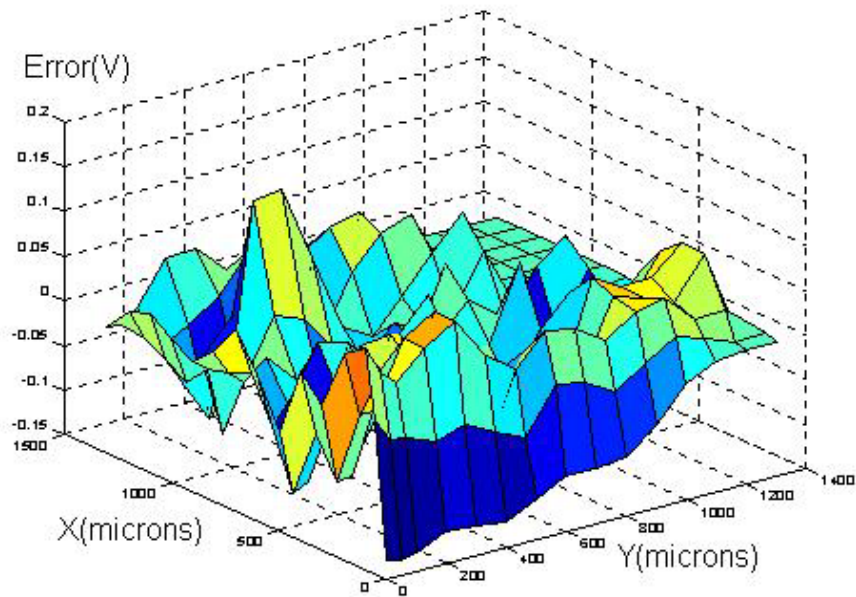


Figure 2.31. Analytical Approximation Error

2.3. Conclusion

This part of the project involves experimental characterization of the main components of the laser beam positioning system. It has resulted in obtaining the simulation models for the Bragg cell and the quadrant detector with all parameters being verified experimentally. These models can further be used as a testbed for implementing control systems for laser beam positioning. The results obtained in this task can also be used for design improvement of the particular components, for example, decreasing nonlinear effects of the quadrant detector.

REFERENCES

- [1] Internet, “Tip-Tilt Sensing and correction (Mirror)-TTS & TTM”,
<http://www.eso.org/~fdelplan/laos/node10.html>, (1999)
- [2] M. Elbaum, P. Diamant, M. King, W. Edelson, “Maximum Angular accuracy Of Pulsed Laser Radar In Photo Counting,” *Applied Optics*. 16(7), pp. 1982-92, (1977).
- [3] RCA Emitters and Detectors, “400 to 1100 nm Quadrant Silicon Avalanche Photodiode for tracking Applications”, *Technical characteristics of C30927E*, (1986).
- [4] T. E. Busch, “*Beam Steering Techniques for Free Space Laser Communication*,” Ph.D. Dissertation, Binghamton, New York, 1997.
- [5] S. J. Bennett, J. W. Gates, “ The design of detector arrays for laser alignment systems”, *Journal of Physics E: Scientific Instruments* Vol.3, pp. 65-68, (1970).

3. BRAGG CELL DESIGN CONSIDERATIONS

Depending on the desired communication link many parameters have to be determined to design the hardware components of laser communication systems. In this application the Bit Error Rate (BER) is considered to be a crucial issue to be addressed. This is the case especially when acousto-optic deflectors, such as Bragg cells, are used as steering devices. The transmitter beam diameter is one of the factors responsible for the BER. Indeed, depending on the link distance between the receiver and the transmitter, various beam diameters will yield different BER as shown in Fig. 3.1. It illustrates the fact that the BER can drastically change depending on the beam diameter under similar communication conditions.

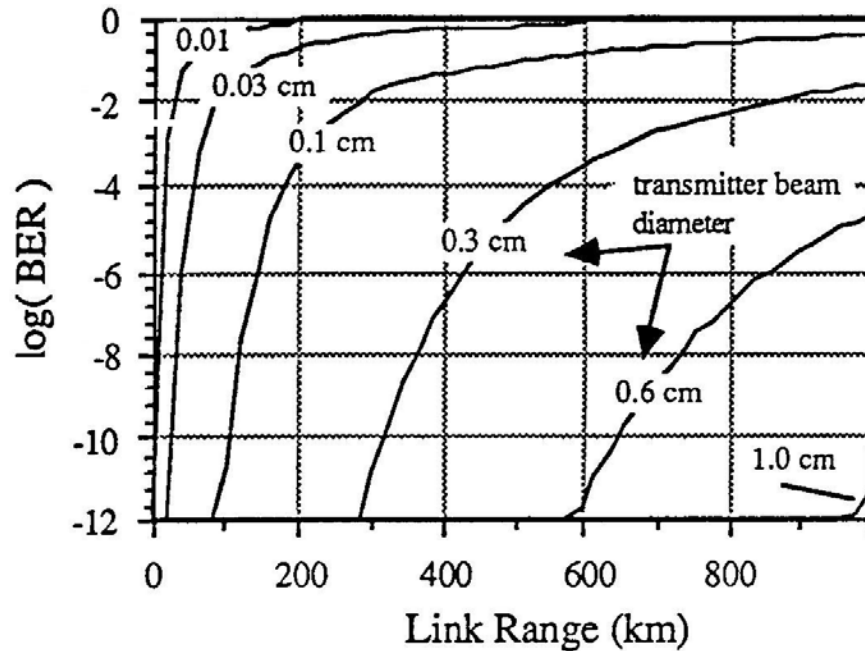


Figure 3.1. BER versus link range for different beam diameters [1]

The steering range allowed is also an important issue in acousto-optic based laser communication. As a matter of fact, the steering range known also as the field of regard

Θ_{FOR} is related to the beam diameter D_t , the wavelength of the laser λ , and the time bandwidth of the acousto-optic device N_{tb} (spot resolution) through [1]:

$$\Theta_{FOR} = \frac{\lambda * N_{tb}}{D_t} \quad (3.1)$$

As a result, depending on the desired spot resolution and the steering range, the wavelength of the laser to be used and the diameter of the beam can be determined.

3.1. Interaction Medium Choice

Regarding the material to be used as a medium for the Bragg cell, many parameters have to be considered. The most important ones are the acoustic velocity inside the medium, the coefficient of acoustic attenuation, and the figure of merit M_2 responsible for the diffraction efficiency.

Using the figure of merit M_2 , two other important figures of merit are defined. The thermal distortion figure of merit M_{th} defined as [1]:

$$M_{th} = \frac{n * M_2 * k}{\xi} \quad (3.2)$$

Where k - coefficient of thermal conductivity ($W / m / ^\circ C$).

ξ - dependence of acoustic velocity on temperature ($1 / ^\circ C$).

A high thermal figure of merit is desired. The higher is M_{th} , the less distortion of the beam wavefront is caused due to incomplete conversion of the electrical signal into acoustic waves inside the Bragg cell, and due to the acoustic attenuation inside the interaction medium [1].

An “optical deflection efficiency” figure of merit M_{de} defined as [1]:

$$M_{de} = \frac{M_2}{v * \Gamma^{1/2}}, \quad (3.3)$$

Where v - acoustic velocity inside the medium

Γ - acoustic attenuation parameter ($dB / m / GHz^2$).

This figure of merit represents the relation between M_2 and the acoustic attenuation parameter.

In the choice of the acousto-optic material to be used, one has to consider both a high thermal figure of merit M_{th} and deflection figure of merit M_{de} . Generally a trade-off has to be made to accommodate for both of the figures of merit choosing the material that offers the best combination. Fig. 3.2 shows a combination these two figures of merit in six different materials: GaP in both the longitudinal mode L110 and the shear mode S110, $LiNbO_3$ in the L100 mode, and TeO_2 in both the L001 and S110 mode.

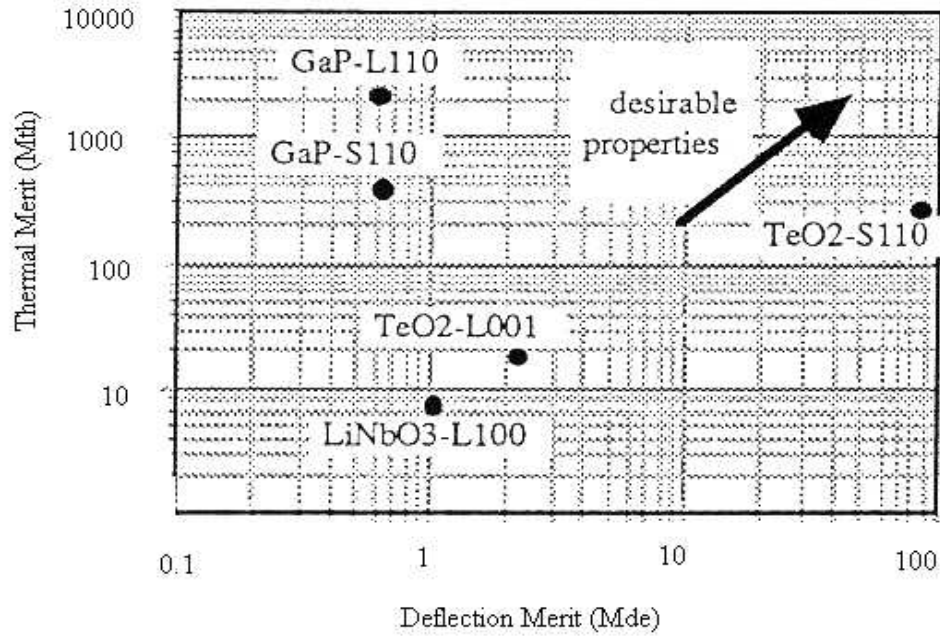


Figure 3.2. Thermal and Deflection figures of merit for different acousto-optic materials [1].

From Fig. 3.2, one can see that Tellurium Dioxide (TeO_2) in the slow shear mode is the material that offers the best combination among all the material compared. It offers a high figure of merit M_2 allowing high diffraction efficiency and requiring low drive power. Another important advantage is the ability of having a relatively large scanning

angle $\Delta\alpha$, thus offering the advantage of having more resolvable spots N [2]. However, the drawback of using Tellurium dioxide is its high acoustic attenuation Γ .

After a material has been chosen, more specific issues have to be addressed. The designer has to determine the desired spot resolution, the necessary beam width and the allowable bandwidth as well as the center frequency.

3.2. Choice Of Field Of Regard, Time Bandwidth And Beam Dimensions

The choice of spot resolution (time bandwidth) is important because the entire Bragg cell design is dependent on the chosen N_{tb} . Indeed, the higher is the spot resolution the higher is the design complexity. Moreover as shown in [1], and as illustrated in Fig. 3.3 [1], there is a trade-off between all three parameters: the field of regard, the beam size and the spot resolution.

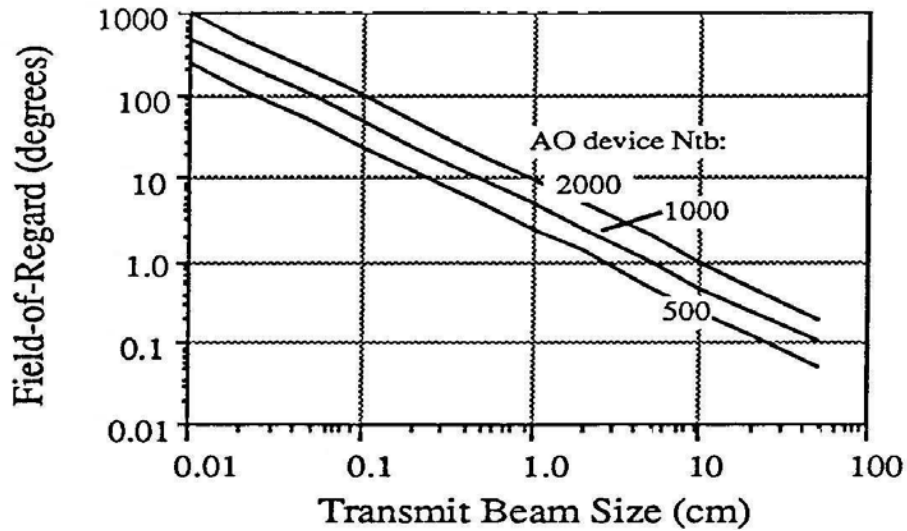


Figure 3.3. Field of regard Θ_{FOR} versus the beam size for different spot resolutions N_{tb}

On the other hand, the choice of the spot resolution N_{tb} has a direct effect on the maximum allowable operating frequencies of the Bragg cell (BW) due to acoustic attenuation through the relation [1]:

$$N_{tb} \approx \frac{10^{17}}{\nu * \Gamma * BW} \quad (3.4)$$

Finally, there is also an important relation between the time resolution N_{tb} , the bandwidth BW , and the optical beam width D_o [1]:

$$N_{tb} = \frac{D_o * BW}{\nu} \quad (3.5)$$

Using all the equations above, the design procedure for a chosen 500 spots Bragg cell in the horizontal channel versus a 200 spot Bragg cell in the vertical channel yields the following results:

1) Horizontal channel:

From equation (3.4), the allowable bandwidth in the horizontal channel is given by:

$$BW_H \approx \frac{10^{17}}{\nu * \Gamma * N_{tb}^H} \approx \frac{10^{17}}{617 * 22000 * 500} \approx 14.734 \text{ Mhz}$$

Using this result in equation (3.5) yields the necessary horizontal beam width:

$$D_0^H = \frac{N_{tb}^H * \nu}{BW_H} = \frac{500 * 617}{14,734,000} \approx 21 \text{ mm}$$

Note: By truncating the allowable bandwidth to 13 Mhz, the beam width can be made equal to 24 mm.

The transit time (T_{tr}) representing also the switching time at the horizontal channel can finally be computed as:

$$T_{tr}^h = \frac{D_0}{\nu} = \frac{24 * 10^{-3}}{617} = 38.89 \mu \text{ sec} \approx 40 \mu \text{ sec}$$

2) Vertical channel:

The maximum allowable bandwidth in this channel can be computed using equation (3.4):

$$BW_v^{\max} \approx \frac{10^{17}}{v * \Gamma * N_{tb}'} \approx \frac{10^{17}}{617 * 22000 * 200} \approx 36.83 \text{ Mhz}$$

However, considering the fact that the beam expansion ratio at the output of the laser cavity is 2:1 (horizontal: vertical), the beam vertical width is, thus, determined to be equal to 12 mm . So, using this beam width along with the chosen vertical spot resolution (200) in equation (3.5) yields the bandwidth of the vertical channel:

$$BW_v = \frac{N_{tb}^v * v}{D_o^v} = \frac{200 * 617}{12 * 10^{-3}} \approx 10.283 \text{ Mhz}$$

Finally, the transit time in this channel is computed by:

$$T_{tr}^v = \frac{D_o^v}{v} = \frac{12 * 10^{-3}}{617} = 19.44 \mu \text{ sec} \approx 20 \mu \text{ sec}$$

Note: Combining both the horizontal and vertical transit time gives a total response time of 40 μ sec in the system yielding a 25KHz tracking bandwidth.

3.3. Center Frequency Choice And Bragg Cell Design

Bragg cells are usually divided in two classes: isotropic and birefringent devices. The material presented in Chapter 1 concentrated on the working principle of isotropic devices for they are mostly used as deflectors. The dynamics involved in birefringent devices called also “abnormal deflectors” is more complicated. However, the use of birefringent cells offers the ability of having a larger acoustic bandwidth. This is due to the fact that for the same scanning angle defined earlier by $\alpha = \theta_i + \theta_d$, less acoustic divergence is needed [2]. This is illustrated in Fig. 3.4. One can see that in the isotropic case, due to the fact that $n_i = n_d$, both the diffracted and the incident beam vectors end on the same circle (see Fig. 4a). Considering the birefringence of the cell (Fig. 4b), the incident beam vector is longer than the diffracted vector. As a result, the angle $\Delta\theta_a$ needed to yield the same scanning angle $\Delta\alpha$ is smaller in the case of the birefringent cell.

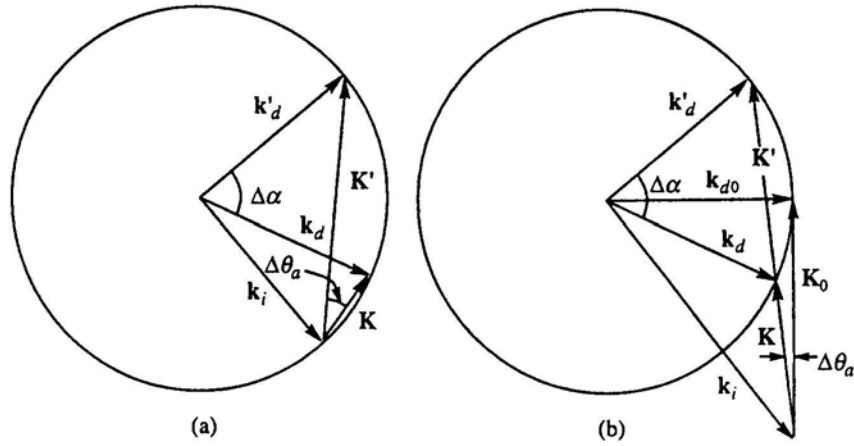


Figure 3.4. Vector diagrams for isotropic and birefringent cells

This means that the transducer length on the cell can be longer to achieve higher diffraction (see Chapter 1).

The material used as interaction media in the Bragg cells in our example is Tellurium Dioxide. It belongs to the class of birefringent crystals, however; the degree of birefringence caused by “optical activity” is considered to be very small for TeO_2 [2].

The birefringence is due to the fact the index of refraction n_i for the incident laser is not equal to the index of refraction of the output laser n_d . More precisely, the index n_i is usually bigger than the output laser index n_d . As a result, the input and output beam vectors are no longer equal and [2]:

$$\begin{aligned} k_i &= \frac{2 * \pi * n_i}{\lambda} \\ k_d &= \frac{2 * \pi * n_d}{\lambda} \end{aligned} \quad (3.6)$$

The inequality of both vectors yields the following momentum triangle for the birefringent interaction (see Fig. 3.5).

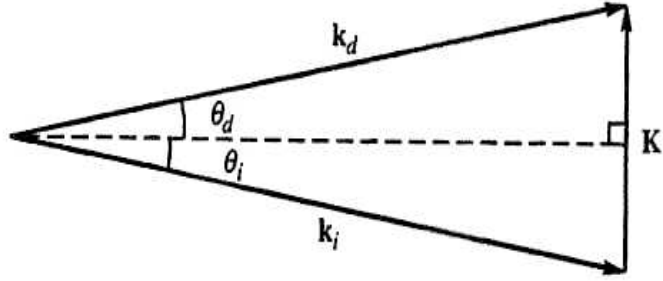


Figure 3.5. Birefringent momentum diagram

Using popular trigonometric relationships for the diagram in Fig. 3.5 we obtain

$$\begin{aligned} k_d^2 &= K^2 + k_i^2 - 2 * K * k_i * \sin(\theta_i) \\ k_i^2 &= K^2 + k_d^2 - 2 * K * k_d * \sin(\theta_d) \end{aligned} \quad (3.7)$$

Solution of (3.7) for $\sin \theta_i$ and $\sin \theta_d$ yields the Dixon equations [1]:

$$\begin{aligned} \sin \theta_i &= \frac{\lambda_o}{2 * n_i * v} * \left\{ f + \frac{v^2}{\lambda_o^2 * f} * (n_i^2 - n_d^2) \right\} \\ \sin \theta_d &= \frac{\lambda_o}{2 * n_d * v} * \left\{ f - \frac{v^2}{\lambda_o^2 * f} * (n_i^2 - n_d^2) \right\} \end{aligned} \quad (3.8)$$

Considering that the difference between n_i and n_d is small, (3.8) can be simplified to:

$$\begin{aligned} \sin \theta_i &= \frac{\lambda_o}{2 * n_i * v} * \{f\} \\ \sin \theta_d &= \frac{\lambda_o}{2 * n_d * v} * \{f\} \end{aligned} \quad (3.9)$$

Using the fact that for small x $\sin x = x$, the previous equations can be written as:

$$\begin{aligned}\theta_i &= \frac{\lambda_o f}{2 * n_i * v} \\ \theta_d &= \frac{\lambda_o f}{2 * n_d * v}\end{aligned}\tag{3.10}$$

Adding both the incident angle and the deflection angle yields the angle between the incident laser and the diffracted laser given by [2]:

$$\alpha = \theta_i + \theta_d = \frac{\lambda_o * f}{n_{eq} * v}\tag{3.11}$$

Where

$$n_{eq} = 2 * \frac{n_i * n_d}{n_i + n_d}\tag{3.12}$$

As a result, one can see that the relation linking the angle between the incident and diffracted beams to the input frequency still holds with the exception of the small change introduced by the difference in the refraction index as shown in (3.12). From equation (3.8), one can notice that if n_i is exactly equal to n_d , then we are in the isotropic case as has been described earlier. Using equation (3.8), the tangential or extreme value frequency is defined as the frequency at which the deflection angle is zero whereas the incident angle reaches a maximum [2]:

$$f_o = \frac{v}{\lambda_o} [n_i^2 - n_d^2]^{\frac{1}{2}}\tag{3.13}$$

The choice of center frequency for the Bragg cells is a challenging task in birefringent cells. This is due to the fact that the center frequency should accommodate for the required bandwidth without reaching the degenerate frequency of the cell as will be seen later.

There are several methods that can be used to compute the center frequency, and two main design solutions to be considered. There is the Non-Rotated method and the Rotated method. In the non-rotated method, the cell is designed so that it is not optically rotated, but is acoustically rotated. This means that in the case of non-rotated cells (also known as off-axis cells), the sound wave vector is no longer parallel to the $[110]$ plane but is rather rotated by an angle θ_a as illustrated in Fig. 3.6. In the rotated cell, the Bragg cell is optically rotated, which means that the acousto optic interaction does now occur in a rotated plane rather than in the conventional z-plane.

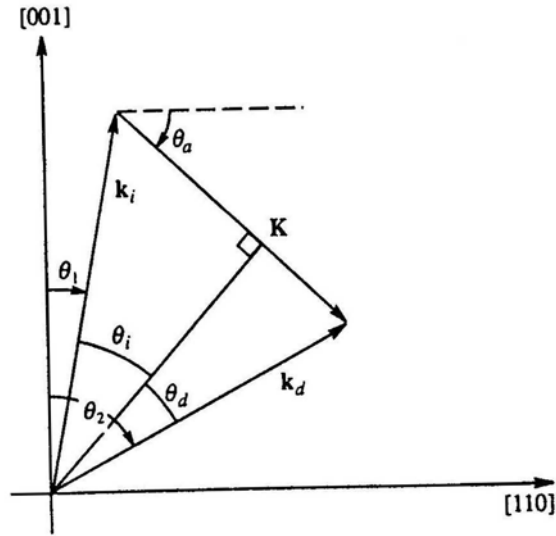


Figure 3.6. Off-axis illustration for non-rotated Bragg cell[2]

From the previous figure, we have

$$\begin{aligned}\theta_i &= \pm(\theta_a - \theta_1) \\ \theta_d &= \pm(\theta_2 - \theta_a)\end{aligned}\tag{3.14}$$

The Dixon equation (3.8) can be rewritten taking in consideration the angles θ_a , θ_1 , and θ_2 :

$$\begin{aligned}\sin \theta_i &= \frac{\lambda_o}{2 * n_i(\theta_1) * v(\theta_a)} * \left\{ f + \frac{v^2(\theta_a)}{\lambda_o^2 * f} * \{n_i^2(\theta_1) - n_d^2(\theta_2)\} \right\} \\ \sin \theta_d &= \frac{\lambda_o}{2 * n_d(\theta_2) * v(\theta_a)} * \left\{ f - \frac{v^2(\theta_a)}{\lambda_o^2 * f} * \{n_i^2(\theta_1) - n_d^2(\theta_2)\} \right\}\end{aligned}\quad (3.15)$$

Design of the non-rotated Bragg cells consists of defining the relations between the angles $\theta_a, \theta_1, \theta_2$ and the operating frequency f . However, since we have two equations and three variables, there are two ways of solving for the angles.

a- First solution method:

The “first solution method” implies fixing the angle θ_a , and then solving for θ_1 and θ_2 with respect to f . After solving for these two angles, the degenerate frequency is determined, and the center frequency is chosen.

The relations between the angles and the frequency are solved for both the cases where the sign is positive and negative in (3.14). The solution has been conducted in [2], where $\theta_a = 6^\circ$, and $\lambda_o = 632.8nm$. Fig. 3.7 illustrates the results found.

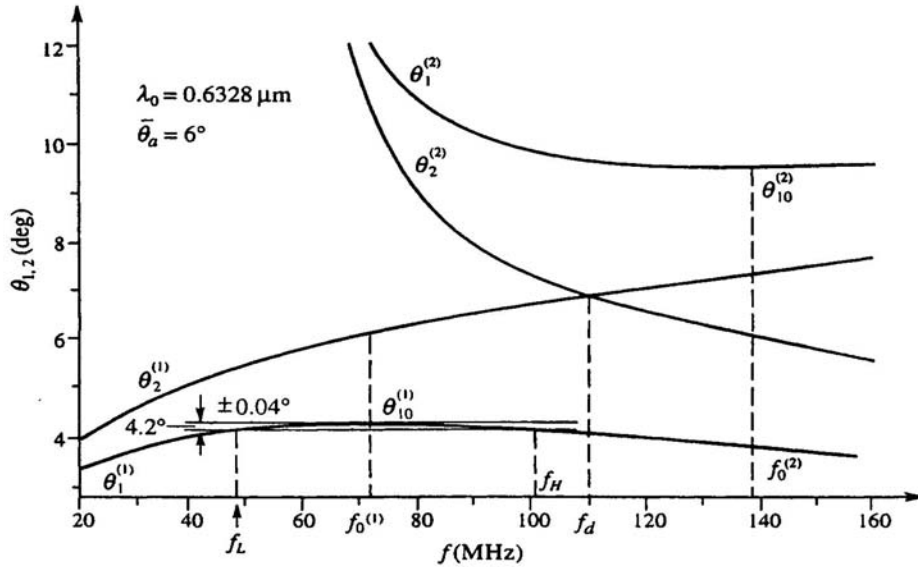


Figure 3.7. First solution method for off axis device with $\lambda = 632.8nm$ and $\bar{\theta}_a = 6^\circ$

At first, we should note that we $f_o^{(1,2)}$ are defined as the tangential or extreme frequencies. At these frequencies, the deflection angle is zero, and the angles $\theta_1^{(1,2)}$ reach their maximum value. One also should note that the degenerate frequency is given at the intersection of the curves $\theta_2^{(1)}(f)$ and $\theta_2^{(2)}(f)$, it is denoted f_d . It is the frequency at which the incident laser vector k_i is diffracted twice. It is diffracted as k_d and redirected as k_i' . This is illustrated in Fig. 3.8 for on-axis devices where the sound vector is K_d , at the degenerate frequency f_d .

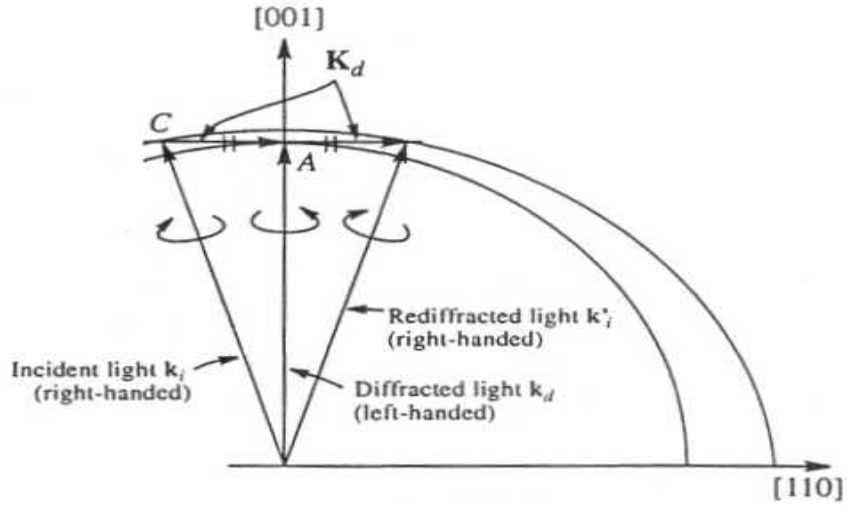


Figure 3.8. Illustration of the rediffraction at the degenerate frequency f_d for on-axis Bragg cells

The same phenomenon is illustrated in Fig. 3.9 for off-axis devices where the sound wave propagation direction has been rotated by an angle θ_a .

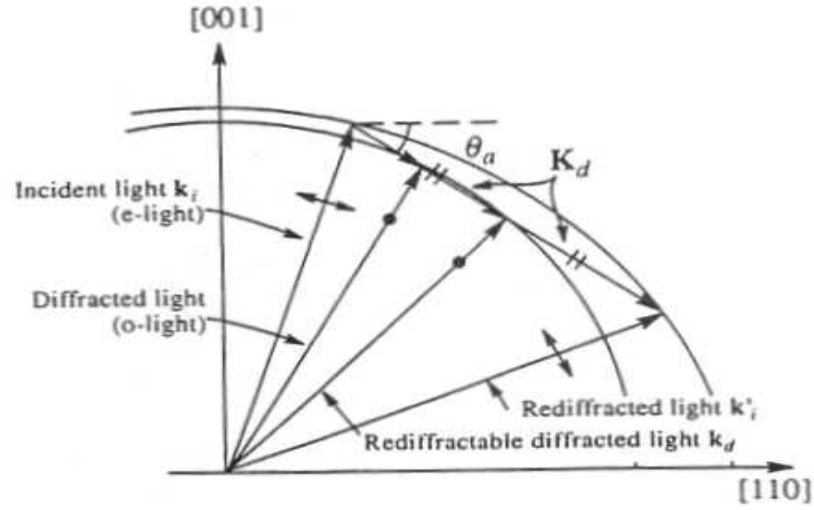


Figure 3.9. Illustration of the rediffraction at the degenerate frequency f_d for off-axis Bragg cells

Note: To avoid the degeneracy, the center frequency is chosen so that the bandwidth does not include the frequency f_d .

b- Second solution method:

The second solution method is based on the fact that this time the fixed angle is θ_1 , and a relation between θ_a , θ_2 and f is found. This solution is generally preferred over the “first solution method” because it gives details on the actual design of the Bragg cell. The idea here is to set the angle θ_1 slightly smaller than θ_{10} (the two angles are negative), and solve for the relation $\theta_a - f$ for different values of θ_1 . The highest frequency of the operating bandwidth should also be kept less than the degenerate frequency f_d . The following figure adopted from [2] represents three solutions for $\theta_a - f$ for three values of $\theta_1 = 5.67^\circ, 5.69^\circ$ and 5.71° . It also represents the relation between the angle θ_2 and the frequency f illustrating a linear relation between the deflection angle and the operating frequency at $\theta_1 = 5.69^\circ$ given that:

$$\theta_d = \pm(\theta_2 - \theta_a) \quad (3.16)$$

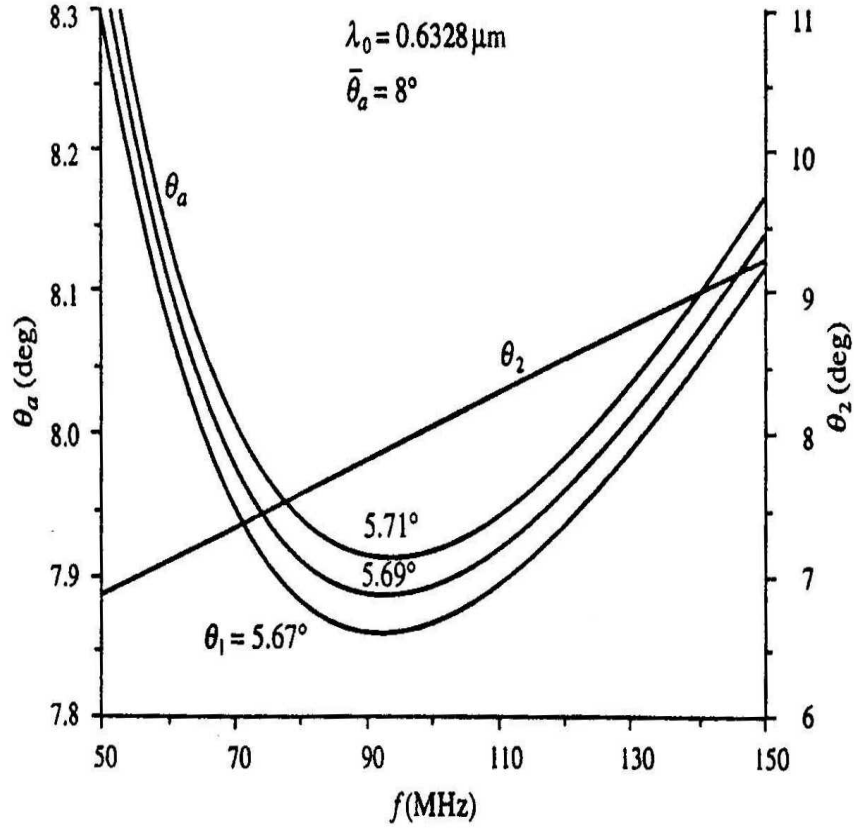


Figure 3.10. The second solution method applied to the off axis Bragg cell design with $\lambda_o = 632.8nm$ and an 8° off axis angle as per[2].

Using the following table [2], representing three solutions to the design problem using the “second solution method”, we can see that as the value θ_1 decreases the bandwidth increases going from 76 to 97 MHz. However the highest frequency in the range increases from 138 to 153 MHz exceeding the degenerate frequency of 148 MHz that can be found using the first solution method [2]. Thus, taking θ_1 equal to 5.69° seems to be the right choice in this case offering a bandwidth equal to 87 MHz and an acoustic divergence angle given by $2 * \delta\theta_{a0} = 2 * 0.115^\circ = 0.23^\circ$ and $f_o = 94MHz$ as can be found using the first solution method.

Table 3.1. Second solution characteristic parameter definition

$\bar{\theta}_a(\text{deg})$	$\theta_1(\text{deg})$	$\delta\theta_{a0}(\text{deg})$	$f_L(\text{MHz})$	$f_H(\text{MHz})$	$\Delta f(\text{MHz})$
8	5.71	0.088	62	138	76
8	5.69	0.115	59	146	87
8	5.67	0.141	56	153	97

As stated earlier, using the second solution method is more advantageous in the sense that it gives direct information on the Bragg cell design itself. Indeed, the transducer length, also called interaction length of the cell can now be determined. The interaction length of the cell is given by the following equation:

$$L = R * \frac{\Lambda_o}{\delta\theta_{a0}} \quad (3.17)$$

Where:

$$\Lambda_o = \frac{v}{f_o} \quad (3.18)$$

So L is given by:

$$L = R * \frac{v}{f_o * \delta\theta_a^o} \quad (3.19)$$

Where R depends on the allowable passband nonuniformity. The allowable passband nonuniformity is 3dB, but in the case of two-dimensional steering system, it is taken as 1.5 dB for each one of the two cells [2]. Table 3.2 gives the values of R depending on the allowable nonuniformity. The value of v , the velocity of the acoustic wave is dependent on the off axis angle chose. It is given by [2]:

$$v^2(\theta_a) = v_t^2 \cos^2(\theta_a) + v_z^2 \sin^2(\theta_a) \quad (3.20)$$

Where

$$\begin{aligned} v_t &= 616 \mu\text{m} / \mu\text{s} \\ v_z &= 2104 \mu\text{m} / \mu\text{s} \end{aligned}$$

Different values of v corresponding to different angles θ_a have been computed in [2], and the results are presented in Table 3.3.

Table 3.2. Value of R versus allowable uniformities

Allowable non-uniformity (dB)	Value of R
1	0.25
1.5	0.32
2	0.37
3	0.45

Table 3.3. Velocity v versus off axis angle θ_a

$\theta_a (Deg)$	$v(\theta)$ in $\mu m / \mu s$
0	616
1	617
2	620
3	625
5	640
6	651
7	663
8	677
9	692
10	708

As an illustration, considering an allowable nonuniformity of 3dB, and a velocity $v = 677 \mu m / \mu s$ with an off axis angle of 8 degrees, and using (3.18), we get:

$$L = 0.45 * \frac{677}{94000000 * (0.115 * \pi / 180)} = 1.612 mm$$

In the case of the Bragg cell used in our laboratory, acoustical rotation is done to accommodate for both the desired center frequency, and the desired bandwidth. The acoustic rotation of each cell is 2° [1]. In order to attenuate any reflection of the

propagating wave once it reaches the top of the cell, an appropriate absorbing material is used to coat the top surface.

The center frequency has been chosen to be 24 MHz for both cells. As a result, the frequency range for the horizontal cell is from 17 MHz to 31 MHz, for the vertical cell - from 18 MHz to 30 MHz. The choice of the same center frequency for both cells facilitates the frequency generation by the driver electronics. The Driver electronics uses a Direct-Digital-Synthesis (DDS) card to produce the desired frequencies. These are first digitally generated then converted to analog signals through a “Stanford Telecom 2272A DDS board.”

The DDS card has a frequency clock of 160 MHz, and offers a 610 Hz resolution. The DDS clock higher than the tracking frequency of the cell, application of TDMF (Time Division multiplexing of frequencies) could offer multiple beam generation at the same time [1]. The whole system is PC controlled, including the laser and camera switching ON/OFF.

3.4. Design And Materials Alternatives

1- Rotated cells

Another design procedure consists of designing cells that are optically rotated. Using optically rotated cells offers many advantages of which the main ones are the fact that the acoustic bandwidth can be increased without a loss of deflection efficiency as can be observed in the off-axis non-rotated cells. Indeed, in non-rotated off-axis cells, the larger is the off-axis angle, the higher is the velocity of the acoustic wave. As a result, the figure of merit M_2 defined for birefringent cells as follows becomes smaller as the velocity increases causing the deflection efficiency to decrease.

$$M_2 = \frac{n_i^3 n_d^3 p^2}{\rho V^3}$$

Fig. 3.11 adopted from [2] illustrates the AO interaction plane, as a rotation by α is achieved around the [110] axis:

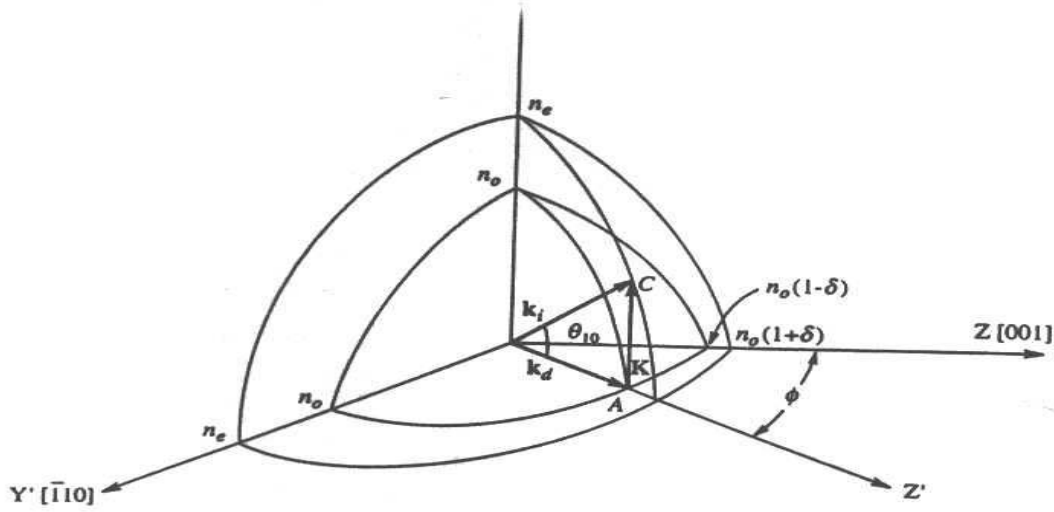


Figure 3.11. Rotated acousto-optic interaction plane

In rotated cells, we also distinguish between on-axis devices and off-axis devices. Although the whole derivation of the design process is not given, the main procedures, equations and discussions are described below.

First the Dixon equations as presented in (3.15) can be rewritten as:

$$\begin{aligned} \sin \theta_i &= \frac{\lambda_o}{2 * n_i(\phi, \theta_1) * v(\phi, \theta_a)} * \left\{ f + \frac{v^2(\phi, \theta_a)}{\lambda_o^2 * f} * \{n_i^2(\phi, \theta_1) - n_d^2(\phi, \theta_2)\} \right\} \\ \sin \theta_d &= \frac{\lambda_o}{2 * n_d(\phi, \theta_2) * v(\phi, \theta_a)} * \left\{ f - \frac{v^2(\theta_a)}{\lambda_o^2 * f} * \{n_i^2(\phi, \theta_1) - n_d^2(\phi, \theta_2)\} \right\} \end{aligned} \quad (3.22)$$

One of the main difficulties solving the Dixon equations for the case of rotated cells is to determine the $v(\phi, \theta_a)$ depending on the rotation angle ϕ and the off-axis angle θ_a . Solving for the exact value of v can be tedious and is analytically complex. However, as presented in [2], the equation given in (3.20) could be used as a good approximation in the case where the value of the pair (ϕ, θ_a) is below the curve in Fig. 3.12. For some other pairs not present under the curve, Table 3.4 presents the accurate velocity value to be used.

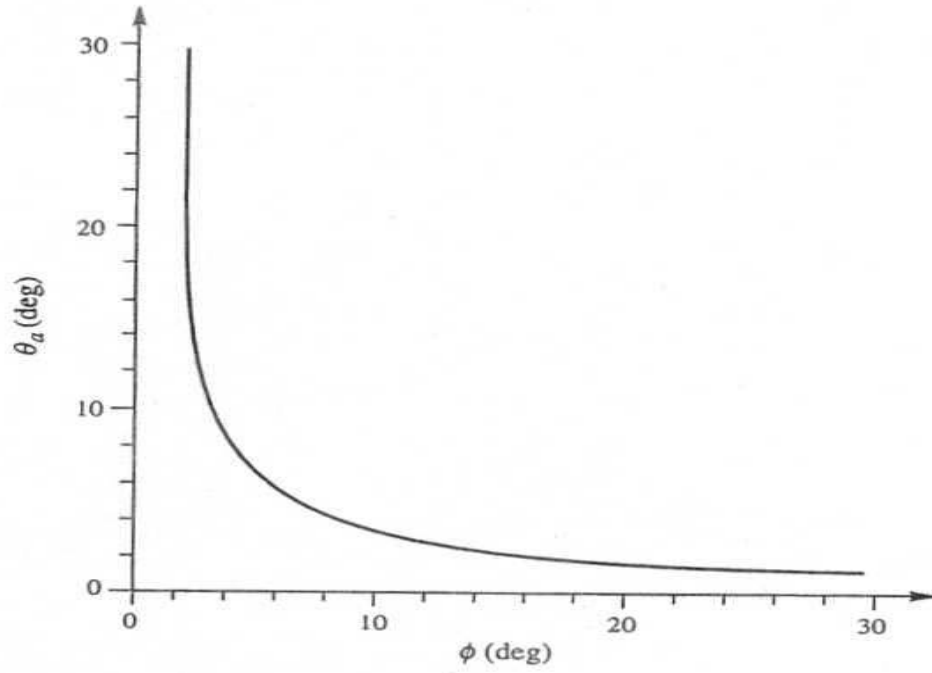


Figure 3.12. Region (under the curve) where (3.20) could be used with less than 1 percent approximation error

Table 3.4. Velocity values for pairs where the approximation is not to be used

(ϕ, θ_a) in $^\circ$	$v(\phi, \theta_a)$ in (m / s)
(8,8)	674
(10,10)	750

The two cases: on-axis and off-axis designs are now considered.

a - On-axis rotated cell:

In the case of On-axis rotated cells, in order to find the degenerate frequency f_d , as well as the maximum value θ_{10} , the following equations are used (these are also valid for on-axis non rotated cells)[2]:

$$f_o = \frac{v}{\lambda_0} [n_c^2 - n_A^2]^{1/2}$$

$$\cos(\theta_{10}) = \frac{n_A}{n_c}$$
(3.23)

Where

$$n_A = \frac{n_o(1-\delta)}{[\cos^2 \phi + (1-\delta)^2 \sin^2 \phi]^{1/2}}$$

$$n_c = n_e^2 + [1 - \frac{n_e}{n_o^2(1+\delta)^2}] * n_A^2 * \cos^2 \phi$$
(3.24)

The value of δ depends on the optical properties of the material. It is given by:

$$\delta = \frac{\lambda_o * \rho}{2 * \pi * n_o}$$
(3.25)

Where λ_o - wavelength of the laser in μm

ρ - constant dependent on the operating laser wavelength as well as on the material properties. It is expressed in $rad / \mu m$.

n_o - ordinary index of refraction of the cell at a given frequency.

Using (3.25) in (3.24) and solving (3.23) yields both the degenerate frequency and the maximum angle value θ_{10} . Then using the second solution method, using different values around θ_{10} , one can solve for $\theta_a - f$, and find the acoustic divergence angle $\delta\theta_{ao}$ necessary to have the desired bandwidth. Finally using (3.17), the interaction length L can be determined.

Fig. 3.12 illustrates the transducer position on a rotated Tellurium dioxide Bragg cell.

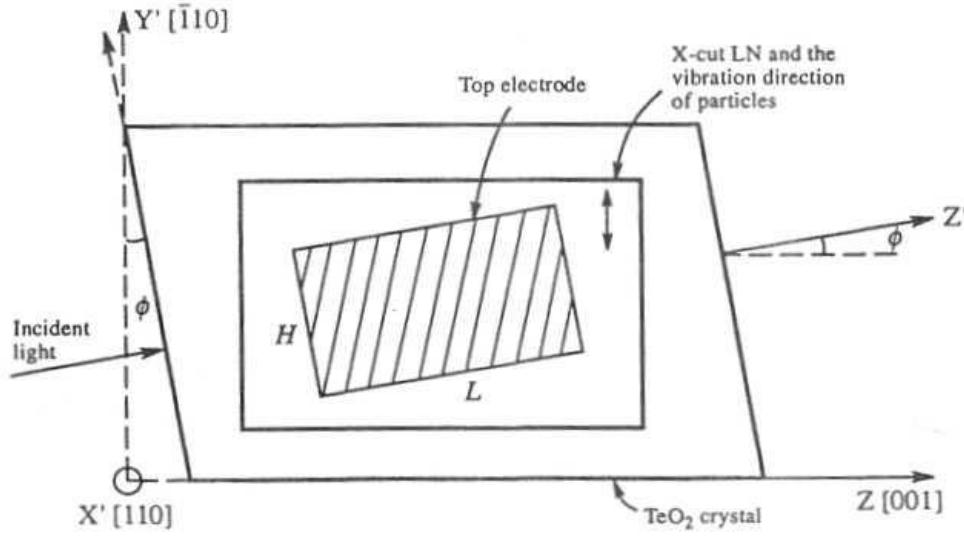


Figure 3.13. Transducer position on a rotated cell

b- Rotated off-axis cells:

The difference in designing off-axis cells is mainly in the determination of the value of the velocity $v(\phi, \theta_a)$. As explained earlier, for the region under the curve in Fig. 3.12, the approximation in (3.20) can be used; otherwise, a more tedious derivation (Solution of the eigenvalue characteristic equation...) should be used to find the accurate v . Table 3.4 gives the computed velocity [2] for two pairs outside the area where the approximation can be used.

After v has been found, the first solution method and then the second solution method can be used to obtain $f_o, f_H, f_L, \Delta f$ and the acoustic divergence angle $\delta\theta_{ao}$, before computing the interaction length L .

2- Material choice:

Tellurium dioxide has been shown to offer the main desirable properties with the drawback of having a high acoustic attenuation. For a lower acoustic attenuation, a relatively new material “mercurous chloride” Hg_2Cl_2 could be used instead of tellurium

dioxide TeO_2 . It offers a high figure of merit $M_2 = 1060 * 10^{-15} * s^3 / Kg$ and slow shear mode with a velocity of $347 m/s$, as well as a coefficient of acoustic attenuation of $13.7 dB / \mu s * GHz^2$. Other interesting figures for the mercurous chloride are [2]:

Transmission range: $0.38 - 25 \mu m$

$n_o = 1.962$

$n_e = 2.621$

Note: the transmission range of tellurium dioxide is only from 0.35 to $5.0 \mu m$.

3.5. Application Of Genetic Algorithms For Design Optimization Of A Bragg Cell

Mathematical model of a Bragg cell, reflecting the physical phenomena behind its operation, provides a description of the complex interrelation between various parameters of the device and characteristics of its performance. Such a model has a number of applications including accurate assessment of the system's performance, analysis of sensitivity of particular performance characteristics to design parameters, and providing a simulation testbed for the analysis of the entire beam steerer. Moreover, the model presents a basis for the formalization of the optimal design problem of a Bragg cell, providing mathematical formulation for particular constraints and optimization criteria. Indeed, the design problem could be defined as the following nonlinear constrained optimization problem

$$\text{Min } C(X) / [X_1 \leq X \leq X_2, A \leq W(X) \leq B]$$

Where X – a vector of design parameters that customarily are chosen by the device

designer in order to assure certain performance characteristics of the design,

$X_1 \leq X \leq X_2$ – a set of conditions limiting numerical values of the design parameters reflecting the feasibility considerations,

$W(X)$ – is a vector-function representing operational characteristics of the device as functions of design parameters,

$A \leq W(X) \leq B$ – is a set of conditions presenting design specifications in terms of common figures of merit, and

$C(X)$ – is one of the operational characteristics of the device (or a linear combination of several operational characteristics taken with appropriate weights) designated as the design criterion.

One can realize that expressions $W(X)$ and $C(X)$ reflect laws of physics, and in combination constitute the mathematical model of the device. Any set of particular numerical values of the vector of design parameters, $X=X^*$, constitutes a solution of the design problem. Any set of particular numerical values of the vector of design parameters, $X=X^{**}$, that satisfies the feasibility conditions and the design specifications, i.e. $X_1 \leq X^{**} \leq X_2$, $A \leq P(X^{**}) \leq B$, constitutes an acceptable solution of the design problem. The criterion provides a numerical measure of goodness to each acceptable solution of the design problem, facilitating the selection of the optimal solution, $X=X_{OPT}$. While any designer is intended to obtain a design solution as close to the optimal solution as possible, the “goodness” of the design is based upon his/her experience and intuition and truly optimal designs still is just a matter of good intentions.

There are two major factors preventing us from finding the optimal solution of a design problem. The first one is the complexity of solving a nonlinear constrained optimization problem. The second factor is that, typically, a nonlinear optimization problem has many “local” optimal solutions among those the global minimum should be found. The first difficulty we address by converting the original constrained optimization problem into an unconstrained optimization problem via the method of penalty functions as follows

$$\text{Min } L(X)$$

where $L(X)=C(X)+P_1(X)+P_2(X)$ – is a loss function,

$P_1(X)$ and $P_2(X)$ – are penalty function defined as follows,

$$\text{If } [X_1 \leq X \leq X_2] \ P_1(X)=0$$

$$\text{If } [X_1 > X] \ P_1(X) = (X_1 - X)^T Q (X_1 - X)$$

$$\text{If } [X > X_2] \ P_1(X) = (X - X_2)^T Q (X - X_2)$$

and

$$\text{If } [A \leq W(X) \leq B] \ P_2(X)=0$$

$$\text{If } [A > W(X)] \ P_2(X) = [A - W(X)]^T R [A - W(X)]$$

$$\text{If } [W(X) > B] \ P_2(X) = [W(X) - B]^T R [W(X) - B],$$

T - is a transpose symbol, and $Q \gg 1$ and $R \gg 1$ are weight coefficients.

One can realize that any successful minimization effort would result in the “enforcing” the constraints on the vector of design parameters X .

Proliferation of genetic optimization algorithms, possessing the advantages of known random and direct search optimization procedures, combined with the availability of high performance computers alleviated the second obstacle in the way of the formal solution of design optimization problems. The following diagram illustrates application of a genetic algorithm to the solution of a design optimization problem.

GENETIC OPTIMIZATION FOR OPTIMAL DESIGN

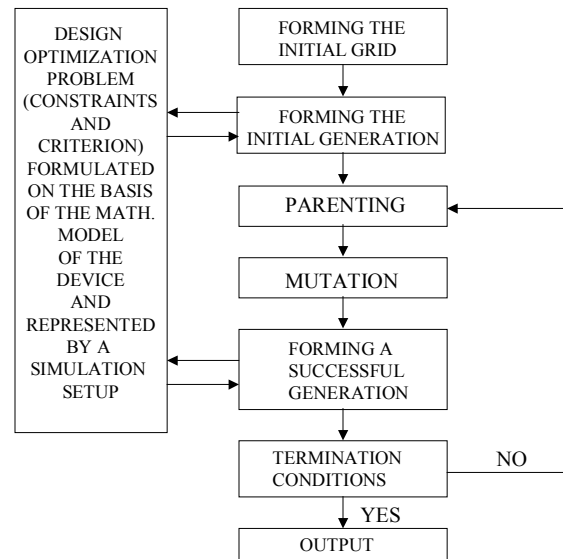


Figure 3.14 Genetic Optimization of Optimal Design

Mathematical model developed for the Bragg cell can be used at the design stage for selecting physical parameters of this system component. The objective is to improve performance while satisfying some constraints posed by the design specifications. This calls for running a constrained optimization procedure. Out of a number of approaches to minimizing (maximizing) a performance criterion we have selected a genetic algorithm procedure. Definition of the problem is as follows. We will run optimization for an acoustically rotated off-axis Bragg cell. The parameters to be selected by the routine are:

Θ_a – off-axis angle, rad;
 L – transducer length, m;
 H – transducer height, m;
 P_a – acoustic power, W;
 Θ_i – incidence angle, rad.

The following set of equations describes behavior of the acousto-optic device. The acoustic velocity can be expressed as follows.

$$v^2 = v_t^2 \cos^2 \Theta_a + v_z^2 \sin^2 \Theta_a$$

For TeO₂ $v_t=616$ m/sec, $v_z=2104$ m/sec [1], therefore

$$v = \sqrt{616^2 \cos^2 \Theta_a + 2104^2 \sin^2 \Theta_a} \quad (3.26)$$

The deflection figure of merit

$$M_2 = \frac{n_i^3 n_d^3 P^2}{\rho v^3}$$

From [2] we have $n_t=2.26354$, $n_d=2.25658$, $p=0.1126$, $\rho=5990$ kg/m³; therefore,

$$M_2 = \frac{2.82 * 10^{-4}}{v^3} \quad (3.27)$$

The incidence angle corresponding to the Bragg condition can be found as

$$\Theta_i = \frac{\lambda f_c}{2n_i v}$$

Hence the center frequency f_c

$$f_c = \frac{2n_i v \Theta_i}{\lambda} = 6.757 * 10^6 v \Theta_i \quad (3.28)$$

As has been mentioned previously, in the case of an off-axis cell design the entire acoustic frequency range should be below the degenerate frequency f_d . Fig. 3.7 illustrates a graphical approach to finding f_d . Values of the degenerate frequency have been tabulated in [2] for different values of the off-axis angle Θ_a . For practical purposes we

have generated an analytical expression for $f_d(\Theta_a)$ for a given value of the optical wavelength using the Least Square Method approach as follows:

$$f_d = 0.9161 * 10^6 \Theta_a^2 + 6.3461 * 10^6 \Theta_a + 39 * 10^6$$

We select the maximum operating frequency to be 2 MHz below the degenerate frequency, therefore

$$f_{\max} = 0.9161 * 10^6 \Theta_a^2 + 6.3461 * 10^6 \Theta_a + 37 * 10^6$$

Acoustic bandwidth can be found as

$$\Delta f = 2(f_{\max} - f_c) \quad (3.29)$$

Steering range

$$\Delta \Theta = \frac{\lambda \Delta f}{nv} = 2.96 * 10^{-7} \frac{\Delta f}{v} \quad (3.30)$$

From [2] the maximum deflection angle is

$$\Theta_d = \frac{\lambda}{2n_d v} f_c - \frac{v}{2n_d \lambda f_c} [n_i^2 - n_d^2] + \frac{\Delta \Theta}{2} = \frac{1.485 * 10^{-7}}{v} f_c - \frac{10404v}{f_c} + \frac{\Delta \Theta}{2} \quad (3.31)$$

Finally, diffraction efficiency is found as

$$\eta = \sin^2 \left\{ \frac{\pi}{\lambda \cos \Theta} \sqrt{\frac{M_2 L}{2H} P_a} \right\} = \sin^2 \left\{ \frac{\pi}{\lambda \sqrt{\cos \Theta_i \cos \Theta_d}} \sqrt{\frac{M_2 L}{2H} P_a} \right\}$$

$$\eta = \sin^2 \left\{ 4.69 * 10^6 \sqrt{\frac{M_2 L}{2H \cos \Theta_i \cos \Theta_d} P_a} \right\} \quad (3.32)$$

The Klein-Cook parameter

$$Q = \frac{2\pi \lambda L}{\Lambda^2 \cos \Theta} = \frac{2\pi \lambda L f_{\max}^2}{v^2 \sqrt{\cos \Theta_i \cos \Theta_d}} = 4.2 * 10^{-6} \frac{L f_{\max}^2}{v^2 \sqrt{\cos \Theta_i \cos \Theta_d}} \quad (3.33)$$

Following is a list of physical constraints imposed by the design specifications:

$$0 \leq \Theta_a \leq 0.175 \text{ rad } (10^0)$$

$$0.01 \text{ m} \leq L \leq 0.1 \text{ m}$$

$$0.005 \text{ m} \leq H \leq 0.1 \text{ m}$$

$$0 \leq P_a \leq 1 \text{ W}$$

$$0 \leq \Theta_1 \leq 0.175 \text{ rad } (10^0)$$

$$M_2 \geq 10^{-12}$$

$$0.8 \leq \eta \leq 1$$

$$\Delta\Theta \geq 0.0175 \text{ rad } (1^0)$$

Optimization using the genetic algorithm and mathematical model of the Bragg cell described by (3.26) – (3.33) has been performed twice. In the first case we maximize the steering range $\Delta\Theta$, in the second – efficiency η . The results are presented in Table 3.5.

Table 3.5. Genetic optimization for off- axis acoustically rotated device

		$\eta \rightarrow \max$	$\Delta\Theta \rightarrow \max$
Variables of optimization	Off-axis angle Θ_a , rad (X_1)	0.107 (6.13 ⁰)	0.093 (5.33 ⁰)
	Transducer length L, m (X_2)	0.019	0.019
	Transducer height H, m (X_3)	0.062	0.091
	Acoustic power, W (X_4)	0.7	0.9
	Incidence angle, Θ_i (X_5)	0.006 (0.34 ⁰)	0.005 (0.29 ⁰)
System characteristics	Steering range $\Delta\Theta$, rad	0.0106 (0.6 ⁰)	0.015 (0.95 ⁰)
	Diffraction efficiency η	1	0.997
	Klein-Cook parameter Q	86π	89π
	Center frequency f_c , MHz	26	21.3
	Acoustic bandwidth Δf , MHz	23.37	32.58

As one can see from Table 3.5, selection of the optimization criterion affects the results. It is also possible to maximize (minimize) a linear combination of several system characteristics taken with appropriate weights, then the resultant design presents a compromise between several, often mutually-contradictive, system requirements. It should also be noted that the acoustic power in Table 3.5 is calculated for the deflection angle $\Theta_d = 0$. As one can see from (3.32), increase in the deflection angle requires to use less power therefore, Table 3.5 features the maximum power consumption. Acoustic

attenuation reaches its highest value at the highest acoustic frequency and could be found as [2],

$$\alpha = \alpha_0 f_{\max}, \quad (3.34)$$

where α_0 – acoustic attenuation at 1 GHz. For TeO_2 this value is $17.9 \text{ dB}/\mu\text{sec} \cdot \text{GHz}^2$.

The highest acoustic frequency for the first optimization is 37.69 MHz, for the second – 37.59 MHz; therefore, the attenuation values are 0.0254 and 0.0253 dB/ μsec , respectively, which is very small numbers. The genetic algorithm optimization can potentially be used for more complicated tasks. For example, diffraction efficiency presented in Table 3.5 has been calculated for a certain value of acoustic power. However, as the sound wave propagates inside the crystal it attenuates, thus changing the value of diffraction efficiency in the direction of propagation. A cumulative criterion that accounts for different diffraction efficiencies as a function of distance from the transducer can be used. It is also possible to have more variable parameters and consider several characteristics that need to be optimized at a time.

3.6. Other Research Aspects

a - Multichannel Bragg cells

Using the same cell as a support to multiple beam steering has many interesting applications. The idea is to have different parallel channels taking different inputs and steering the input beam separately in different directions. The design procedure for each channel is the same as the one discussed for the regular cell. However, more design considerations are necessary. The distance between the transducers of two adjacent channels is critical to prevent any cross talking between the channels. This issue has been addressed in [3]. One way of limiting the cross talk is increasing spacing between the channels; however, doing so reduces the number of channels that can be used, reducing the throughput and overall diffraction efficiency. Another way implies the apodization of the transducer. Doing so reduces the sidelobes of the acoustic beam traveling through the cell, which minimizes the possibility of interference between the channels. The drawback of such a technique, as discussed in [3], is the fact that apodizing the transducer reduces the time aperture of the cell because the width of the main acoustic beam increases. Finally, [3] presents another way of preventing the cross talk. It consists of

using materials that exhibits self-collimation modes. In self-collimated modes, the Poynting vector describing the power flow in the material is orthogonal to the transducer reducing the acoustic divergence and, thus, the channels cross talk. The materials exhibiting such modes have generally an anisotropy parameter $b \approx 0.5$. Pape in [3] shows that using Gallium phosphide (GaP) presents both acceptable figure of merit and a good parameter $b=0.487$ offering an orthogonal acoustic direction of propagation.

b- Electro-optic Bragg cells

Some acousto-optic materials have allowed the reduction of the response time to the order of nanoseconds. Still, this reduction in the response time has decreased the diffraction efficiencies of the cells. One way to get both very high response time and high diffraction efficiency is the use of electro-optics. Indeed, by applying a voltage to two cathodes on top and bottom of the cell, and by special arrangements of the electrical domains in the cell, a grating is created inside the cell, and high response times can be achieved (1 nanosecond). Investigation of the behavior of such electro optic Bragg cells has been presented in [4]. Rise time of the order of 1 nanoseconds has been reached using a 633nm HeNe laser by applying an electric field on a periodically poled cell ($LiNbO_3$) between the top and bottom electrodes.

c- Monolithic two dimensional deflector

The idea is to achieve two-dimensional deflection using only one cell instead of two in series with one cell orthogonal to the other one. Barosci in [5] investigates the idea by considering the design specifications of a multichannel monolithic Bragg cell. The principle is to have the incident light diffracted in the horizontal direction, then have the diffracted x-light rediffracted in the vertical direction inside the same cell. Figure 3.13 [5] illustrates the working principle of a 2-dimensional deflector for birefringent TeO_2 .

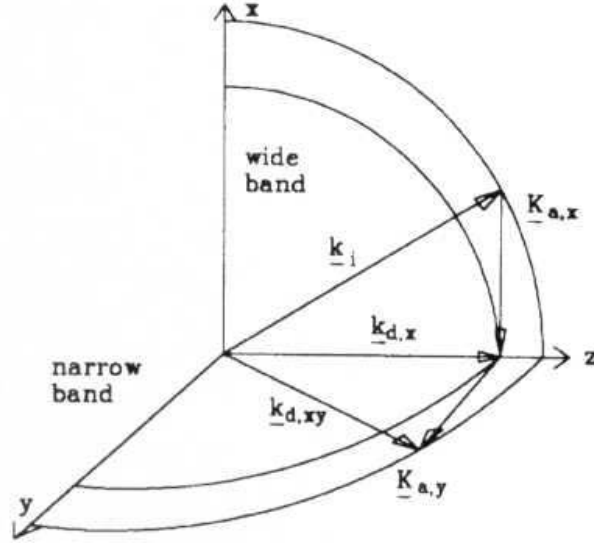


Figure 3.15. The wave-vector diagram of the 2D interaction

The bandwidths for the X and Y directions are given by

$$\begin{aligned}\Delta f_x &= \frac{v}{\lambda} \sqrt{\frac{2n_o}{\lambda L}} \\ \Delta f_y &= \frac{n_e v^2}{2\lambda f_o L}\end{aligned}\tag{3.35}$$

Where v - sound velocity

L - interaction length

n_o, n_e - ordinary and extraordinary indices of refraction of the cell.

and $f_o = \frac{v}{\lambda} \sqrt{n_e^2 - n_o^2}$ is the “acoustic midband frequency” as defined by [5].

There is an asymmetry between the two channels that is due to the fact that the interaction bandwidths are different, which can be minimized by using different interaction length [5]. Another issue is the use of the off-axis mode to avoid degenerate frequencies that cause rediffraction of the diffracted light as explained earlier.

Barosci then investigates the use of the 2-dimensional cell as a multichannel Bragg cell emphasizing on design parameters such as the channel cross talk, the active channel width and the total aperture of the cell. The total aperture of the cell is limited by the high attenuation factor, while the active channel width is responsible for the resolution. On the other hand, proper spacing between the channels should be provided to avoid unwanted interaction.

3.7. Conclusion

In this part of the project the main issues of the acousto-optic Bragg cell design and different design alternatives have been addressed. Recommendations for satisfying certain specifications such as steering range, diffraction efficiency, resolution, etc. are formulated. Two design approaches with acoustical and optical rotation have been considered. While some of the design methods involve graphical solution, and are rather complicated, we have developed a formal optimal design procedure utilizing the developed mathematical model of a Bragg cell and a genetic optimization tool. The procedure enables a designer to select a unique combination of system parameters that allow to meet design specifications and maximize the chosen performance criteria at the same time. The optimal design procedure could be recommended for many other tasks.

REFERENCES

- [1] Harry Presley, "High efficiency large time-bandwidth acousto-optic laser deflector for free space optical communications," Harris Corp. Technical Report.
- [2] J. Xu, R. Stroud, "Acousto-Optic Devices: Principles, Design and Application," John Wiley & Sons, 1992.
- [3] Dennis R. Pape, "Multichannel Bragg cells design, performance, and applications", *Optical Engineering*, Vol.10, pp 2148-2157, (1992).
- [4] H. Gnewuch, C. Pannell, G. Ross, P. Smith, H. Geiger, "Nanoseconds response of Bragg deflectors in periodically poled $LiNbO_3$ ", *IEEE Photonics technology Letters*, Vol. 10, pp. 1730-1732, (1998).
- [5] A. Barosci, L. jakab, I. Verhas, P. Richter, "Two-dimensional acoustooptic light diffraction and its applications", *Integrated Computer-Aided Engineering*, Vol. 3, pp. 108-116, (1996).

4. COMPARATIVE ANALYSIS OF ACOUSTO-OPTIC AND PIEZO-ELECTRIC STEERING TECHNOLOGY

Properties of the acousto-optic Bragg cell as a steering device have been extensively studied, and the results are presented in Chapters 1 – 3. Another approach that can be used for the same type of applications is piezo-electric technology. One of its many advantages is high resolution. It is possible to make extremely fine adjustment in the nm range [1].

4.1. Piezo-Electric Steering System Components

Piezo-electric mirrors are mirrors that depend on piezo-translators for positioning. The electric field applied to a translator applies a torque to an aligned dipole which causes a change in length in the monocrystalline regions. Typically high voltages (1000-2000 V) are used to generate these fields [2]. Such high voltages are a concern for a designer due to the possibility of arcing aboard the communication platform. Therefore, low-voltage piezo-translators are used. They have about the same expansion range, but are more susceptible to temperature changes.

The experimental analysis has been performed using a Physik Instrumente S-320 three-axis tilting mirror. The tilting plate supporting the mirror substrate rests on three piezo-electric translators that can be addressed individually. Collective expansion of all three piezo-electric elements results in linear movement. Individual operation provides tilting movement on two orthogonal axes, as well as linear translation.

The piezo-translators using low voltage technology require operating voltages in the range from -20 V to $+120\text{V}$ [1]. Compared to the high-voltage models they have larger capacities and require correspondingly larger currents to change their expansion. The task of providing these currents is accomplished with a piezo driver P-863.10. The velocity of the expansion depends on the maximum output current, and; therefore, on the output power of the piezo driver. The driver can be used in one of the two modes of operation:

- manual operation: The output voltage is set by a potentiometer. Therefore, it is possible to set any expansion value of the translator within the operation range.
- controlled operation: The required expansion of the translator is determined by an external control voltage. An offset can be added at the same time.

It has been mentioned that the piezo-translators are capable of very fine adjustments. However, in some cases hysteresis and drift can interfere. The hysteresis effect may cause a maximum difference of 10 – 15% of the nominal expansion. The drift is about 1 – 2% of the positioning movement per time decade [1]. Both these phenomena are properties of the piezo-effect and cannot be avoided. Therefore, they need to be automatically compensated by using sensors and operating in closed loop. The maximum accuracy depends on the sensors and control electronics. Strain gage sensors applied directly to the piezo-ceramic are used in the tilting mirror. They are switched as full bridges, and; therefore, not only capable of compensating hysteresis and drift, but also elastic deformations. The electronics operating the sensors is a piezo-controller E-808. It is a 3-axis control unit that allows highly accurate expansion of the three piezo-translators with integrated position sensors. The piezo-controller corrects expansion values by adjusting voltages.

4.2. Piezo-Electric Mirror Model

The mathematical model of the piezo-electric mirror and the control circuitry described in Section 4.1 is based on a series of laboratory experiments. A mathematical model of the system is described as follows

$$\begin{bmatrix} A(s) \\ E(s) \end{bmatrix} = \begin{bmatrix} g_{A1}(s) & g_{A2}(s) & g_{A3}(s) \\ g_{E1}(s) & g_{E2}(s) & g_{E3}(s) \end{bmatrix} \begin{bmatrix} V_1(s) \\ V_2(s) \\ V_3(s) \end{bmatrix} \quad (4.1)$$

A square wave has been applied to each input channel and the output of the quadrant detector representing azimuth and elevation channel response is recorded.

The experimentation has been performed as follows:

- 1) a 1 Hz square wave voltage signal with a magnitude of 0.02 V has been applied to the input of channel 1. Responses $A(s)=g_{A1}(s)*V_1(s)$ and $E(S)=g_{E1}(s)*V_1(s)$ have been recorded. The choice of 1 Hz input signal frequency provides enough time for the signals to reach the steady-state values. The amplitude of 0.02 V has been selected to ensure that we operate with displacement corresponding to the linear range of the quadrant detector. The recorded data contains complete information for obtaining transfer functions $g_{A1}(s)$ and $g_{E1}(s)$.
- 2) a 1 Hz square wave voltage signal with a magnitude of 0.02 V has been applied to the input of channel 2. Responses $A(s)=g_{A2}(s)*V_2(s)$ and $E(S)=g_{E2}(s)*V_2(s)$ have been recorded. The recorded data contains complete information for obtaining transfer functions $g_{A2}(s)$ and $g_{E2}(s)$.
- 3) a 1 Hz square wave voltage signal with a magnitude of 0.02 V has been applied to the input of channel 3. Responses $A(s)=g_{A3}(s)*V_3(s)$ and $E(S)=g_{E3}(s)*V_3(s)$ have been recorded. The recorded data contains complete information for obtaining transfer functions $g_{A3}(s)$ and $g_{E3}(s)$.
- 4) the experiments described in steps 1), 2), and 3) have been repeated with a square wave voltage signal with a magnitude of 0.04 V to detect possible nonlinearities in the system response. The results ensured that we operate in the linear range, and the piezo-controller compensates for hysteresis and drift.

Details of the experimentation are presented in Fig. 4.1, Fig. 4.2, and Fig. 4.3. They illustrate response of the mirror system to a step signal applied to channel 1, channel 2, and channel 3, respectively.

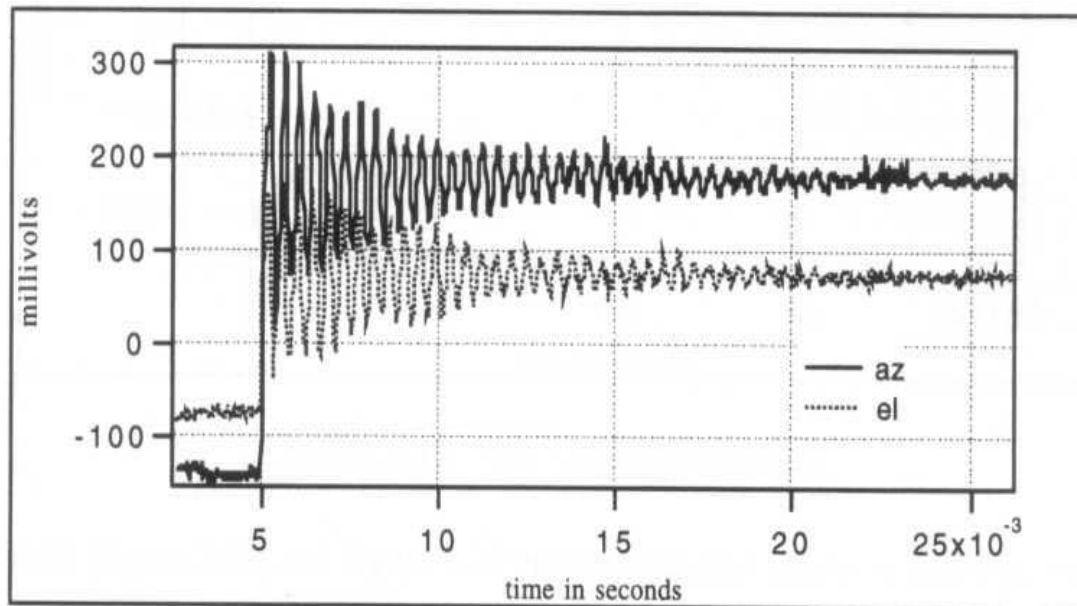


Figure 4.1. Step response for Channel 1

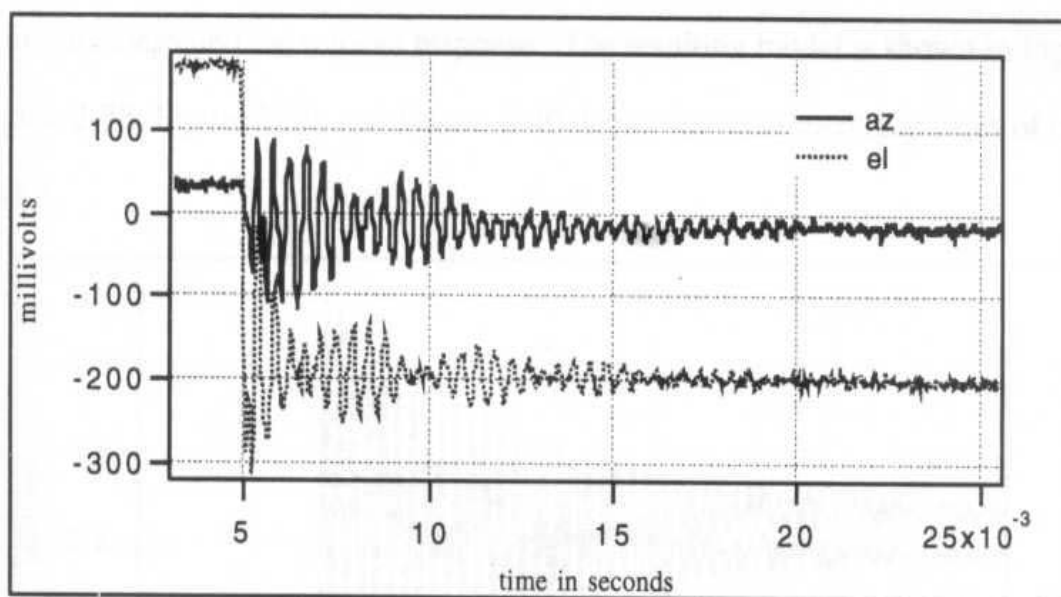


Figure 4.2. Step response for Channel 2

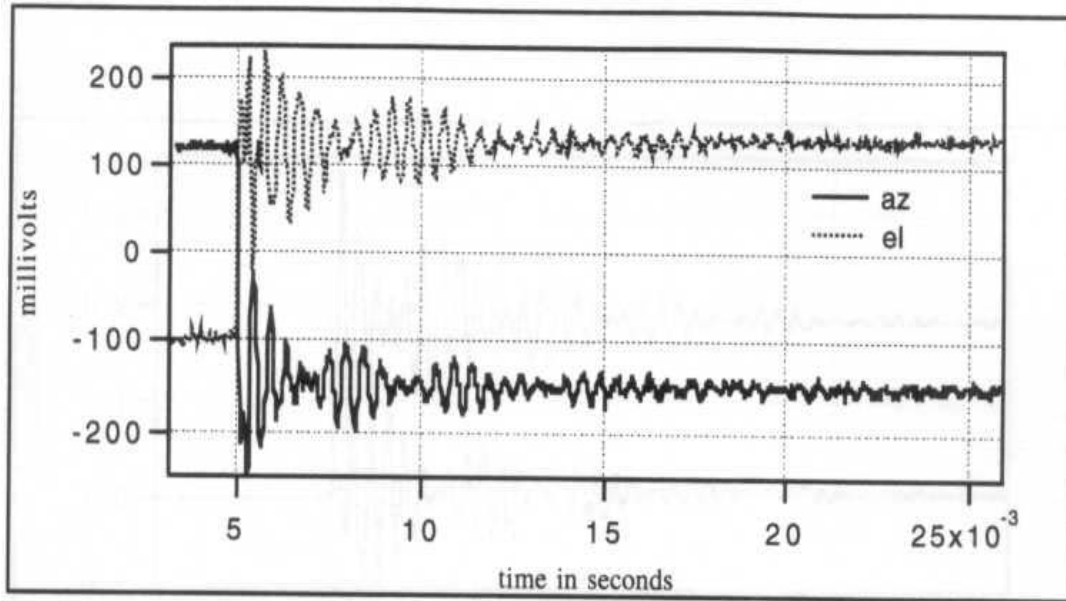


Figure 4.3. Step response for Channel 3

The measurements reveal a significant degree in cross coupling. It can be seen that for each experiment a signal applied to one channel results in response in both outputs. The beat present in the channel 2 and channel 3 responses serves as an evidence of exchange of bending modes. This corresponds to the situation when the system has 3 zeros and 4 poles. A combination of second order systems has been used to model each dynamic channel. Parameters of these systems have been manually tuned until response of the model resembled experimentation results. Fig. 4.4 presents a simulation setup for the linear model obtained as a result of experimentation.

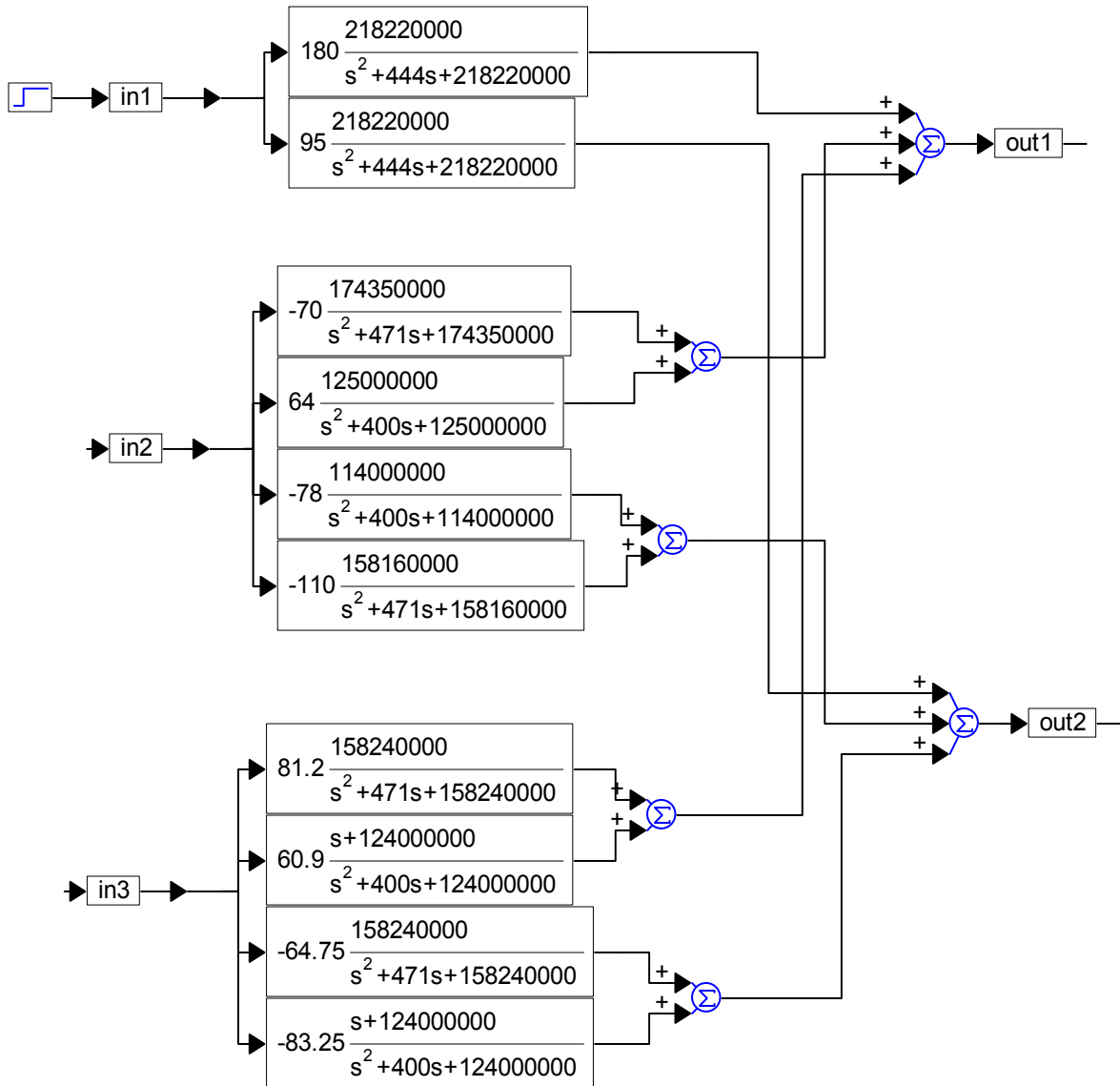


Figure 4.4. VISSIM simulation model of the piezo-electric mirror

The resulting model responses are presented in Fig. 4.5, Fig. 4.6, and Fig. 4.7. It may appear from the transfer functions presented in Fig. 4.4 that the bandwidth of the device is very high. However, very low dumping ratio causes an oscillatory process and it takes much more time for the system to settle to its steady-state value. Therefore, the effective bandwidth of the system is significantly lower.

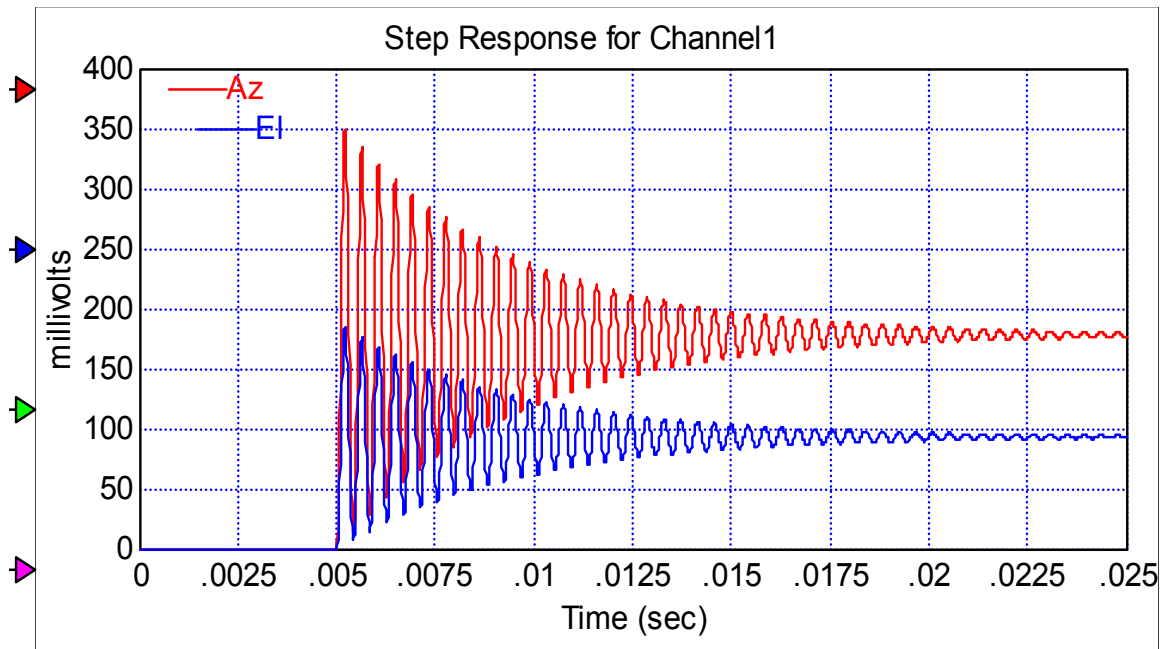


Figure 4.5. Simulated step response for Channel 1

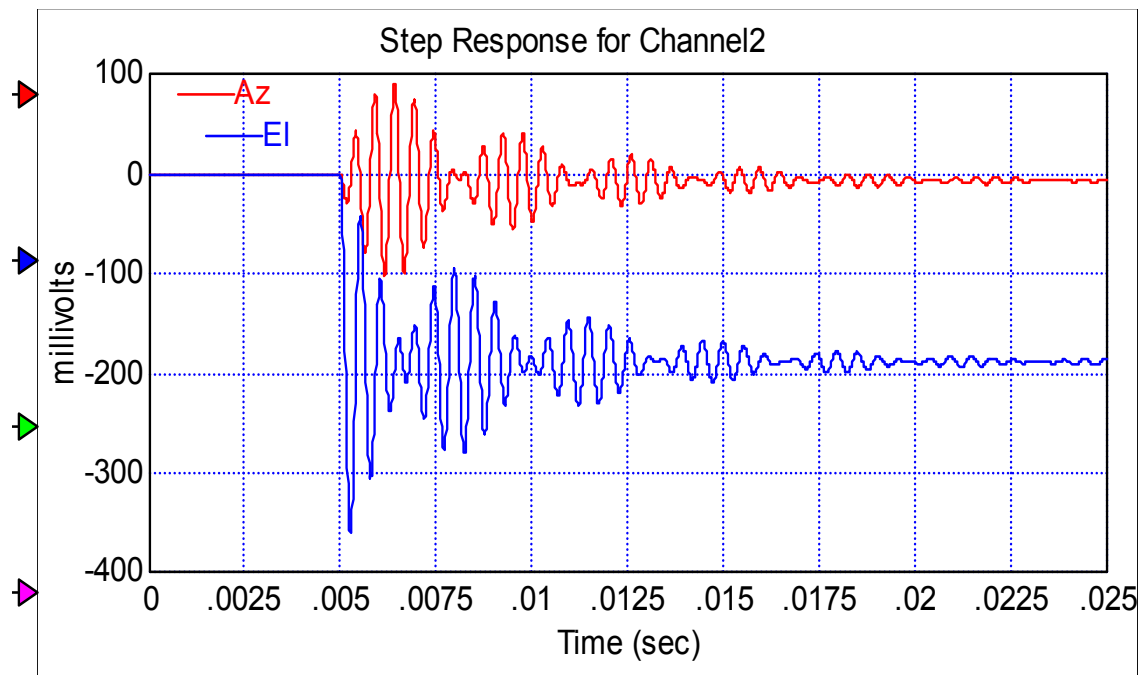


Figure 4.6. Simulated step response for Channel 2

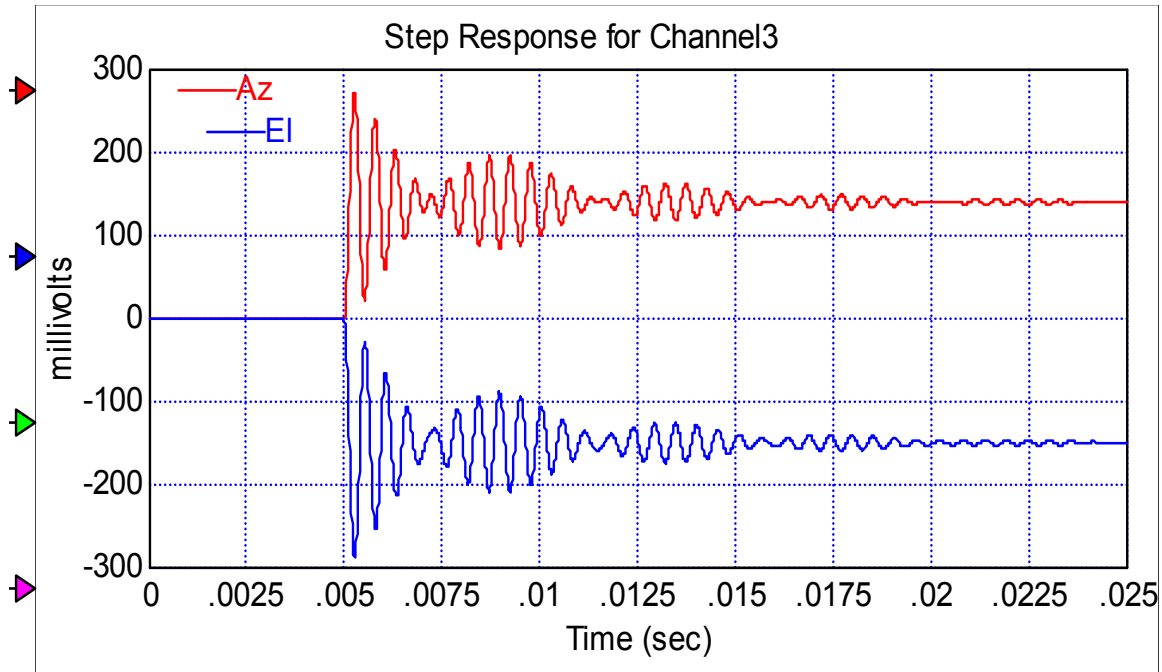


Figure 4.7. Simulated step response for Channel 3

4.3. Comparative Analysis

The two technologies: acousto-optic and piezo-electric can be compared using several characteristics. Both acousto-optic Bragg cells and piezo-electric mirrors are advanced deflector devices. Their advantage versus mechanical steering mirrors is smaller size, weight, and power consumption. The principle of acousto-optic deflection is better in the sense that the system does not have any moving mechanical parts. Therefore, Bragg cell response time is faster, and the bandwidth is larger. The system dynamics can be described by a first-order transfer function; therefore, there is no overshoot in system response.

The piezo-electric mirror not only experiences overshoot, but also exhibits oscillations (due to very low dumping ratio) and cross coupling between the dynamic channels. The Bragg cell-based steering systems do not have any coupling, but each device is capable of deflecting the beam only in one direction (vertical or horizontal). As a result a combination of two devices is necessary to achieve two-dimensional steering.

Resolution of both devices essentially depends on the driver electronics. For the piezo-electric mirror it is a function of the voltage step that the piezo-driver can produce

and also accuracy of the sensors integrated on the piezo-translators. For the Bragg cell it depends on the frequency step of the RF signal applied to the transducer. Acousto-optic cell input-output characteristics are linear for the case when it operates in the near Bragg regime. The piezo-translators have non-linear response (due to hysteresis and drift) that needs to be constantly corrected. The fact that the Bragg cell driver operates in the open loop mode (it does not have a feedback like sensor signals for the piezo-controller) makes it more reliable.

Optical efficiency of the piezo-electric mirror is better, and most of the incident light is deflected. Acousto-optic cells have larger optical losses (up to 20%). However, this value can be manipulated with proper design steps. Optimal selection of the physical dimensions, as well as acoustic power can maximize diffraction efficiency. The advantage of the mirror is that its optical efficiency is independent of the steering angle. For the Bragg cell it depends on the acoustic frequency, and as a rule, decreases with higher deflection angles.

Another parameter for comparison is power consumption. The Bragg cell has no moving parts, and usually requires less power per channel. In addition, the response time of this device depends mostly on material properties and beam size. Contrary to the acousto-optic devices, the speed of expansion of the piezo-translators depends on the power provided by the driver. The power of the Bragg cell; however, may need some adjustment in the process of operation, if, depending on the acoustic frequency, diffraction efficiency is being maximized.

Dimensions of the two types of steering devices, as well as their weights are very close.

Finally, the last characteristic for qualitative comparison is the field-of-regard, or steering range. Even though the piezo-electric mirror is a mechanical system, its range of operation is very small due to expansion limits of the piezo-translators. The Bragg deflectors with their usual steering range of 1° or less are still more advantageous in terms of this characteristic.

The comparison of two systems installed in our laboratory is summarized in Table 4.1.

Table 4.1. Properties of Bragg cells and piezo-electric mirrors

Parameter	Bragg Cell	Piezo-Electric Mirror
Bandwidth, Hz	≈ 15000	≈ 500
Resolution, μrad	depends on driver	≈ 5
Optical Efficiency	$\approx 84\%$	$\geq 95\%$
Power, W	0.4 per channel	5 per channel
Weight	small	small
Size (unmounted)	42x34x30 mm	40x20x20 mm
Steering Range, mrad	≈ 5.8	≈ 2
Cross-Coupling	almost none	significant

Note that resolution of the Bragg cell is not specified, since all experiments have been conducted using a driver with limited acoustic frequency resolution. Steering resolution of the piezo-electric mirror is limited by accuracy of the integrated expansion sensors.

4.4. Conclusion

In this part of the project a comparison between two advanced steering devices: Bragg cells and piezo-electric mirrors has been performed. A series of experiments has been conducted to obtain dynamic response of the piezo-electric steerer. A mathematical model based on the experimental data has been developed. Comparative analysis has been performed in terms of such characteristics as tracking bandwidth, steering resolution, attenuation of beam intensity, power consumption, weight/size, and range of linear operation.

REFERENCES

- [1] Products for micropositioning. Physik Instrumente vendor databook.
- [2] Timothy E. Busch, “Beam Steering Techniques for Free-Space Laser Communication,” Ph.D. Dissertation. Binghamton, NY, 1997

5. MODEL REFERENCE ADAPTIVE CONTROL

The laser beam steering open-loop system model has been established and validated. The adaptive model reference controller is designed and tested. A full description of the controller design is provided. The robustness and efficiency of adaptive control is demonstrated.

5.1. Simulation Analysis Of The Existing System

A simulation model of the entire beam positioning system is implemented in VISSIM software, and simulations are performed. The open-loop simulation diagram is shown in Fig. 5.1.

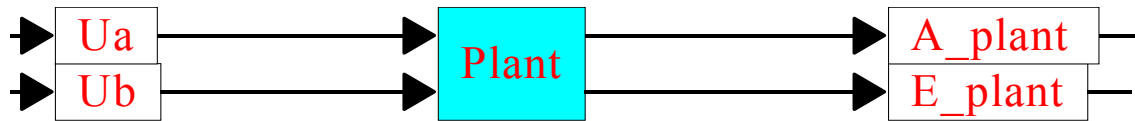


Figure 5.1. Open loop simulation block diagram

The inputs “Ua” and “Ub” are the desired azimuth “X” and elevation “Y” position of the beam, and the outputs “A_plant” and the “E_plant” are the voltages generated by the detector indicating the actual azimuth and elevation displacements. The compound block “Plant” contains the simulation model of both Bragg cells and the quadrant detector as shown in the Fig. 5.2 below. The two Bragg cells are placed in the horizontal and vertical channels. Their outputs are connected to the quadrant detector model that computes the elevation and azimuth position of the beam. The reference signal is the desired beam position on the quadrant. Using the distance between the Bragg cell and the detector, the necessary deflection angle is estimated, and translation from the coordinates into acoustic frequency is performed using equations from Chapter 1. This task is performed in the blocks “XtoF” and “YtoF”. The deflection angles are computed in the blocks “Horizontal deflection” and “Vertical deflection”, and the linear displacement of

the beam center on the quadrant detector is computed in “Def_X” and “Def_Y”. The Delay block in both channels represents the 8 μsec time interval that is needed for the acoustic wave to propagate from the bottom of the cells to the beam. During this time, no sound-light interaction occurs, which explains the use of the pure delay function. After, the delay blocks, there are lag filters in both channels. These lag filters simulate the response time of each cell when light-sound interaction occurs. Physically, as explained in Chapters 1 and 2, this is the time needed for the sound wave to traverse the beam inside the cell. It has been computed and experimentally verified that the response time is 40 microseconds for the horizontal cell, and 20 microseconds for the vertical cell resulting the following transfer functions:

$$\text{Horizontal Channel: } \frac{100000}{s + 100000}$$

$$\text{Vertical Channel: } \frac{200000}{s + 200000}$$

The outputs “X_Dis” and “Y_Dis” are used as inputs to the quadrant detector model. As has been described in Chapter 2 it is obtained by approximating the surface with a Radial-Basis-Function neural network with a set of 31 Gaussian functions for each channel.

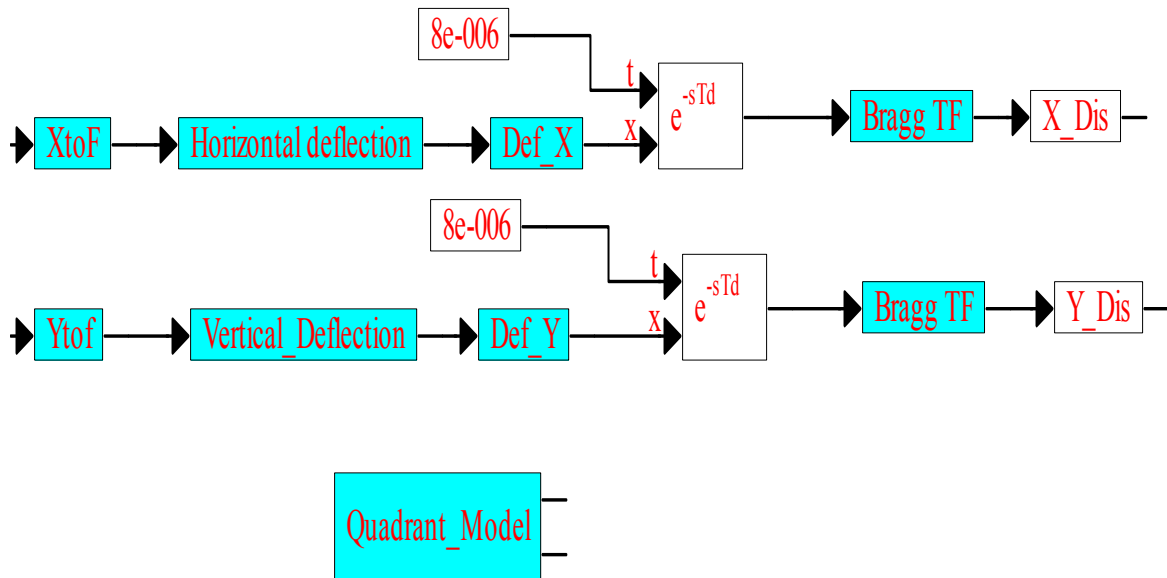


Figure 5.2. Plant compound block.

Using the appropriate time step, operation of the system is simulated. Coupling and non-linearity of the overall system is demonstrated. Figure 5.3 shows the simulation results of the open-loop system as input X is kept constant at 200 microns, while desired position Y starts also at 200 microns, but is changed to 550 microns after 500 μ sec and then decreased to 300 microns after 1500 μ sec.

From Fig. 5.3, one can see that the system exhibits undesirable behavior in the azimuth channel when only the elevation channel is excited. The outputs of both the azimuth and elevation channels are not linearly related to the inputs. Moreover, we can observe that when the command input for the elevation channel decreases from 550 to 300 microns, the output voltage of the corresponding channel of the quadrant detector increases.

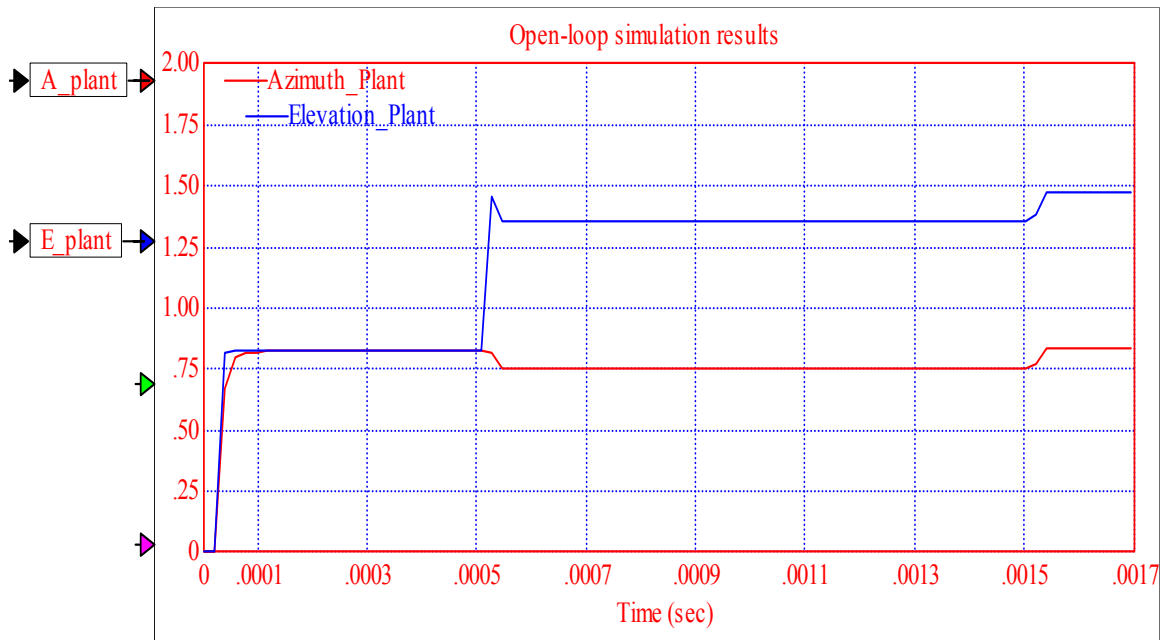


Figure 5.3. Open-loop simulation results

This can be explained by coupling and non-linearity of the quadrant detector. The mathematical expressions that describe this device are highly nonlinear due to the presence of a sum of different Gaussian function with different centers.

The system does not exhibit any overshoot being a 2-input-2-output system with first order dynamic channels. The settling time of the overall system is 40 microseconds offering a tracking bandwidth of 25KHz.

The control system to be designed should decouple the plant, linearize it and offer a tracking bandwidth of 3KHz. The design of the model reference controller is accomplished using the hyperstability and positivity procedure.

5.2. Design Of The Reference Model Controller

The controller design procedure has to be performed in two stages[1, 2]. First, we design a linear model-following (LMF) system using a “best guess” definition of the plant. After this stage the system is augmented with an adaptive model-following (AMF) control part.

A-The LMF design:

The system “best guess” state variable equations are:

$$X_1' = -200000 * X_1 - 50000 * X_2 + 200000 * Ua$$

$$X_2' = -50000 * X_1 - 200000 * X_2 + 200000 * Ub$$

or simply

$$X' = Ap * X + Bp * U$$

and the output equations are:

$$a = X_1$$

$$e = X_2$$

where

$$Ap = \begin{bmatrix} -200000 & -50000 \\ -50000 & -200000 \end{bmatrix} \quad \text{and} \quad Bp = \begin{bmatrix} 200000 & 0 \\ 0 & 200000 \end{bmatrix}$$

First we assume that the desired Acl matrix is given by:

$$Acl = \begin{bmatrix} -6000 & 0 \\ 0 & -6000 \end{bmatrix}, \quad \text{with} \quad Acl = Ap - Bp * F,$$

where F is a 2x2 matrix of the state variable feedback controller. F has the form:

$$F = \begin{bmatrix} f_{11} & f_{12} \\ f_{21} & f_{22} \end{bmatrix} \text{ so } BpF = \begin{bmatrix} 200000 * f_{11} & 200000 * f_{12} \\ 200000 * f_{21} & 200000 * f_{22} \end{bmatrix} \text{ and}$$

$$Ap - Bp * F = Acl$$

yields:

$$-200000 - 200000 * f_{11} = -6000$$

$$-50000 - 200000 * f_{12} = 0$$

$$-200000 - 200000 * f_{22} = -6000$$

$$-50000 - 200000 f_{21} = 0$$

So F is given by

$$F = Kp = \begin{bmatrix} -0.97 & -0.25 \\ -0.25 & -0.97 \end{bmatrix}.$$

If state variable controller F is used by itself, the system will not meet the desired specifications, and will still be coupled due to non-linearity and parameter uncertainties of the plant. To obtain a closed loop system as desired, let us assume that the design specifications have changed, and let us define the LMF system by finding Km, and Ku.

The desired reference model of the system is given by:

$$Z' = Am * Z + Bm * R, \text{ and } Ym = Cm * Z,$$

where

$$Am = \begin{bmatrix} -12000 & 0 \\ 0 & -12000 \end{bmatrix}, Bm = \begin{bmatrix} 12000 & 0 \\ 0 & 12000 \end{bmatrix}, \text{ and } Cm = \begin{bmatrix} 1 & 0 \\ 0 & 1 \end{bmatrix}, \text{ and}$$

R=U the input vector to our system.

Km and Ku should satisfy:

$$Am - Ap + Bp * F - Bm * Km = 0 \text{ and,}$$

$$Bm = Bp * Ku$$

We have:

$$Ap - Bp * F = Acl \text{ so,}$$

$$Bm * Km = \begin{bmatrix} 12000 * Km11 & 0 \\ 0 & 12000 * Km22 \end{bmatrix} = Am - Acl.$$

Solving for Km yields:

$$Km = \begin{bmatrix} -0.5 & 0 \\ 0 & -0.5 \end{bmatrix}.$$

Ku is given by $Bp * Ku = Bm$, so:

$$\begin{bmatrix} 200000 & 0 \\ 0 & 200000 \end{bmatrix} * \begin{bmatrix} Ku11 & Ku12 \\ Ku21 & Ku22 \end{bmatrix} = \begin{bmatrix} 200000 * Ku11 & 0 \\ 0 & 200000 * Ku22 \end{bmatrix} = \begin{bmatrix} 12000 & 0 \\ 0 & 12000 \end{bmatrix}$$

Solving for Ku gives:

$$Ku = \begin{bmatrix} 0.06 & 0 \\ 0 & 0.06 \end{bmatrix}$$

The designed LMF system as defined by the matrices F, Km, and Ku, is valid for the “best guess” plant only. Indeed, if the plant is exactly defined by the “best guess” state-space model, then the appropriate control is provided, and the resultant closed loop system will exhibit the desired behavior. However, in our case the best guess plant does not describe the exact system as present in the real plant. Using only the LMF design without an adaptation mechanism does not satisfy the performance requirements for the system as shown in Fig. 5.4.

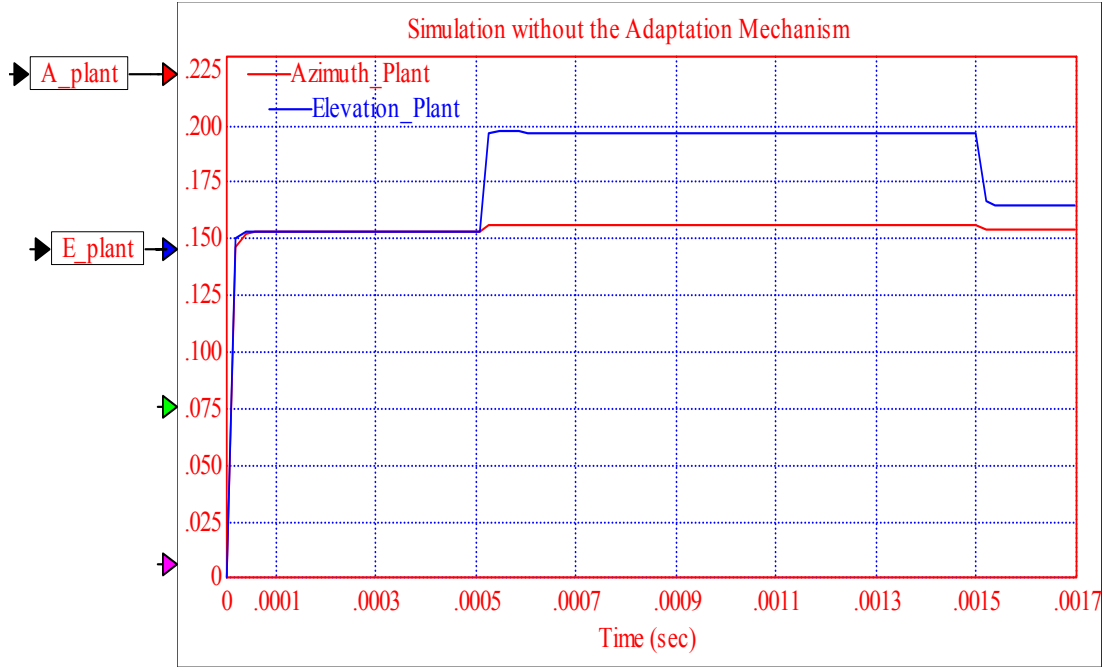


Figure 5.4. Closed-loop simulation results without the adaptation mechanism.

There is a need to come up with an adaptation mechanism that will use the error between the plant output and the reference model to adjust the matrices K_m , and K_u . This is accomplished by upgrading our LMF system to an adaptive model-following (AMF) system using the hyperstability and positivity approach.

B-The AMF system design:

Following the proper procedure, a successful design includes the definition of matrix D , the definition of the intermediate variable V , and the selection of the matrix functions $\phi_1(v, t, \tau)$ and $\psi_1(v, t, \tau)$.

1-Matrix D definition:

Matrix D is defined by solving first for matrix P, such that:

$$(Am - Bm * Km)^T * P + P * (Am - Bm * Km) = -I ,$$

Where

$$Am - Bm * Km = Acl ,$$

so P is defined by solving the Lyapunov equation:

$$(Acl)^T * P + P * (Acl) = -I ,$$

Where

$$Acl = \begin{bmatrix} -6000 & 0 \\ 0 & -6000 \end{bmatrix} ,$$

And P has the form $\begin{bmatrix} p11 & p12 \\ p21 & p22 \end{bmatrix}$

Solving the Lyapunov equation in MATLAB, yields:

$$P = \begin{bmatrix} 0.833 * 10^{-4} & 0 \\ 0 & 0.833 * 10^{-4} \end{bmatrix} , \text{ then D is computed using:}$$

$$D = B^T * P = \begin{bmatrix} 200000 & 0 \\ 0 & 200000 \end{bmatrix} * \begin{bmatrix} 0.833 * 10^{-4} & 0 \\ 0 & 0.833 * 10^{-4} \end{bmatrix} , \text{ so:}$$

$$D = \begin{bmatrix} 16.66 & 0 \\ 0 & 16.66 \end{bmatrix}$$

2- Vector V Definition

$$V = D * (Z - X) = D * e = \begin{bmatrix} 16.66 & 0 \\ 0 & 16.66 \end{bmatrix} * \begin{bmatrix} e1 \\ e2 \end{bmatrix} , \text{ so:}$$

$$v1 = 16.66 * e1$$

$$v2 = 16.66 * e2$$

3-Definition of matrix functions $\phi_1(v, t, \tau)$ and $\psi_1(v, t, \tau)$.

The adaptation mechanism that provides the controller's parameters adjustment is based on the definition of $\Delta Kp(e, t)$ and $\Delta Ku(e, t)$. These two functions are defined as:

$$\Delta Kp(e, t) = \int_0^t \Phi_1(v, t, \tau) d\tau + \Phi_2(v, t) + \Delta Kp(0)$$

$$\Delta Ku(e, t) = \int_0^t \Psi_1(v, t, \tau) d\tau + \Psi_2(v, t) + \Delta Ku(0)$$

For computational simplicity purposes, we can assume that:

$$\begin{aligned}\Phi_2(v,t) &= 0 \\ \Psi_2(v,t) &= 0\end{aligned}$$

and define $\phi_1(v,t,\tau)$ and $\psi_1(v,t,\tau)$ as :

$$\begin{aligned}\Phi_1(v,t,\tau) &= H * V(\tau) * X^T * G \\ \Psi_1(v,t,\tau) &= M * V(\tau) * R^T(\tau) * N\end{aligned}$$

Where $H, G, M, N > 0$

We have:

$$\begin{aligned}V * X^T &= \begin{bmatrix} v1 \\ v2 \end{bmatrix} * \begin{bmatrix} x1 & x2 \end{bmatrix} = \begin{bmatrix} v1x1 & v1x2 \\ v2x1 & v2x2 \end{bmatrix}, \text{ and} \\ V * R^T &= \begin{bmatrix} v1 \\ v2 \end{bmatrix} * \begin{bmatrix} Ua & Ub \end{bmatrix} = \begin{bmatrix} v1 * Ua & v1 * Ub \\ v2 * Ua & v2 * Ub \end{bmatrix}\end{aligned}$$

Selecting $H=M=I$, and selecting $G=N=100000*I$ results in:

$$\begin{aligned}\Phi_1(v,t,\tau) &= \begin{bmatrix} 100000 * v1 * x1 & 100000 * v1 * x2 \\ 100000 * v2 * x1 & 100000 * v2 * x2 \end{bmatrix} \\ \Psi_1(v,t,\tau) &= \begin{bmatrix} 100000 * v1 * Ua & 100000 * v1 * Ub \\ 100000 * v2 * Ua & 100000 * v2 * Ub \end{bmatrix}\end{aligned}$$

5.3. Testing Of The Model Reference Controller By Computer Simulations

The simulation setup of the closed-loop system as implemented in VISSIM for testing purposes of the designed adaptive controller is shown in Fig. 5.5. The compound block “Characteristics Definition” contains the initialization of all the variables used in the system. These include the center frequencies of the Bragg cells, the wavelength of the laser, as well as the velocity of the sound propagating inside the Bragg cells. The “References” block contains the input signals identifying positions where the beam is to be steered. The “Reference Model Block” defines desired static and dynamic characteristics of the system according to the design specifications. It includes two linear and decoupled channels. The “Adaptation Mechanism” is the implementation of the defined V vector, the $\Delta Kp(e,t)$ and $\Delta Ku(e,t)$ function. Finally, the “Control effort” block implements the control law for both channels defined by:

$$Up = -Kp(e,t) * X + Km * Z + Ku(e,t) * U ,$$

where

$$Kp(e,t) = F - \Delta Kp(e,t)$$

$$Ku(e,t) = Ku + \Delta Ku(e,t) \quad ,$$

which implies:

$$Up = Up1 + Up2 ,$$

where

$$Up1 = -Kp * X + Km * Z + Ku * U$$

$$Up2 = \Delta Kp(e,t) * X + \Delta Ku(e,t) * U$$

Up1 is the linear control part, and Up2 the nonlinear control effort.

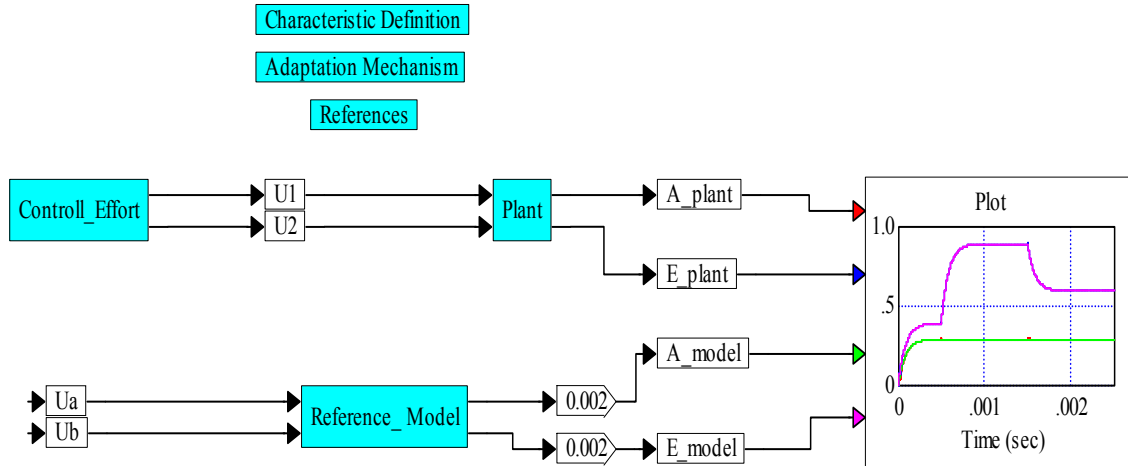


Figure 5.5. Closed-loop adaptive control system simulation setup

After the system is implemented, the model reference controller is first tried with the “best guess” definition of the plant. The designed system performed successfully, the plant outputs have been decoupled and linearly related to the inputs as specified by the reference model. The AMF system design robustness has been tested with the real plant model exhibiting high nonlinearity and coupling. Once again, as can be seen in Fig. 5.5, the objective is successfully achieved. The two channels of the plant are decoupled and linearized, thus, robustness of the model reference controller is demonstrated. The introduction of the controller allowed the change of our hardware behavior without having to redesign the hardware itself. Indeed, the quadrant detector does not cause any

more coupling and does not introduce any nonlinearity in our dynamic channels. We set the azimuth command to 150 microns. For the elevation channel initial desired position is set to 200 microns; after 3 msec, the elevation position is changed to 450 microns, and then is stepped down to 300 microns after 5 msec, while the azimuth position is kept unchanged. More information on the simulation results is presented in Fig. 5.6 – Fig. 5.9. Azimuth channel response is presented in Fig. 5.6. One can see how the model-reference control system adapts to decrease the discrepancy between the actual and desired positions. Initially the system performs poorly, during the second transient it settles back to the desired value faster; finally, during the last transient the discrepancy is considerably small. This shows how the system “learns” from the tracking error.

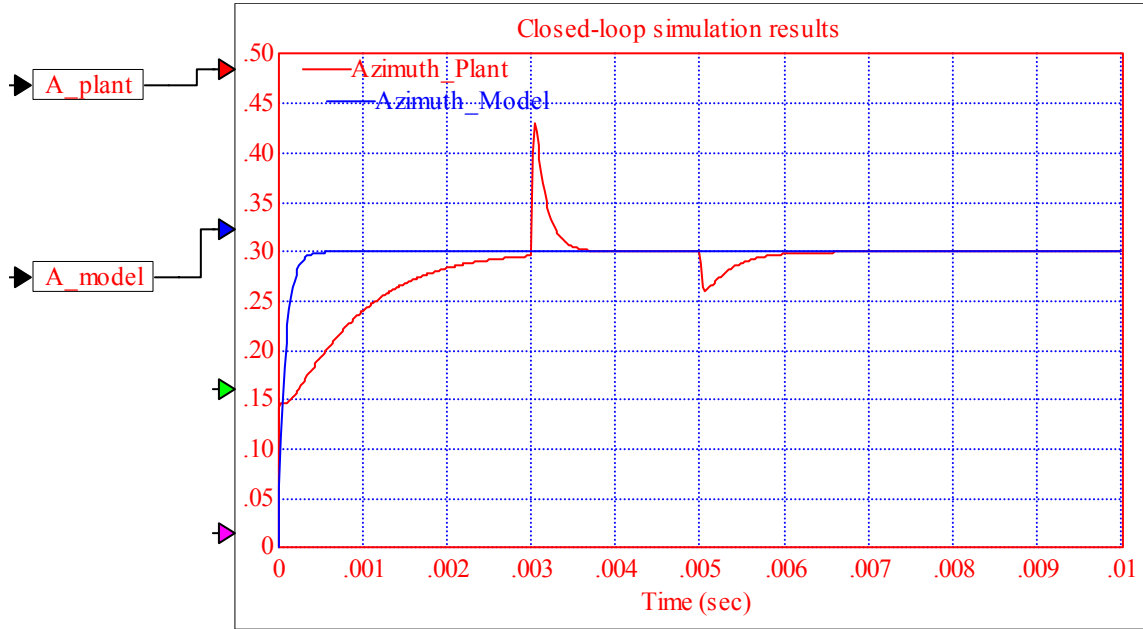


Figure 5.6. Simulation results for the azimuth channel of the AMF control closed-loop system

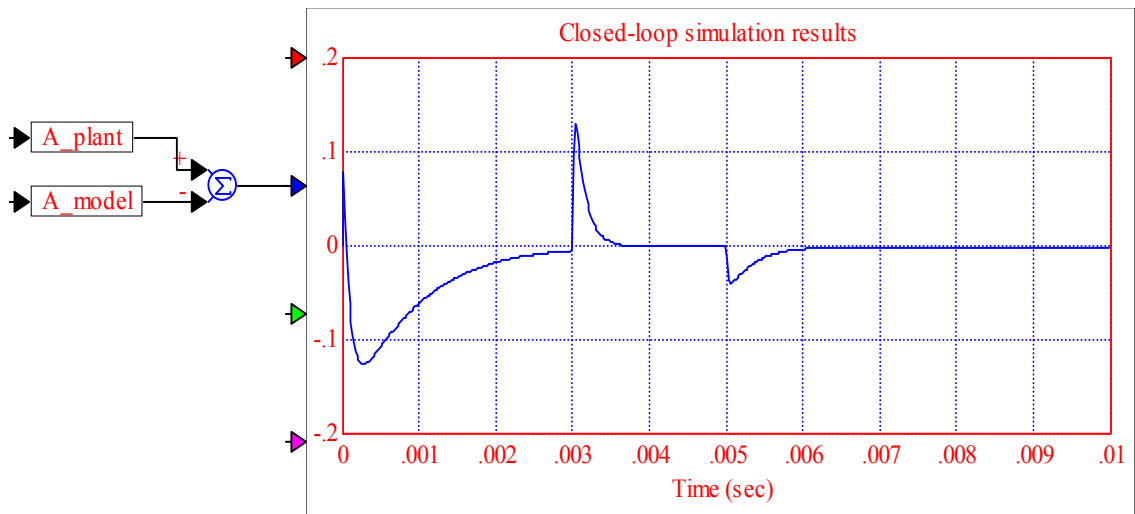


Figure 5.7. Tracking error in the azimuth channel

Figure. 5.7 presents the difference between the outputs of the reference model and the plant. As can be seen from the figure, in steady state the error converges to 0.

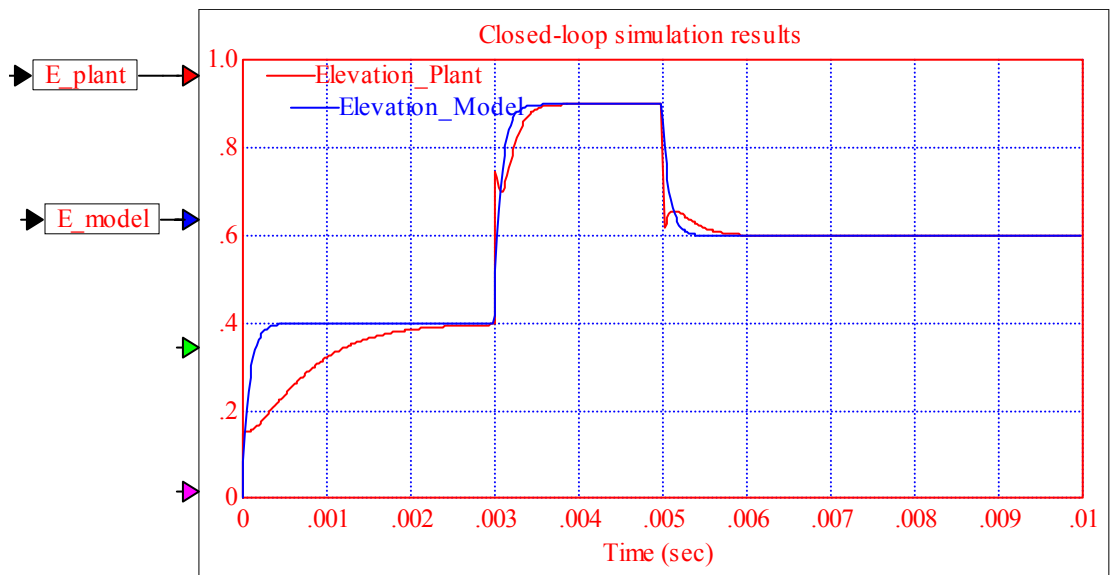


Figure 5.8. Simulation results for the elevation channel of the AMF control closed-loop system

Fig. 5.8 illustrates response in the elevation channel. One can see behavior similar to that in the azimuth channel: the plant output converges to the reference model signal with less error being generated with every successive transient (see Fig. 5.9). This can be explained by the initial condition of the controllers. For this experiment they have been set to 0, which is the main cause for large error in the beginning of the first transient.

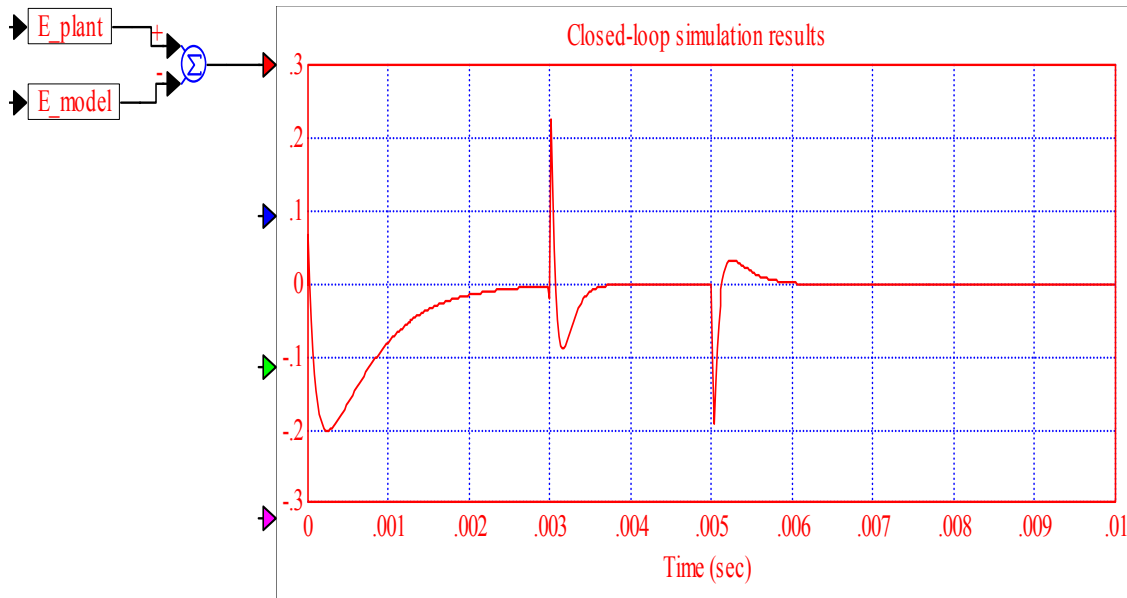


Figure 5.9. Tracking error in the elevation channel

Proper selection of initial conditions may help to improve the initial transient. In real application the simulation model can be used to adjust parameters of the adaptive system off-line, and use those parameters with the hardware.

It can be seen from the simulation results presented in Fig. 5.6 – Fig. 5.9 that even though as time goes on, the magnitude of the error during each transient decreases, the error itself never diminishes. We can also observe that after initial adaptation, when the next transient occurs, error convergence time is constant and approximately equal to 8 μsec . This number is related to the propagation delay τ introduced in our model in Chapter 1, and experimentally estimated to be 8 μsec , as has been shown in Chapter 2. This delay is associated with the time necessary for the sound wave to propagate from the transducer to the beam; therefore, better alignment can reduce this delay and improve the

system performance. Fig. 5.10 – Fig. 5.13 present simulation results for a “good alignment” case when the propagation delay $\tau = 0$.

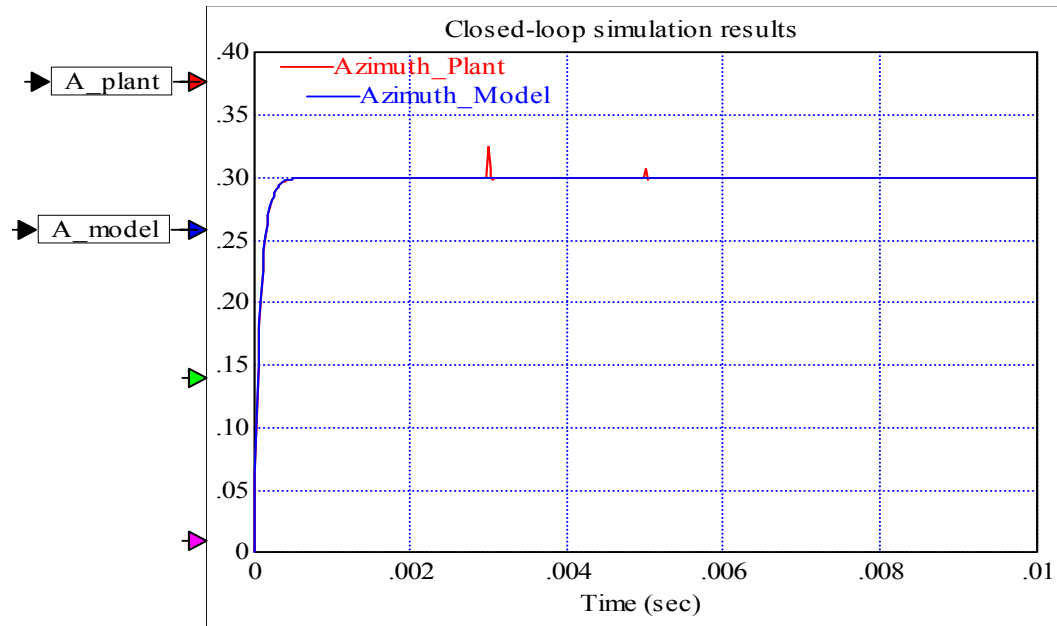


Figure. 5.10. Azimuth channel response for $\tau = 0$

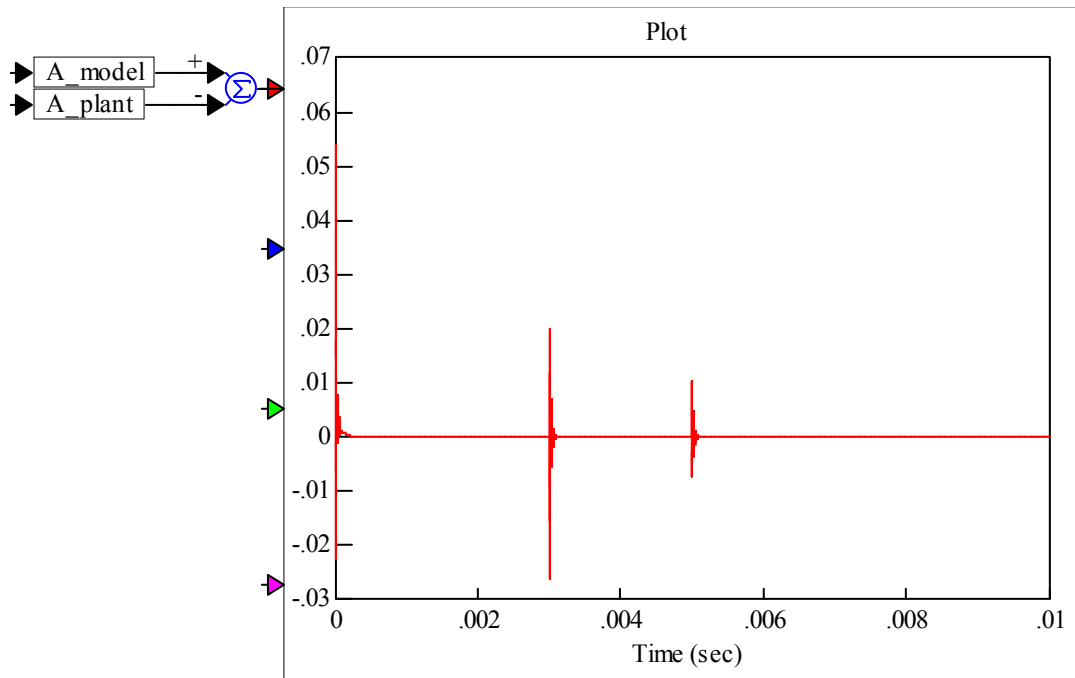


Figure. 5.11. Azimuth channel tracking error for $\tau = 0$

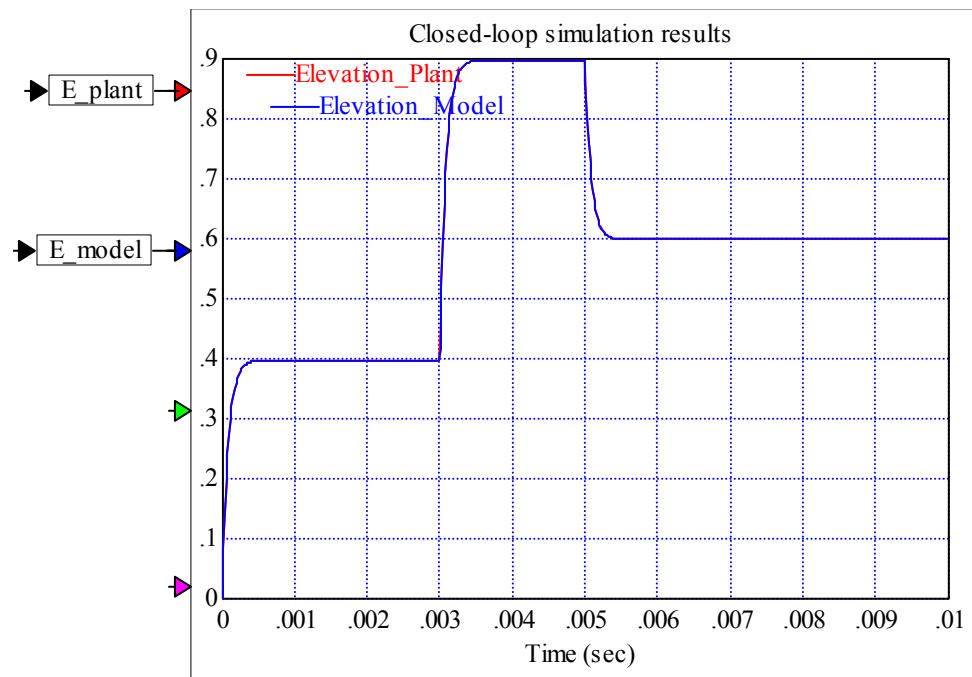


Figure. 5.12. Elevation channel response for $\tau = 0$

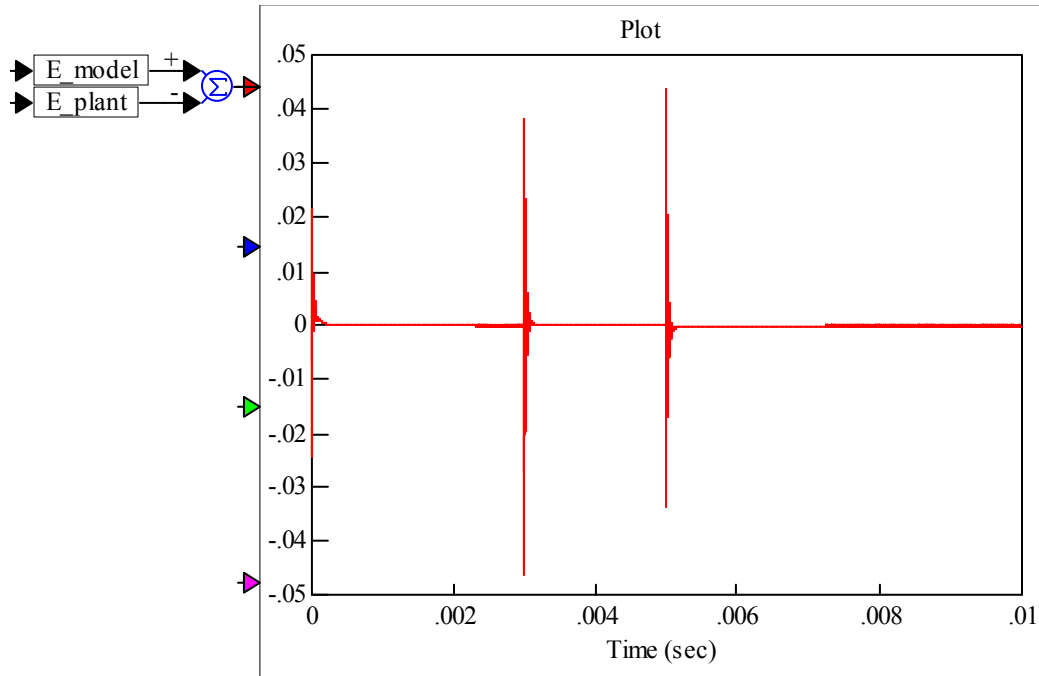


Figure. 5.13. Elevation channel tracking error for $\tau = 0$

5.4. Jitter Rejection

In order to simulate satellite jitter, different simulation methods can be used [3, 4, 5]. A noise with frequencies ranging between 1KHz and 3KHz has been considered. In order to simulate it, a random gaussian generator has been used and its signal has been added to beam displacement, thus modeling platform vibration. A pass-band FIR filter with cutoff frequencies of 1000 Hz for the lower limit, and 3000 Hz for the upper limit and a Hanning-type window has been used to select the frequencies of interest. A magnitude of 5 micron is chosen to provide a reasonable S/N ratio. Fig. 5.14 presents a sample of injected noise.

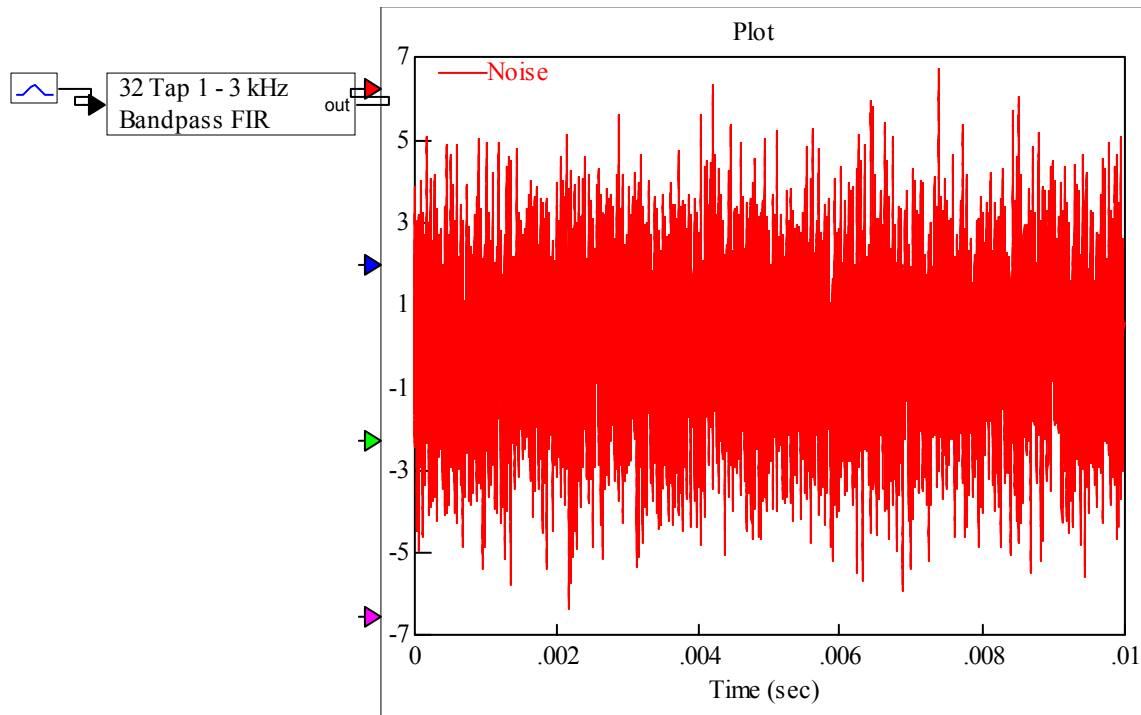


Figure 5.14 Noise sample after appropriate filtering

A summary of the results obtained by simulation is given. First the noise is injected in the azimuth channel. Fig. 5.15 and 5.16 present the plots of system response to noise signal. To obtain these plots, system response to a step input has been obtained. Then a similar simulation has been performed with the signal applied to the plant being “contaminated” with noise. The selected signal-to-noise ratio (SNR) is 250. The difference between two simulation results presents system response to disturbance (platform jitter effects).

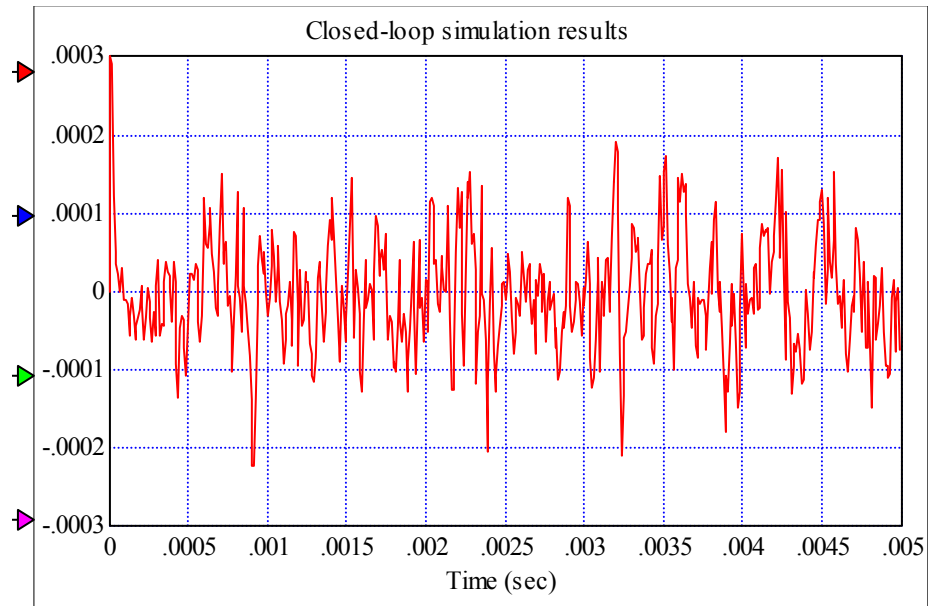


Figure 5.15 Azimuth response to noise signal injected in the horizontal channel

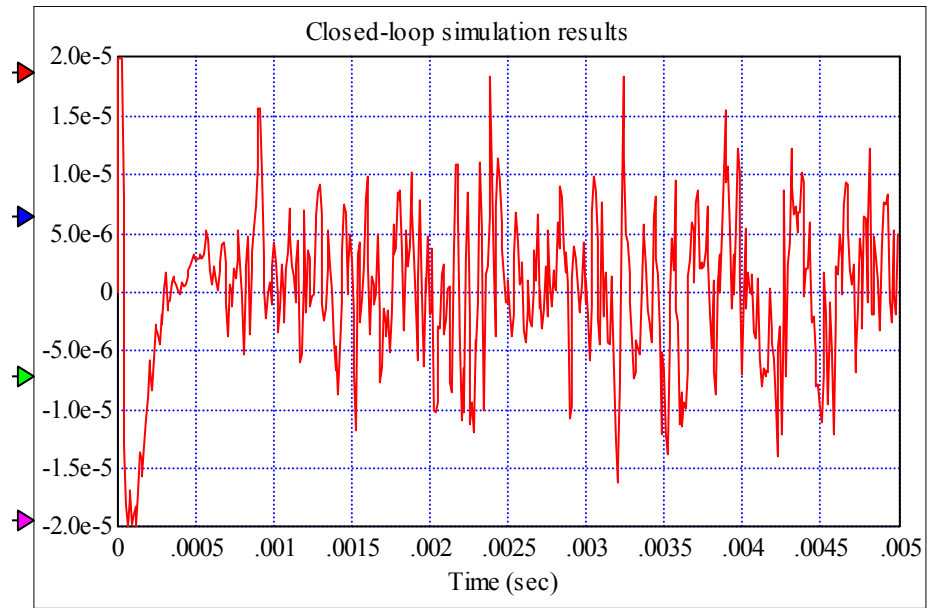


Figure 5.16. Elevation response to noise signal injected in the horizontal channel

Propagation of a disturbance signal through the system results in the output signal error. As can be seen from Fig. 5.15, the amplitude of this signal is very small. The estimated SNR in the output of the azimuth channel is approximately 14000; therefore, disturbance rejection for this channel is

$$20 \log \left(\frac{14000}{250} \right) = 35dB$$

For the elevation channel (see Fig. 5.16) SNR = 160000, and disturbance rejection is

$$20 \log \left(\frac{160000}{250} \right) = 56dB$$

Similar simulations have been performed for the case when the noise is injected in the elevation channel. The results are presented in Fig. 5.17 and 5.18.

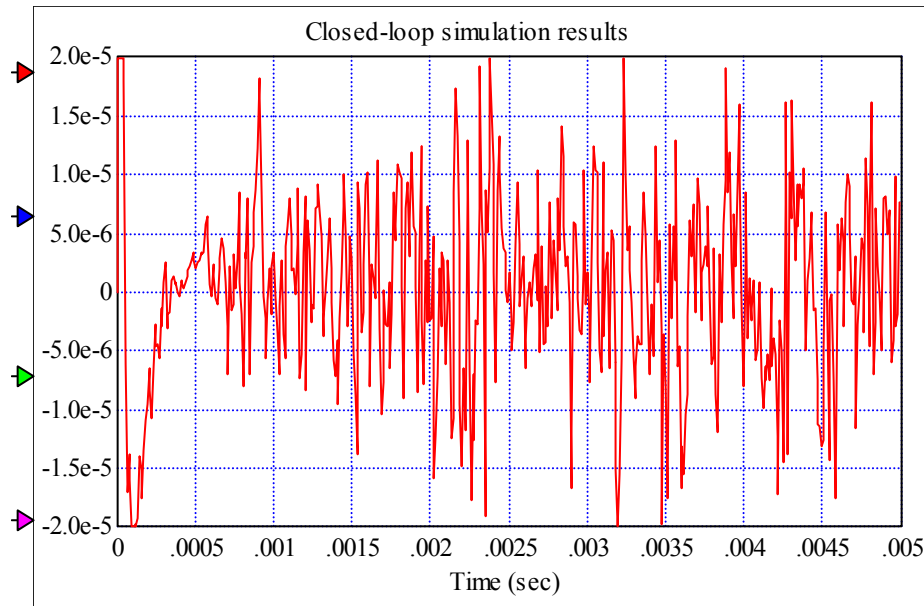


Figure 5.17 Azimuth response to noise signal injected in the vertical channel

One can see from Fig. 5.17 and 5.18 that disturbance rejection is large in the channel where the noise is injected, and even larger in the other channel due to decoupling effect of the AMF control system.

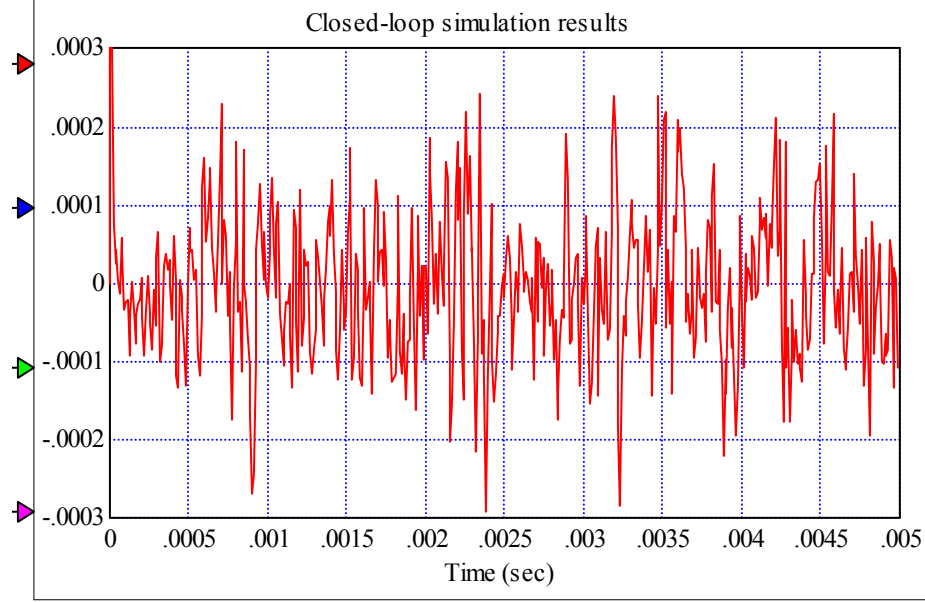


Figure 5.18 Elevation response to noise signal injected in the vertical channel

5.5. Acoustic Power Control: Diffraction Efficiencies

The overall diffraction efficiency is evaluated by multiplying the diffraction efficiencies of the two cells. Diffraction efficiency of each cell depends, in particular, on acoustic power and is computed using the formulas given in Chapters 1 and 3 as follows

$$\eta = \sin^2 \left\{ \frac{\pi}{\lambda \cos \Theta} \sqrt{\frac{M_2 L}{2H} P_a} \right\} = \sin^2 \left\{ \frac{\pi}{\lambda \sqrt{\cos \Theta_i \cos \Theta_d}} \sqrt{\frac{M_2 L}{2H} P_a} \right\}$$

This parameter is sensitive to the transducer length and height as well as acoustic power. It is also dependent on the incident and diffracted angle in the case of the birefringent cells. However, due to the fact that these angles are generally small (in the order of microradians), their cosine is very close to 1 and can often be disregarded.

As an example let us consider a Bragg cell with the following parameters:
acoustic bandwidth $\Delta f = 12$ MHz (from 18MHz to 30 MHz); deflection figure of merit
 $M2 = 1200 \cdot 10^{-15}$

transducer length $L = 16$ mm

transducer height $H = 25$ mm

The wavelength of the laser beam is 670 nm. First approach to power management mentioned in Chapter 1 is the use of constant acoustic power. The setup in our laboratory provides 400 mW to each Bragg cell. As a simulation experiment, frequency of the RF signal applied to the transducer has been varied between 18 and 30 MHz in a sinusoidal manner as shown in Fig. 5.19.

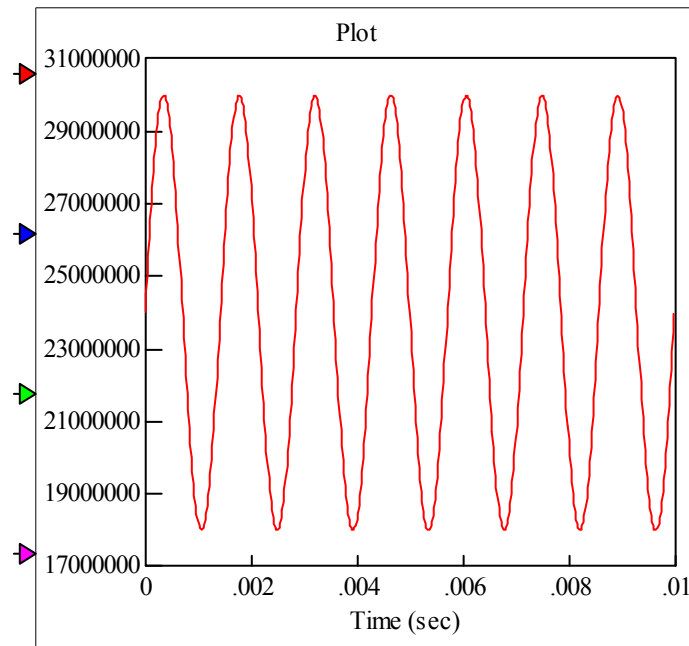


Figure. 5.19. Acoustic frequency applied to the Bragg cell

According to the equations of physics presented in Chapter 3 for a birefringent cell, the deflection angle changes as shown in Fig. 5.20. Note that the deflection angle is obtained with respect to the direction of the first diffracted order corresponding to the center frequency. Fig. 5.21 presents diffraction efficiency dynamics as steering from the minimum to the maximum deflection angle is performed.

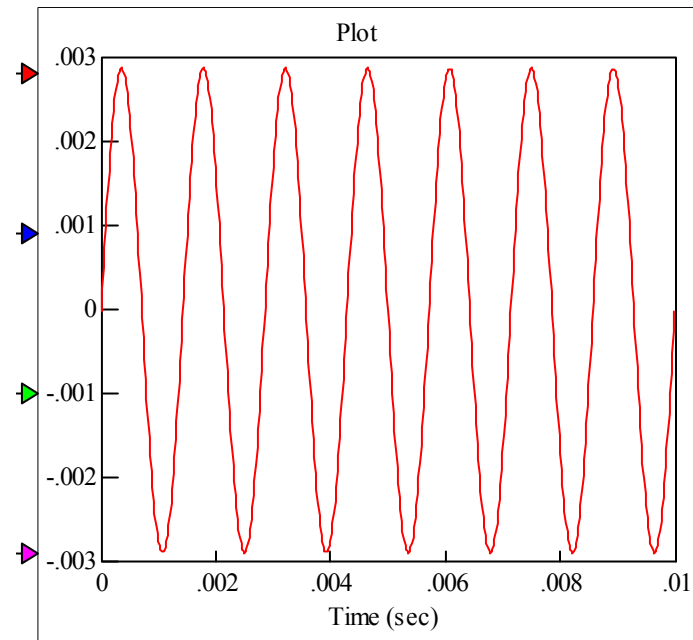


Figure 5.20. Deflection angle change

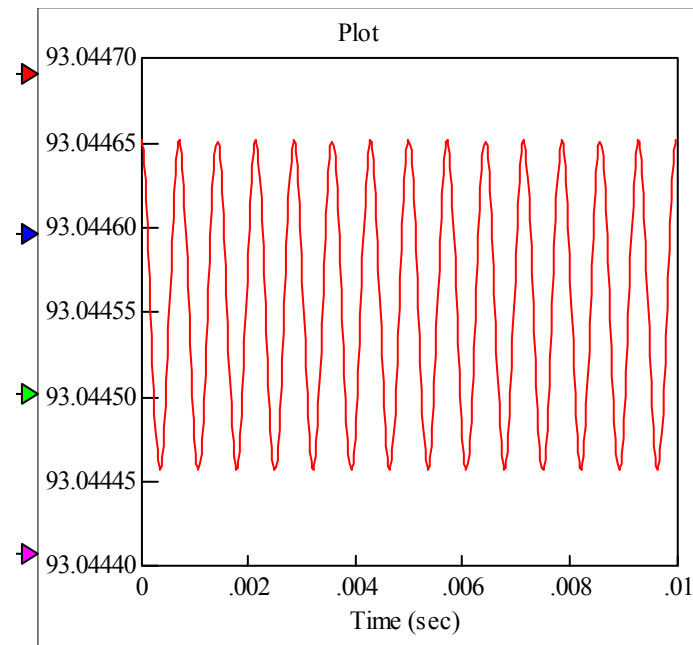


Figure 5.21. Diffraction efficiency for $P_a = 400$ mW

As can be seen from Fig. 5.21, the change in diffraction efficiency is negligible due to the fact that steering range is small. Acoustic power can be adjusted to maximize η as follows. Assuming that $\cos(\Theta_i) = \cos(\Theta_d) = 1$, we have

$$P_a = \frac{H\lambda}{2M_2L} = \frac{0.025 * (670 * 10^{-9})^2}{2 * 1200 * 10^{-15} * 0.016} = 0.2923W$$

Figure 5.22 presents simulation results for the acoustic power computed above.

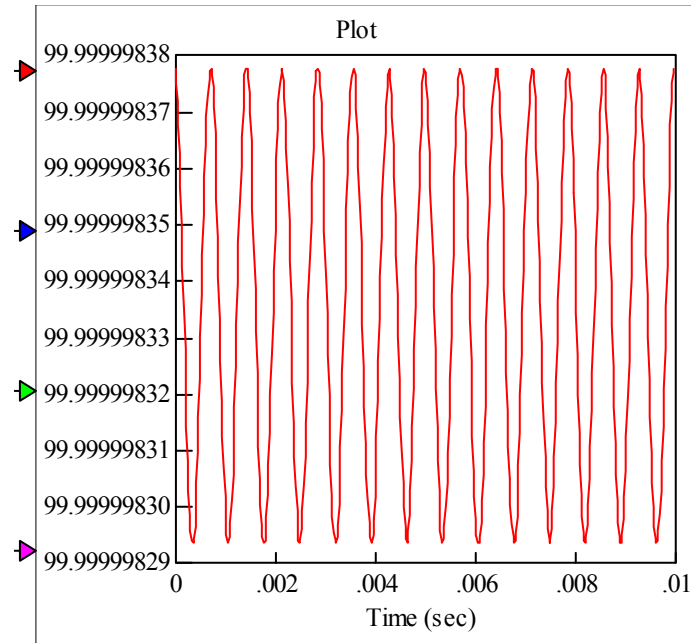


Figure 5.22. Diffraction efficiency for $P_a = 292.3$ mW

The following conclusion can be made. For small steering range constant acoustic power can be used for the Bragg cell to ensure high diffraction efficiency. Modulation described by (1.28) is necessary only when $\cos(\Theta_d)$ significantly deviates from 1. As can be seen from the results presented in Fig. 5.21 and 5.22, high diffraction efficiency can be achieved for a relatively large acoustic power range. A plot of diffraction efficiency as a function of acoustic power is presented in Fig. 5.23.

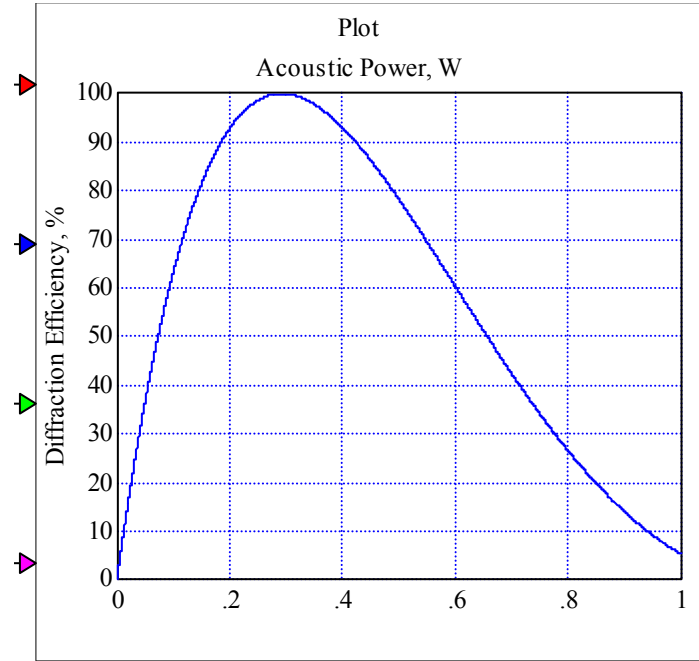


Figure 5.23. Diffraction efficiency as a function of acoustic power

The only concern about acoustic power is that in the case when it is not selected appropriately, and the sound wave attenuates as it traverses the laser beam, diffraction efficiency changes in the direction of acoustic wave propagation and may become too small at some point. As a result, we can observe the effect discussed in Chapter 2, when distortion of the deflected beam profile occurs, and the overall efficiency of the device decreases. Therefore, it is recommended to perform optimal design of the Bragg cell using several constraints and criteria. Attenuation will pose a requirement on the minimum acoustic power. The equation of diffraction efficiency should also be used as one of the constraints to ensure that this parameter does not decrease below the required value. Depending on other design specifications and system characteristics that need to be minimized or maximized, a procedure, such as genetic algorithm optimization discussed in Chapter 3 may be successfully utilized.

5.6. Conclusion

In this part of the project simulation analysis of the Bragg cell-based steering system has been performed. It has been demonstrated that uncompensated system exhibits nonlinear behavior and has coupling between its dynamic channels.

The model reference control approach has been applied and an Adaptive Model Following control system based on hyperstability and positivity principle has been designed. It has been proved by simulations that the controllers decouple and linearize the plant. It has also been demonstrated that this system offers at least 35 dB noise rejection.

A diffraction efficiency model has been implemented in simulation software. It has been demonstrated that for many practical tasks acoustic power modulation is not necessary. It has also been demonstrated that acceptable diffraction efficiency can be obtained over a range of values for P_a . The issue of proper selection of acoustic power in terms of acoustic attenuation has also been addressed. The results obtained by simulations and analysis point in the direction of implementing optimization procedures for selecting parameters of the Bragg cell and other system components.

REFERENCES

- [1] Yoan D. Landau, "Adaptive Control. The Model Reference Approach", Marcel Dekker, Inc.
- [2] Skormin V.A., T.E. Busch, and M.A. Givens, "Model Reference Approach for Compensation of Bending Modes in Fine Steering Mirrors": SPIE Free-Space Laser Communications 1995.
- [3] Skormin, V.A., Tascillo, M.A., and Nicholson, D.J., "A Jitter Rejection Technique in a Satellite-Based Laser Communication Systems", Optical Engineering, November 93.
- [4] Skormin, V.A., Busch, T.E., and Tascillo, M.A., "An Adaptive Jitter Rejection Technique Applicable to Airborne Laser Communication System", Optical Engineering, May 1995 (Also in the Book "Selected Papers on Precision Stabilization and Tracking Systems for Acquisition, Pointing, and Control Applications", SPIE Optical Engineering Press).
- [5] Skormin, V.A., Busch, T.E., and Tascillo, M.A., "Demonstration of Jitter Rejection Technique for Free Space Laser Communication", IEEE Transactions on Aerospace and Electronic Systems, April 1997